UNIVERSITY OF CALIFORNIA
RIVERSIDE

Synthesis and Surface Modification of Group IV Nanoparticles Using Non-Thermal
Plasmas

A Dissertation submitted in partial satisfaction
of the requirements for the degree of

Doctor of Philosophy

in

Mechanical Engineering

by

Ozgul Yasar-Inceoglu

June 2015

Dissertation Committee:
        Dr. Lorenzo Mangolini, Chairperson
        Dr. Guillermo Aguilar
        Dr. Sandeep Kumar

The Dissertation of Ozgul Yasar-Inceoglu is approved:

_____

_____

_____

Committee Chairperson

University of California, Riverside

Acknowledgements

First of all, I would like to express my special thanks to my Ph.D. advisor Dr. Lorenzo Mangolini who never hesitated to convey all his experience to me in order to facilitate this hard work. His constructive suggestions, sincere attitude and support gave me the courage I needed to complete this research. With his valuable advice and guidance he not only helped me throughout my doctoral studies but also prepared me for my next career.

I sincerely thank to my committee members Dr. Guillermo Aguilar and Dr. Sandeep Kumar to serve as my committee members in their busy schedules and being available for guidance and support. I greatly appreciate their valuable comments and suggestions for perfecting this dissertation.

I would like to thank my lab group members Lanlan Zhong, Thomas Lopez, Devin Coleman, Steven Exarhos, and Alejandro Alvarez for their help and hands on assistance in my experiments. I always enjoyed our discussions on courses, experiments, and academic career. Thanks to all my friends for their friendship and encouragements.

In this dissertation, chapters 3, 4, and 5 are published in Nanotechnology, Materials Letters, and Journal of Applied Physics D: Applied Physics, respectively. I would like to thank to all my co-authors, Lanlan Zhong, Thomas Lopez, Ebrahim Farshihagro, and Devin Coleman, for their contributions to all my published

I would like to give my special thanks to my family. I would like to thank my parents, who provided unconditional love and care, support, trust, and confidence on every part of my life. I am very lucky to have such wonderful parents. I would never complete this work without the support of my twin sister, her husband, my brother, and his wife. I feel greatly indebted to them for being supportive all the time. The smiles of my nieces and nephews were always a source of happiness for me. Thanks to my husband for his continued support, help, and patience. I love you all.

This dissertation is dedicated to my parents.

ABSTRACT OF THE DISSERTATION

Synthesis and Surface Modification of Group IV Nanoparticles Using Non-Thermal
Plasmas

by

Ozgul Yasar-Inceoglu

Doctor of Philosophy, Graduate Program in Mechanical Engineering
University of California, Riverside, June 2015
Dr. Lorenzo Mangolini, Chairperson

The rapidly increasing interest in silicon nanostructures is motivated by important advantages of this material compared to other semiconductors commonly investigated in the broad field of nanotechnology. Silicon nanoparticles are promising materials for many applications such as photovoltaics, transistors, light emitting devices, and energy storage devices.

Commonly used nanoparticle synthesis techniques have many challenges such as high cost, long processing time, and wide particle size distribution. In this dissertation, non-thermal plasma technique is used to overcome these challenges. In this study, in order to produce high quality nanoparticles, the direct comparison of the use of a chlorinated and hydrogenated precursor and its consequences on both the process parameters and material properties are initially investigated. The analysis results show that the chlorinated precursor yields nanoparticles vulnerable against oxidation in air compared to the hydrogenated precursor. In addition, it is found that in the chlorinated precursor case the gas composition needs to be modified and hydrogen needs to be added to the mixture to enable the nucleation and growth of the powder. Silicon nanocrystals with sizes between 5 and 10 nm have been produced in a non-thermal plasma reactor using chlorinated precursor.

The properties of the silicon nanoparticles can be tuned through post-processing steps to optimize for targeted applications. In particular surface modification is generally necessary to both tune dispersibility of the particles in desired solvents to achieve optimal coating conditions, and to interface the particles with other materials to realize functional heterostructures. In this contribution a non-thermal plasma-based process for the synthesis of silicon nanoparticles and their in-flight coating with a plasma polymerized shell (silicon/polymer core/shell) has been developed. It is found that it is possible to tune the chemistry of the shell by modifying the gas-phase composition during the polymerization step.

These nanoparticles are used as an anode material for lithium-ion batteries. The coating of the silicon particle with a polymer shell offers a way to uniformly disperse the particles into a carbon matrix after high-temperature treatment, which provides an improvement in the stability of an anode for lithium-ion batteries, compared to the case of uncoated silicon particles.

Table of Contents

List of Figures

Chapter 1 Introduction

Characteristics of Nanoparticles

Nanotechnology is an important concept that positively affects the economy, environment, and every field of society. Nanoparticles are the integral parts of nanostructures and devices. Nanoparticles can be classified as zero-dimensional (0D) nanostructures and can be defined as the particles whose sizes range between one to hundreds of nanometer. In 1980s, nanoparticles started to attract attention and the researches on zero-dimensional nanostructures showed an important progress in the last ten years [1, 2]. Nanoparticles especially semiconductor and metal nanoparticles hold a special place in the broad field of scientific research because of their unique electronic properties. They can be used for variety of applications in medicine, information technology, biotechnologies, medical devices, military application, energy production and energy storage, material technologies, environmental applications..

The properties of bulk materials and nanoparticles show different characteristics. For instance, mechanical, electrical, thermal, and optical properties of the bulk materials and nano size particles differ from each other for the same materials. Nanoparticle properties can be an intermediate level between bulk and atomic level materials and their properties change by their size. Other than size, shape and surface

properties are also the main factors that affect the material characteristics such as physical and chemical properties.

Size dependent property changes can be explained as the quantum confinement. Quantum confinement describes the change in electron energy levels and band gaps due to substantial decrease in particle size, especially in nanoscale. At that scale electrons and electron holes are squeezed in to a dimension described as exciton Bohr radius. The quantum confinement phenomenon is observed when the diameter of the particle reaches a critical size which is known as de Broglie wavelength. Decrease in size of particles also causes increase in surface energy due to the high surface to volume ratio. Therefore, nanoparticles have unique optical, electrical, and magnetic properties which differ from bulk material.

Nanoparticles can be in different structural forms where it can have amorphous or crystalline structure. They can also exist in different chemical compositions such as single or multi elements, and shapes (sphere, cubic etc.). Nanoparticles can be produced as free standing particles, or can be embedded in matrix which can be metallic, ceramic, or polymeric.

Group II-VI semionductors, which are Cadmium selenide (CdSe), Cadmium sulfide (CdS), Zinc selenide (ZnSe), and Zinc sulfide (ZnS), are commonly used materials for different applications especially for light emitting devices, and photovoltaic devices because of their several properties such as direct band gap, and ease of synthesis [3].

However, the important advantages of silicon over other semiconductors made it more interesting material than commonly used materials such as group II-VI semiconductors and metal chalcogenides in nanotechnology.

Group IV Elements

In the periodic table, group IV elements, which are also known as carbon family, comprise of metallic and non-metallic elements and thus they show different properties from top to bottom, Carbon (C), Silicon (Si), Germanium (Ge), Tin (Sn), and Lead (Pb), respectively. The Group IV element properties change from non-metallic to metallic properties based on the structure, bonding with chloride and hydride, and the oxidation state. While C shows nonmetallic properties, Si and Ge show metalloid properties, and Sn, and Pb show metallic properties. On the other hand, based on the allotropes of Sn, it might exhibit non-metallic and metallic properties. For instance, gray tin, which is also known as α-tin, is semiconductor, and white tin is conductor [4, 5].

All group IV elements can be found in nature except germanium. Germanium can be found in traces such as zinc ores, coal, and silver. Silicon and carbon are the most abundant elements in the earth compared to lead and tin which are also called rare elements.

Table 1-1 shows the atomic number and atomic mass for group IV elements. As a common property, all of Group IV elements C, Si, Ge, Sn, and Pb have four valence electrodes in their highest energy orbitals ($ns^2 np^2$). The electronegativities of these elements are constant or slightly decreases when the atomic mass and atomic radii increases [6]. Based on their electronic properties, group IV elements can be grouped as non-conductor (i.e. carbon), semiconductors (i.e. silicon and germanium), and conductors (i.e. tin and lead).

Comparing the physical properties of Group IV elements, since carbon has strong covalent bonds, it has the highest melting point and boiling point which are 3750 ^oC and 4827 ^oC , respectively [7]. Melting point of silicon, germanium, tin, and lead are 1421, 937, 232, 325 ^oC, respectively.

Table 1-1 Atomic number, atomic mass, and electron configuration of group IV elements

Element	Atomic Number	Atomic Mass	Electron Configuration
Carbon (C)	6	12.011	$[He]2s^22p^2$
Silicon (Si)	14	28.0855	$[Ne]3s^22p^2$
Germanium (Ge)	32	72.61	$[Ar]3d^{10}4s^24p^2$
Tin (Sn)	50	118.710	$[Kr]4d^{10}5s^25p^2$
Lead (Pb)	82	207.2	$[Xe]4f^{14}5d^{10}6s^26p^2$

Silicon Nanoparticles

Silicon, discovered by Jons Jacobs Berzelius in 1824, the most important member of Group IV elements in periodic table and can be in amorphous form or in crystalline form which show different physical and chemical properties. Silicon is applied in variety of industries that we encounter often in our daily lives. For instance, it presents in sand, clay, bricks, toothpaste, hair conditioner, glass, mica, plastics, contact lenses, calculators, and refrigerators etc.

Silicon nanocrystals and silicon based nanostructures also play an important role in the broad field of nanotechnology because of its many advantages. They can be used for different applications. They can be used in electronic devices such as transistors, and computer chips, in photovoltaic devices, optical devices such as light emitting devices, and bio related applications such as biosensors, or artificial arms, and legs[8].

Silicon is also the best-known and main semiconductor material which is used in semiconductor technology. The advantages of silicon over other semiconductors such as group II-VI semiconductors and metal chalcogenides make silicon more beneficial for different variety of applications. One of the advantages of silicon is its high resource abundance. Silicon is the second most abundant element in the earth after oxygen and seventh most abundant element on the entire universe. It composes approximately the 28 percent of earth mass [8]. It has low cost and it is non-toxic in its bulk form which is important for environmental health issues and safety.

Silicon is a metalloid material and it can show both metallic and non-metallic properties. A distinctive property of silicon among other semiconductors is that it is an indirect bandgap material which causes some limitations for bulk silicon in optical device applications. When the size of silicon nanoparticles approach to bulk Bohr radius, which is 4 nm for silicon, the optical and electrical properties change because of the quantum confinement and surface effects. For instance, the intensity of the photoluminescence can be adjusted by changing particle size and thus band gap. In the literature the unique properties of silicon nanoparticles are studied through particle size-controlled experiments utilizing variety of synthesis techniques [9, 10].

Although porous silicon nanoparticles show high photoluminescence, surface oxidation of hydrogen terminated silicon nanoparticles reduces the photoluminescence intensity and thus causes blue shift which has been a technical challenge about these materials [11, 12]. It has been shown that silicon nanoparticles with a diameter less than 5 nm have photoluminescence emission in visible range. [10].

Photoluminescence peak energy is investigated by Ledoux et al. for silicon nanoparticles with different sizes [13]. They obtained theoretical data based on quantum confinement model using a linear combination of atomic orbitals (LCAO) which was shown as the following equation.

$$E_g(eV)(d) = E_0(eV) + \frac{3.73}{d(nm)^{1.39}}$$

where, E_g represents the recommendation energy of electron-hole pair, E_0 is the bulk silicon band gap, which is 1.17 eV, and d denotes the diameter of the silicon nanoparticles. In Figure 1-1 while the solid curve shows the theoretical data, the other curves represent the results from similar experimental analyses. The authors showed that the experimental and theoretical data were in good agreement. However, the theoretical and experimental data did not match quite well only at the end range
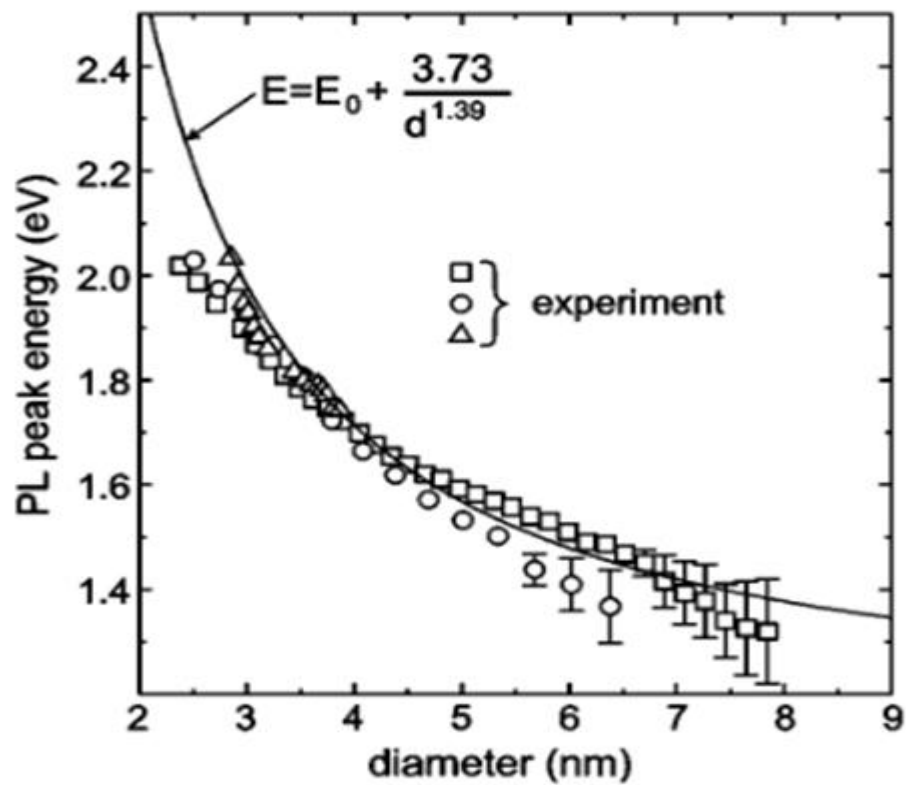
Figure 1-1 Relationship between the photoluminescence peak energy and particle diameter [13]

particle sizes which were because of the surface oxidation and size distribution.

Size distribution plays an important role on the photoluminescence. Wide size distribution results in lower photoluminescence intensity [14, 15]. It has been shown that the photominescence properties of silicon nanoparticles are influenced by the presence of oxygen and nitrogen [16, 17].

Quantum confinement effect which affects the photoluminescence properties of silicon nanoparticles is also related to the electronic properties of nanoparticles. Change in the particle size causes the conduction band and valence band shift. Van Buuren et al. demonstrated that band shift was inversely correlated with the particle size [18].

It has been shown that silicon nanocrystals has good optical properties such as bright emission, photo-stability, size dependent and wavelength tunable luminescence, and long fluorescence life time [19, 20].

Silicon-based nanostructures are potentially compatible with already developed integrated circuit (IC) architectures and/or microfabrication schemes. Several types of silicon-based nanostructures are under intense investigation. For instance, quantum confined silicon in the form of either porous silicon [21], nanoparticles dispersed in a dielectric matrix [22], or free standing quantum dots [23] are promising for many applications including the fabrication of highly efficient light emitting devices [24] or photovoltaic devices [25]. Free standing nanocrystals are potential building blocks of

single particle transistors [26] and a variety of other electronic devices [27]. Silicon nanoparticles have also been used to produce bulk nanostructured silicon samples for thermoelectric applications [28] and have been integrated into the anode of lithium-ion batteries [29]. Silicon nanowires are also attracting increasing interest of researchers for both thermoelectric and photovoltaic applications [30-32].

Nanoparticle Synthesis Techniques

Nanoparticle synthesis techniques can be classified based on the synthesis environment. They can be synthesized by using liquid phase, gas phase, or solid phase methods. The liquid phase synthesis is based on the wet chemistry means that the chemical reactions in the solvents. Evaporation decomposition, precipitation, and sol-gel process are the different kinds of liquid phase techniques. High quality group II-VI nanoparticles can be synthesized using the liquid phase techniques. However, it is not a preferred technique to produce silicon nanoparticles because it yields the low quality nanoparticles with a wide size distribution. In order to prevent the moisture and contaminate the particles and solvents, the process should be done under inert gas.

Silicon nanocrystals were synthesized in liquid phase by different researchers. Baldwin et al. synthesized silicon nanocrystals using silicon tetrachloride ($SiCl_4$) as a silicon precursor, and different reducing agents. Silicon nanocrystals synthesized at high temperature and pressure using organosilane precursor (diphenylsilane) by Korgel

group [33]. Even though they were able to produce high quality crystalline silicon nanoparticles, low mass yield was still a problem.

Ball milling is the most commonly used solid phase nanoparticle production method. Although large particle size had been an important challenge for ball milling process, Lam et al. was able to produce silicon nanoparticles with diameter as small as approximately 5 nm using ball milling method [34]. The authors used graphite and SiO_2 powders and applied to ball milling process for 10 and 7 days. After 48 hours annealing process at 150 °C, they continued the milling process for 48 hours. The authors obtained that the produced particles were mostly in spherical shape and also complex coarse shapes. Although small size nanoparticles are produced, size distribution and particle agglomeration are still challenges of the ball milling. Therefore, this is not a preferred technique compared to the other types of nanoparticle synthesis techniques.

Gas phase techniques are based on physical and chemical reactions. High quality nanoparticles can be produced by using gas phase techniques compared to other methods. Pulsed laser ablation, furnace and laser pyrolysis are the commonly used gas phase techniques.

Pulsed laser ablation is one of the techniques that are used to produce silicon nanoparticles based on the physical process. There are three main stages of the synthesis of silicon nanoparticles based on the kinetic energy of silicon atoms. These stages are high kinetic energy region, nucleation region, and transporting region. In the

first region, silicon atoms release kinetic energy with the collision of the ambient gas atoms. The kinetic energy of the silicon atoms decreases when silicon atoms move away from the silicon target. The nucleation region plays an important role in the formation of silicon nanoparticles and defining the size.

Fu et al. synthesized silicon nanoparticles by pulsed laser ablation technique. Silicon wafer was used as a target and pulsed laser at a nanosecond or femtosecond rate hit the target and ejected the silicon atoms to produce silicon nanoparticles with less surface contamination [35]. Usually helium (He), argon (Ar), and neon (Ne) are used as an ambient gas for this technique. They investigated the importance of the ambient gas on the silicon nanoparticles. They obtained that the most uniform and small silicon nanoparticles can be produced with using Ne gas. The reason behind this is the atomic weight of Neon, which is the closest to the atomic weight of silicon compared to Argon and Helium. The relation between the size of silicon nanoparticles and ambient gas pressure was investigated by Yoshida and his group. They used inertia fluid model to show the effect of the gas pressure on the particle size. The dashed line in Figure 1-2 represents the theoretical data using inertia liquid model. They showed that the particle size was proportional to the ambient gas pressure, that is, the increase of the ambient gas pressure increases the particle size and thus causes the increase in the binding energy [36].
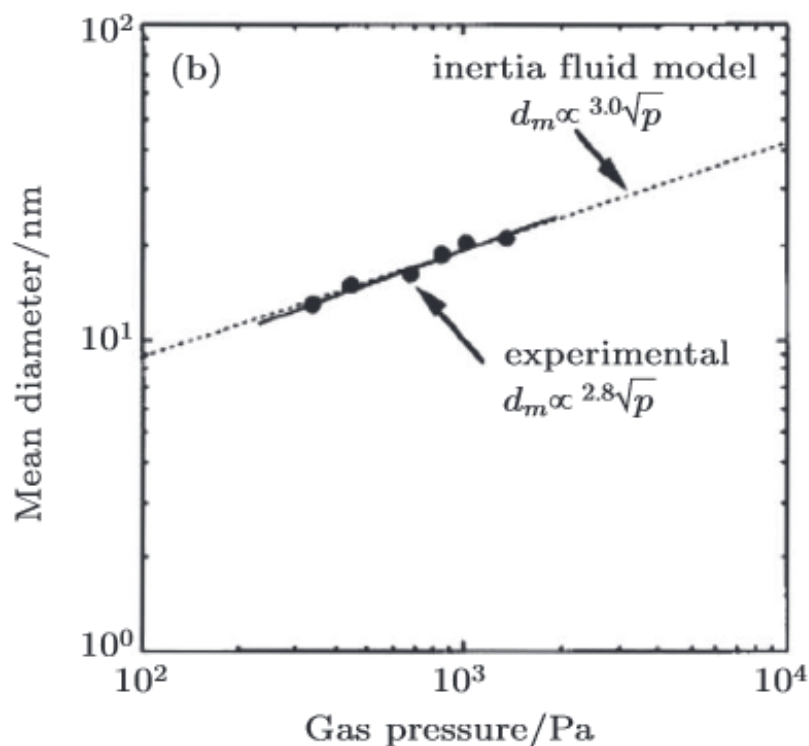
Figure 1-2 Relationship between particle mean diameter and ambient gas pressure [36].

Non-Thermal Plasma System

Nanoparticle synthesis can be done by three main groups of synthesis techniques. These techniques are particle reduction in the solid phase, liquid phase, and gas phase. Although the solid phase techniques have low cost, controlling the shape and size of the nanoparticles in this method is difficult. The liquid phase techniques have many drawbacks such as high cost, long processing time, multiple steps involved, and

large amount of solvents used. The common shortcoming of the gas phase techniques is that they require high temperatures which yield size distribution because of particle agglomeration.

Plasma processing is an important nanoparticle synthesis technique that overcomes these challenges. One of the common uses of non-thermal plasmas is the deposition of silicon thin films. For this process, usually silane is used as a silicon precursor. Greater amount of nanoparticles can be produced using plasma techniques in a short processing time compared to other synthesis methods. Non-thermal plasma technique is the most advantageous plasma processing method mainly because of its cost effectiveness and room temperature processing. In addition to these advantages, particle charging, particle confinement, and selective nanoparticle heating are the other important benefits that make non-thermal plasma system more efficient.

Plasma is determined as the fourth state of matter after solid, liquid and gas states. Gas to plasma change occurs through the ionization reaction. Plasma can be defined as a collection of free charged nanoparticles moving in random directions [37]. The characteristics of plasma can be defined by mainly the temperatures and densities that are exist in plasma such as electron temperature (T_e), ion temperature (T_i), gas temperature (T_g), electron density (n_e), ion density (n_i), and gas density (n_g).

Nanoparticle nucleation in thermal plasmas can be described as the gas molecules decompose and forms atoms which move in random directions at high

temperatures. Even at higher temperature they decompose to charged particles which represent the plasma state. The plasma state is considered as thermal equilibrium where electron temperature and ion temperature are equal to each other. Non-thermal plasma is characterized by the non-equilibrium process. With applying the electric field to the gas, electrons accelerate and ionize the gas. The temperature of the electrons is between 20 000 K and 50 000 K (2 eV and 5 eV) for the non-thermal plasma systems, which cause the dissociation of gas atoms. Particle charging depends on the electron and ion densities, and electron temperature based on the given radius of nanoparticles [38]. While the electron temperature reaches to very high value, the ion temperature remains approximately at room temperature. Thermal velocity of electrons is also larger than thermal velocity of ions. Thus, all the surfaces in contact with plasma in the system are negatively charged.

Using non-thermal plasma technique, uniform negatively charged particles can be produced. This is an important advantage for the non-thermal plasmas because it prevents or significantly reduces the particle agglomeration.

Conductive Polymers

Polymers are known as insulator materials. Hovewer, Bolto et al. indicated that the conductive sign of polypyrole in 1963 [39]. Later, Shirakawa and his coworkers showed the synthesis of doped polyacetylene as the first synthesized conductive

polymer in 1977 [40]. New class of polymers which are called as conductive polymers were produced in 1970s and became popular among researchers especially for the last two decades.

Since the conductive polymers show both metallic and polymeric properties, they are preferred for different applications from electronic technology to medical sciences. Since they have good optical and electrical properties, they can be used for light emitting diodes and rechargeable batteries. Their biocompatible and biodegradable properties make them also favorable material for the bio-related applications such as artificial muscles and biosensors.

Polypyrrol (PPY), polyaniline (PANI), polyphenylene (PP), polyphenylene vinylene (PPV), polyasulfone (PS), and Polythiophen (PT) are the mostly used conjugated conductive polymers for different research fields. Figure 1-3 shows the chemical structures of common conductive polymers [41]. The first synthesized conductive polymer polyacetylene is investigated by many researchers. However, high chemical instability of this polymer in air became a major disadvantage and redirected the attention of researchers to air stable conductive polymers.
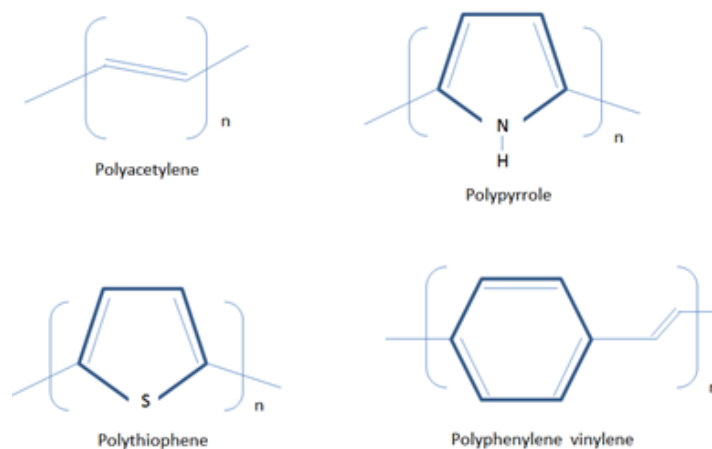
Figure 1-3 Chemical structure of common conductive polymers

Conjugated Polymers

In order for a polymer to be conductive, it needs an orbital system that allows the free travel of charge carriers along the entire structure as seen in metals. The conjugated polymers formed by a backbone chain with alternating double and single bonds, possess atoms providing orbital overlapping for a continuous movement of electrons. The conductivity of conjugated polymer can be enhanced through doping, which adds or removes electrons to the backbone chain. The doping process forms conductive bands and allows free flow of electrons, which contributes to the conductivity. Almost all conjugated polymers can be doped through partially oxidizing (p-type redox doping) and partially reducing (n-type redox doping) with electron

acceptors or donors. Figure 1-4 indicates the conductivity comparison of conjugated

polymers, semiconductors, and metals.

Polyaniline

Conductive polymers with aromatic backbone such as polythiophene (PTH) [42],

polypyrrole (PPY) [43], and polyaniline (PANI) [44] are preferred polymers used for
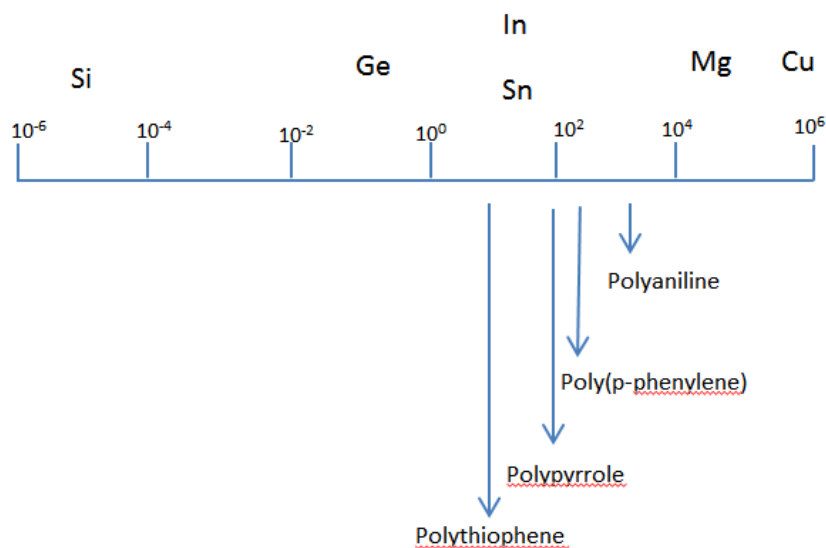
Figure 1-4 The conductivities of conjugated polymers compared to metals and
semiconductors.

different applications especially for coating Si particles. Among these polymers, high

conductivity, unique redox behavior, low cost, and high chemical stability, and good

environment stability makes polyaniline (PANI) more advantages over other materials [45-47]. Polyaniline is also known as aniline black and developed in 1980s. It is phenylene base polymer and it has –NH- group in the polymer chain.

The structure of the base polyaniline is shown in Figure 1-5. Polyaniline is consisted of two basic sites which are benzenoid and quinoid units. Benzenoid units represent the amine –NH- group which is bonded to aromatic rings and quinoid units represents the imine =N- group which is bonded to aromatic rings.

Polyaniline can be in three different forms which are based on the protonation degree and oxidation state of polyaniline. These forms are named as Leucomeraldine (LE), Pernigraniline (PE), and Emeraldine (EB) and they can be converted to each other by chemical reactions. The electronic structure of the polyaniline is based on the overlap and alternating nitrogen and carbon rings. These three forms of polyaniline have different electrical properties.

The conductivity of the polyaniline can be controlled by doping process, which can be done by chemical, electrochemical, or photochemical ways.

Based on the structural formula of polyaniline as seen in the Figure 1-5, different
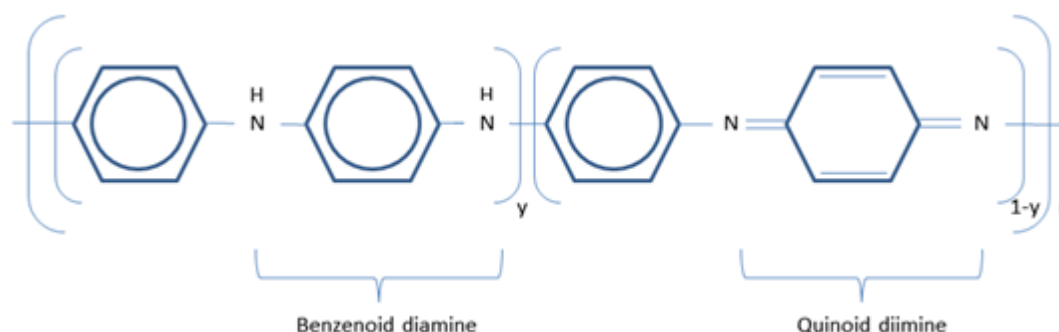
Figure 1-5 Chemical structure of Polyaniline (PANI)

oxidation states of PANI, ie, leucomeraldine, emeraldine, and pernigraniline, respectively, can be obtained for the y-values of 1, 0.5, and 0. All these forms of PANI can exist both in base and protonated salt forms. While Leucomeraldine refers to fully reduced form of polyaniline, emeraldine base (EB) refers to half oxidized form of polyaniline, and pernigraniline is completely oxidized form of polyaniline. Emeraldine salt is the only conductive form of polyaniline. Emeraldine salt, which has green color, can be produced when the emeraldine base is doped or protonated. Leucomeraldine and pernigraniline forms are nonconductive forms of polyaniline and they have white and violet colors, respectively.

The conductivity mechanism of polyaniline is more complex than the other conductive materials. The conductivity of the polyaniline depends on the oxidation and protonation degrees. The reason behind this is the formation of radical cations. Radical

cations usually form at carbon for the general conductive polymers but for the Polyaniline case nitrogen atoms contributes to the formation of radical cations and they are involved in the polymer chain. Conductive form of polyaniline (emeraldine salt) can be produced by doping (injecting extra electrons and holes) the emeraldine base form. Doping level determines the conductivity magnitude. For instance, with 50% of doping level, the polyaniline reaches to its highest conductivity level. The conductivity of polyaniline can be increased approximately 10 order of magnitude [48].

Plasma Polymerization

Plasma polymerization, also known as glow discharge polymerization, can be defined as the formation of polymers under plasma conditions which contains ions, energetic photons, and molecules that occur by applying electric field to the plasma reactor. There are two main reactor types used for plasma polymerization. The bell-jar type reactors have parallel plate metal electrodes, which require direct-current (DC) or alternating-current (AC) voltage. The other reactor type is tubular reactor that has external ring or coil electrodes which are connected to radio frequency (RF) power source [49]. The surface activation occurs by particle collision or photon radiation which enhances the monomer's deposition that leads to polymerization of materials' surface [50]. Monomer molecules flow through the plasma reactor and they dissociate to electrons, ions, free radicals, and neutral particles by plasma discharge. This causes

highly branched and cross-linked three dimensional network which is called as plasma polymers [51].

Physical properties of polymers depend on the plasma process parameters [52]. Plasma parameters can be divided into two categories. The first category is the characteristic parameters of reactor such as electrode size, the distance between electrodes, and electric power frequency. The second group of parameters is related to the adjustment for each run or during run such as monomer flow rate, system pressure, and RF power which play an important role to produce ideal particles [53, 54].

The polymers that are coated to materials by plasma polymerization technique contain chains that are branched and randomly terminated with a high degree of cross-linking, which increases the mechanical strength of the coated particles, instead of regularly repeating units [55-57]. Since the vapor of the monomer is transferred into the plasma reactor, there are no oxidants and solvent involved into plasma which prevents the contamination of the extraneous species. It is also a solvent free, room temperature process, and low cost process. Overall, the non-thermal plasma polymerization provide very short processing time compared to the conventional polymerization (liquid phase) because while the gas atoms and ions are at room temperature, the temperature of the free electrons reaches to very high temperatures as 20,000 - 50,000 Kelvin which dissociates organic ligand molecules and provides chemically highly reactive species. Since both plasma reactor wall and particles are charged negatively, nanoparticles

repulse each other which avoids particle agglomeration of particles, and it also reduces

diffusional loss of the nanoparticles to the walls .

References

[1]   M. A. Reed, R. T. Bate, K. Bradshaw, W. M. Duncan, W. R. Frensley, J. W. Lee*, et al.*, "Spatial Quantization in Gaas-Algaas Multiple Quantum Dots," *Journal of Vacuum Science & Technology B,* vol. 4, pp. 358-360, Jan-Feb 1986*.*

[2]   S. Schmittrink, D. A. B. Miller, and D. S. Chemla, "Theory of the Linear and Nonlinear Optical-Properties of Semiconductor Microcrystallites," *Physical Review B,* vol. 35, pp. 8113-8125, May 15 1987.

[3]   E. C. Hao, H. P. Sun, Z. Zhou, J. Q. Liu, B. Yang, and J. C. Shen, "Synthesis and optical properties of CdSe and CdSe/CdS nanoparticles," *Chemistry of Materials,* vol. 11, pp. 3096-3102, Nov 1999.

[4]   J. O. Bird and P. J. Chivers, *Newnes engineering and physical science pocket book*, 2nd ed. Oxford ; Boston: Newnes, 1996.

[5]   P. Y. Yu and M. Cardona, *Fundamentals of semiconductors : physics and materials properties*, 4th ed. Berlin ; New York: Springer, 2010.

[6]   R. S. Drago, "On the Electronegativities of the Group-Iv Elements," *Journal of Inorganic & Nuclear Chemistry,* vol. 15, pp. 237-241, 1960.

[7]   H. McArthur and D. Spalding, *Engineering materials science : properties, uses, degradation, and remediation*. Chichester, U.K.: Horwood Pub., 2004.

[8]   M. A. Sommers, *Silicon*, 1st ed. New York: Rosen Central, 2008.

[9]   H. Chang and S. Q. Sun, "Silicon nanoparticles: Preparation, properties, and applications," *Chinese Physics B,* vol. 23, Aug 2014.

[10]   G. Ledoux, O. Guillois, D. Porterat, C. Reynaud, F. Huisken, B. Kohn*, et al.*, "Photoluminescence properties of silicon nanocrystals as a function of their size," *Physical Review B,* vol. 62, pp. 15942-15951, Dec 15 2000.

[11]   L. T. Canham, "Silicon Quantum Wire Array Fabrication by Electrochemical and Chemical Dissolution of Wafers," *Applied Physics Letters,* vol. 57, pp. 1046-1048, Sep 3 1990.

[12]   X. G. Li, Y. Q. He, and M. T. Swihart, "Surface functionalization of silicon nanoparticles produced by laser-driven pyrolysis of silane followed by HF-HNO3 etching," *Langmuir,* vol. 20, pp. 4720-4727, May 25 2004.

[13]   G. Ledoux, J. Gong, F. Huisken, O. Guillois, and C. Reynaud, "Photoluminescence of size-separated silicon nanocrystals: Confirmation of quantum confinement," *Applied Physics Letters,* vol. 80, pp. 4834-4836, Jun 24 2002.

[14]   P. F. Trwoga, A. J. Kenyon, and C. W. Pitt, "Modeling the contribution of quantum confinement to luminescence from silicon nanoclusters," *Journal of Applied Physics,* vol. 83, pp. 3789-3794, Apr 1 1998.

[15]   C. Meier, A. Gondorf, S. Luttjohann, A. Lorke, and H. Wiggers, "Silicon nanoparticles: Absorption, emission, and the nature of the electronic bandgap," *Journal of Applied Physics,* vol. 101, May 15 2007.

[16]   L. Mangolini, E. Thimsen, and U. Kortshagen, "High-yield plasma synthesis of luminescent silicon nanocrystals," *Nano Letters,* vol. 5, pp. 655-659, Apr 2005.

[17]   Y. Chao, S. Krishnamurthy, M. Montalti, L. H. Lie, A. Houlton, B. R. Horrocks*, et al.*, "Reactions and luminescence in passivated Si nanocrystallites induced by vacuum ultraviolet and soft-x-ray photons," *Journal of Applied Physics,* vol. 98, Aug 15 2005.

[18]   T. van Buuren, L. N. Dinh, L. L. Chase, W. J. Siekhaus, and L. J. Terminello, "Changes in the electronic properties of Si nanocrystals as a function of particle size," *Physical Review Letters,* vol. 80, pp. 3803-3806, Apr 27 1998.

[19]   F. Erogbogbo, K. T. Yong, R. Hu, W. C. Law, H. Ding, C. W. Chang*, et al.*, "Biocompatible Magnetofluorescent Probes: Luminescent Silicon Quantum Dots Coupled with Superparamagnetic Iron(III) Oxide," *Acs Nano,* vol. 4, pp. 5131-5138, Sep 2010.

[20]   Z. H. Kang, Y. Liu, C. H. A. Tsang, D. D. D. Ma, X. Fan, N. B. Wong*, et al.*, "Water-Soluble Silicon Quantum Dots with Wavelength-Tunable Photoluminescence," *Advanced Materials,* vol. 21, pp. 661-+, Feb 9 2009.

[21]   A. G. Cullis, L. T. Canham, and P. D. J. Calcott, "The structural and luminescence properties of porous silicon," *Journal of Applied Physics,* vol. 82, pp. 909-965, Aug 1 1997.

[22]   T. W. Kim, C. H. Cho, B. H. Kim, and S. J. Park, "Quantum confinement effect in crystalline silicon quantum dots in silicon nitride grown using SiH4 and NH3," *Applied Physics Letters,* vol. 88, Mar 20 2006.

[23]   D. Jurbergs, E. Rogojina, L. Mangolini, and U. Kortshagen, "Silicon nanocrystals with ensemble quantum yields exceeding 60%," *Applied Physics Letters,* vol. 88, Jun 5 2006.

[24]   K. Y. Cheng, R. Anthony, U. R. Kortshagen, and R. J. Holmes, "High-Efficiency Silicon Nanocrystal Light-Emitting Devices," *Nano Letters,* vol. 11, pp. 1952-1956, May 2011.

[25]   C. Y. Liu, Z. C. Holman, and U. R. Kortshagen, "Optimization of Si NC/P3HT Hybrid Solar Cells," *Advanced Functional Materials,* vol. 20, pp. 2157-2164, Jul 9 2010.

[26]   Y. P. Ding, Y. Dong, A. Bapat, J. D. Nowak, C. B. Carter, U. R. Kortshagen*, et al.*, "Single nanoparticle semiconductor devices," *Ieee Transactions on Electron Devices,* vol. 53, pp. 2525-2531, Oct 2006.

[27] S. Oda, "NeoSilicon materials and silicon nanodevices," *Materials Science and Engineering B-Solid State Materials for Advanced Technology,* vol. 101, pp. 19-23, Aug 15 2003.

[28] N. Petermann, N. Stein, G. Schierning, R. Theissmann, B. Stoib, M. S. Brandt*, et al.*, "Plasma synthesis of nanostructures for improved thermoelectric properties," *Journal of Physics D-Applied Physics,* vol. 44, May 4 2011.

[29] J. K. Lee, K. B. Smith, C. M. Hayner, and H. H. Kung, "Silicon nanoparticles-graphene paper composites for Li ion battery anodes," *Chemical Communications,* vol. 46, pp. 2025-2027, 2010.

[30] C. K. Chan, H. L. Peng, G. Liu, K. McIlwrath, X. F. Zhang, R. A. Huggins*, et al.*, "High-performance lithium battery anodes using silicon nanowires," *Nature Nanotechnology,* vol. 3, pp. 31-35, Jan 2008.

[31] A. I. Hochbaum, R. K. Chen, R. D. Delgado, W. J. Liang, E. C. Garnett, M. Najarian*, et al.*, "Enhanced thermoelectric performance of rough silicon nanowires," *Nature,* vol. 451, pp. 163-U5, Jan 10 2008.

[32] J. M. Spurgeon, S. W. Boettcher, M. D. Kelzenberg, B. S. Brunschwig, H. A. Atwater, and N. S. Lewis, "Flexible, Polymer-Supported, Si Wire Array Photoelectrodes," *Advanced Materials,* vol. 22, pp. 3277-+, Aug 10 2010.

[33] D. S. English, L. E. Pell, Z. H. Yu, P. F. Barbara, and B. A. Korgel, "Size tunable visible luminescence from individual organic monolayer stabilized silicon nanocrystal quantum dots," *Nano Letters,* vol. 2, pp. 681-685, Jul 2002.

[34] C. Lam, Y. F. Zhang, Y. H. Tang, C. S. Lee, I. Bello, and S. T. Lee, "Large-scale synthesis of ultrafine Si nanoparticles by ball milling," *Journal of Crystal Growth,* vol. 220, pp. 466-470, Dec 2000.

[35] G. S. Fu, Y. L. Wang, L. Z. Chu, Y. Zhou, W. Yu, L. Han*, et al.*, "The size distribution of Si nanoparticles prepared by pulsed-laser ablation in pure He, Ar or Ne gas," *Europhysics Letters,* vol. 69, pp. 758-762, Mar 2005.

[36] T. Yoshida, S. Takeyama, Y. Yamada, and K. Mutoh, "Nanometer-sized silicon crystallites prepared by excimer laser ablation in constant pressure inert gas," *Applied Physics Letters,* vol. 68, pp. 1772-1774, Mar 25 1996.

[37] M. A. Lieberman and A. J. Lichtenberg, *Principles of plasma discharges and materials processing*, 2nd ed. Hoboken, N.J.: Wiley-Interscience, 2005.

[38] U. Kortshagen and U. Bhandarkar, "Modeling of particulate coagulation in low pressure plasmas," *Physical Review E,* vol. 60, pp. 887-898, Jul 1999.

[39] B. A. Bolto, R. Mcneill, and D. E. Weiss, "Electronic Conduction in Polymers .3. Electronic Properties of Polypyrrole," *Australian Journal of Chemistry,* vol. 16, pp. 1090-&, 1963.

[40] H. Shirakawa, E. J. Louis, A. G. Macdiarmid, C. K. Chiang, and A. J. Heeger, "Synthesis of Electrically Conducting Organic Polymers - Halogen Derivatives of Polyacetylene, (Ch)X," *Journal of the Chemical Society-Chemical Communications,* pp. 578-580, 1977.

[41] K. M. Molapo, P. M. Ndangili, R. F. Ajayi, G. Mbambisa, S. M. Mailu, N. Njomo*, et al.*, "Electronics of Conjugated Polymers (I): Polyaniline," *International Journal of Electrochemical Science,* vol. 7, pp. 11859-11875, Dec 2012.

[42] S. Kuwabata, N. Tsumura, S. Goda, C. R. Martin, and H. Yoneyama, "Charge-discharge properties of composite of synthetic graphite and poly(3-n-hexylthiophene) as an anode active material in rechargeable lithium-ion batteries," *Journal of the Electrochemical Society,* vol. 145, pp. 1415-1420, May 1998.

[43] B. Veeraraghavan, J. Paul, B. Haran, and B. Popov, "Study of polypyrrole graphite composite as anode material for secondary lithium-ion batteries," *Journal of Power Sources,* vol. 109, pp. 377-387, Jul 1 2002.

[44] M. Gaberscek, M. Bele, J. Drofenik, R. Dominko, and S. Pejovnik, "Improved carbon anode properties: pretreatment of particles in polyelectrolyte solution," *Journal of Power Sources,* vol. 97-8, pp. 67-69, Jul 2001.

[45] H. Shirakawa, "The discovery of polyacetylene film: The dawning of an era of conducting polymers (Nobel lecture)," *Angewandte Chemie-International Edition,* vol. 40, pp. 2575-2580, 2001.

[46] M. Kim, S. Cho, J. Song, S. Son, and J. Jang, "Controllable Synthesis of Highly Conductive Polyaniline Coated Silica Nanoparticles Using Self-Stabilized Dispersion Polymerization," *Acs Applied Materials & Interfaces,* vol. 4, pp. 4603-4609, Sep 2012.

[47] S. C. Raghavendra, S. Khasim, M. Revanasiddappa, M. V. N. A. Prasad, and A. B. Kulkarni, "Synthesis, characterization and low frequency a.c. conduction of polyaniline/fly ash composites," *Bulletin of Materials Science,* vol. 26, pp. 733-739, Dec 2003.

[48] G. A. Rimbu, I. Stamatin, C. L. Jackson, and K. Scott, "The morphology control of polyaniline as conducting polymer in fuel cell technology," *Journal of Optoelectronics and Advanced Materials,* vol. 8, pp. 670-674, Apr 2006.

[49] H. Biederman and D. Slavinska, "Plasma polymer films and their future prospects," *Surface & Coatings Technology,* vol. 125, pp. 371-376, Mar 2000.

[50] W. He, Z. G. Guo, Y. K. Pu, L. T. Yan, and W. J. Si, "Polymer coating on the surface of zirconia nanoparticles by inductively coupled plasma polymerization," *Applied Physics Letters,* vol. 85, pp. 896-898, Aug 9 2004.

[51] S. Sivaraman and M. R. Anantharaman, "Determination of charge carrier transport in radio frequency plasma polymerized aniline thin films," *Journal of Physics D-Applied Physics,* vol. 43, Feb 10 2010.

[52]   K. Kanamura, Y. Kawai, S. Yonezawa, and Z. Takehara, "Diffusion Behavior of Anions in Polyaniline during Electrochemical Undoping .2. Effect of the Preparation Conditions of Polyaniline on the Diffusion-Coefficient of Bf4-," *Journal of Physical Chemistry,* vol. 98, pp. 2174-2179, Feb 24 1994.

[53]   H. Yasuda, *Plasma polymerization*. Orlando: Academic Press, 1985.

[54]   X. Y. Gong, L. M. Dai, A. W. H. Mau, and H. J. Griesser, "Plasma-polymerized polyaniline films: Synthesis and characterization," *Journal of Polymer Science Part a-Polymer Chemistry,* vol. 36, pp. 633-643, Mar 1998.

[55]   J. G. Wang, K. G. Neoh, L. P. Zhao, and E. T. Kang, "Plasma polymerization of aniline on different surface functionalized substrates," *Journal of Colloid and Interface Science,* vol. 251, pp. 214-224, Jul 1 2002.

[56]   L. Mangolini and U. Kortshagen, "Plasma-assisted synthesis of silicon nanocrystal inks," *Advanced Materials,* vol. 19, pp. 2513-+, Sep 17 2007.

[57]   F. T. Liu, K. G. Neoh, E. T. Kang, S. Li, H. S. Han, and K. L. Tan, "Effects of crosslinking on polyaniline films' doping behavior and degradation under weathering," *Polymer,* vol. 40, pp. 5285-5296, Sep 1999.

Chapter 2 Synthesis and Characterization Techniques of Group IV Nanoparticles

Overview

Experimental design for silicon nanoparticle synthesis and polymerization process will be presented in this chapter. Material characterization techniques also will be discussed. In order to characterize the samples, Transmission electron microscopy (TEM), Raman spectroscopy, and X-ray Diffraction (XRD), and Energy Dispersive Spectrometry (EDS) are used to analyze the structure of the particles. In order to analyze the surface chemistry, and surface morphology, Fourier transform infrared spectroscopy (FTIR), X-ray photoelectron spectroscopy (XPS), and scanning electron microscopy (SEM) are performed for thus thesis.

Experimental Design and Sample Preparation

Non-thermal plasma system basically consists of the following parts: pyrex tube, copper electrodes, power source, T-type matching network, vacuum fittings, bubbler system to supply the chlorinated silicon precursor and monomer for the polymerization process, butterfly valve to control the system pressure, and liquid nitrogen trap to condense the organic materials.

Experimental Design

Silicon nanoparticles have been synthesized using non-thermal plasma design which is described by Mangolini et al. [1]. The plasma reactor is modified to increase the nanomaterial production rate. Further modifications are done to synthesize also silicon-germanium alloy nanoparticles, and for the plasma polymerization process.

Figure 2-1 shows the schematic view of the non-thermal plasma reactor which is used to produce silicon nanoparticles. Silicon tetrachloride ($SiCl_4$) and silane (SiH_4) are
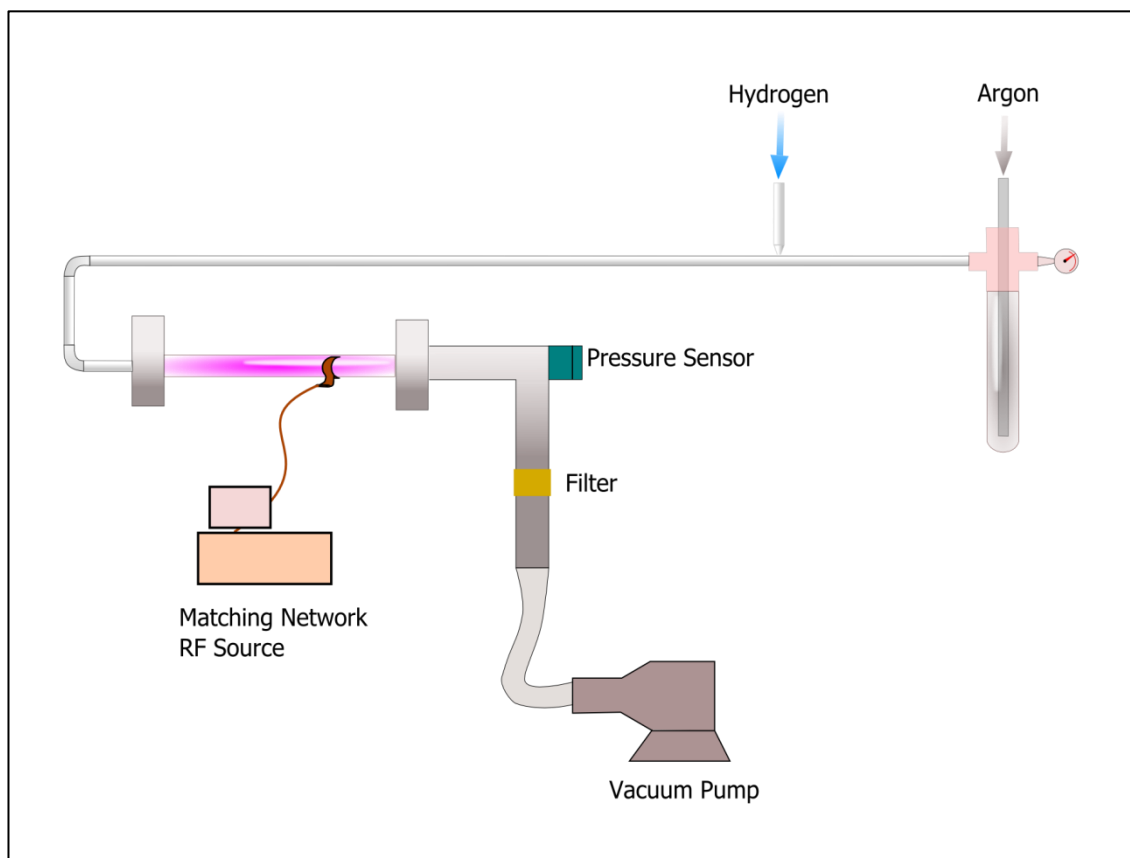
Figure 2-1 Schematic view of non-thermal plasma reactor using chlorinated precursor.

used as silicon precursors. The effects of precursor choice on particle properties will be discussed in details in chapter 3. For the chlorinated precursor case, silicon tetrachloride is supplied using a bubbler system designed to control independently the bubble pressure and the flow rate of the gas carrier flowing through the bubbler. Silicon nanoparticles that will be discussed more in details in chapter 3 are synthesized with bubbler pressure equal to 100 kPa. The bubbler is maintained in a water-ice bath to keep the temperature constant, which is critical to ensure reproducibility.

For hydrogenated precursor case, silane is supplied to the system, which is shown in Figure 2-2, from a compressed tank at a concentration of 1.37%, balance argon. For both cases, one plasma reactor is used to produce silicon nanoparticles. The plasma reactor consists of pyrex tube. The length of the reactor is 30 cm and the outer diameter is equal to 2.54 cm. The pyrex tube is connected to the Ultra-Torr vacuum fittings. The plasma is generated between a copper ring electrode wrapped around the tube and one of the Ultra-Torr flanges, typically the one on the pump side of the system. The copper ring electrode is placed 7 cm apart from the nearest metal flange. The electrical input power is supplied to the system using a 13.56 MHz power supply. T-type matching network is used to minimize the reflected power. Butterfly valve is used to automatically control the reactor pressure. The reactor pressure is settled as equal to 3.5 Torr for the samples discussed in chapter 3. Rotary pump is used to evacuate the system.

In order to produce silicon-germanium alloy nanoparticles, the non-thermal plasma system is modified by adding another precursor delivery system which is second bubbler system that is for germanium tetrachloride ($GeCl_4$). The schematic view of modified system is shown in Figure 2-3. $GeCl_4$ is used as a germanium precursor. The
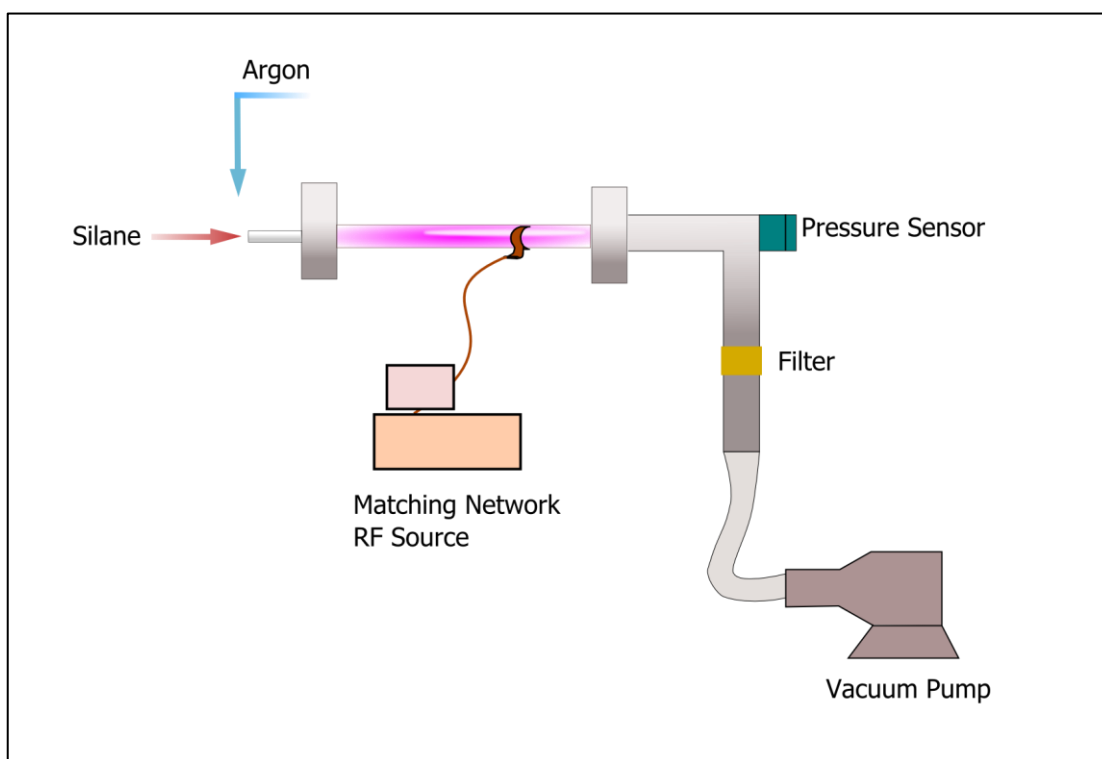
Figure 2-2 schematic view of non-thermal plasma reactor using hydrogenated precursor.

overall system is then comprised of two bubblers, which is represented in Figure 2-4, with independent control over their pressures and over the flow rates of each carrier gas. Hydrogen is separately added to the reactor inlet line. The effects of hydrogen will be discussed in chapter 3. The silicon tetrachloride bubbler is kept in an ice bath while the germanium tetrachloride bubbler is operated at room temperature.

Silicon nanoparticles and silicon-germanium alloy nanoparticles are produced using one plasma reactor. For the polymerization process, non-thermal plasma system is modified by adding another plasma reactor for the polymerization process. Schematic view of plasma polymerization process in indicated in Figure 2-5 Polymerized silicon nanoparticles were synthesized using continuous flow non-thermal plasma system which consists of two serially connected plasma reactors. Immediately after the silicon nanoparticles are synthesized in the first reactor [1, 2], they are dragged into a second
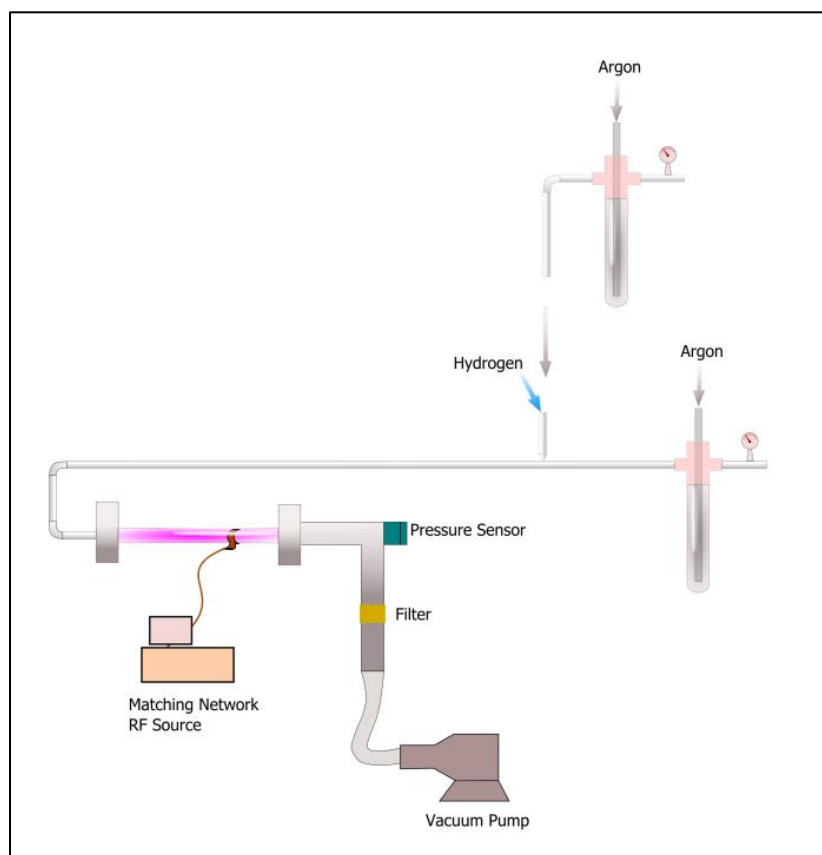
Figure 2-3 Schematic view of non-thermal plasma reactor which is used to synthesize silicon-germanium alloy nanoparticles using chlorinated precursors
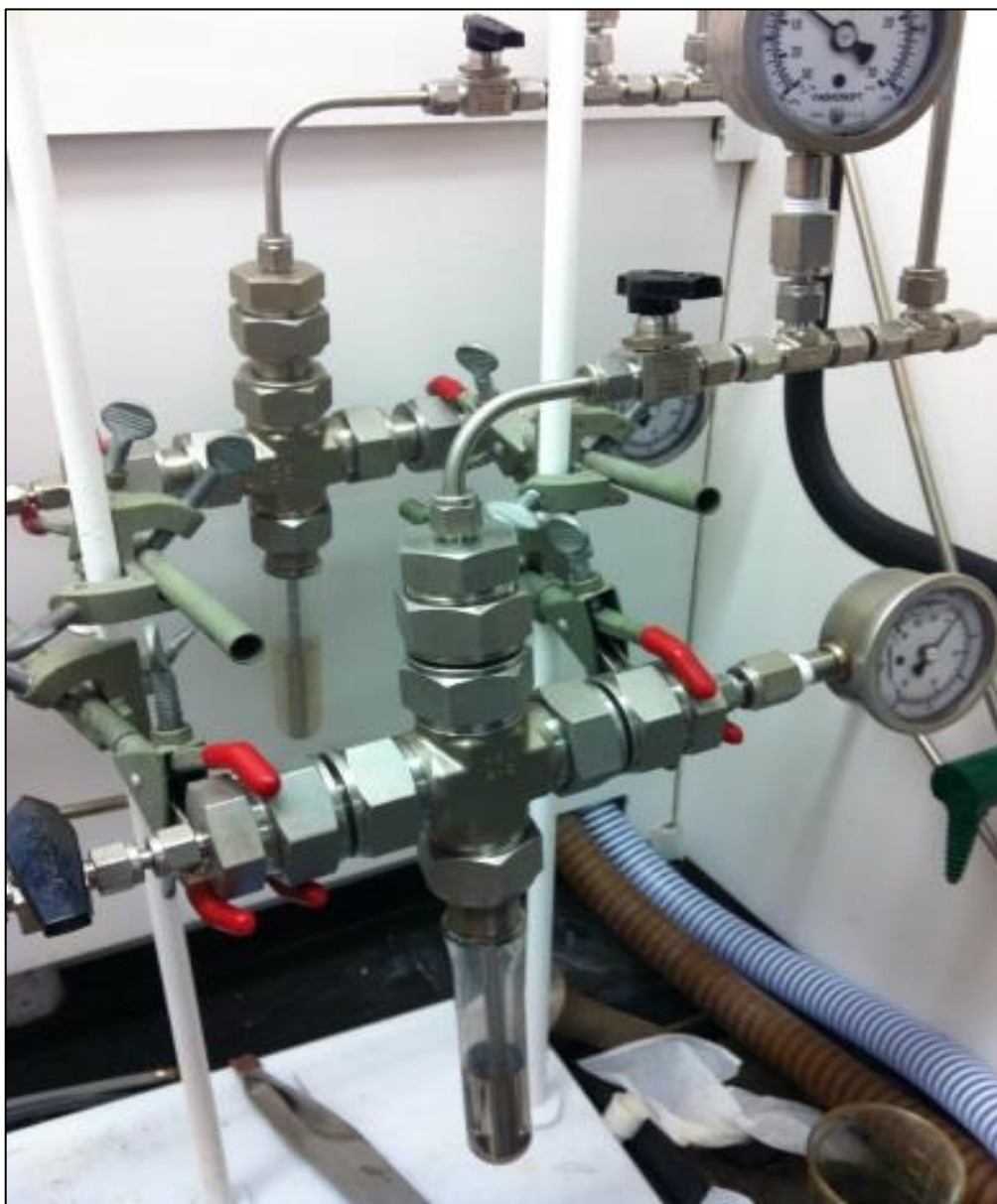
Figure 2-4 Bubbler systems both connected to non-thermal plasma system
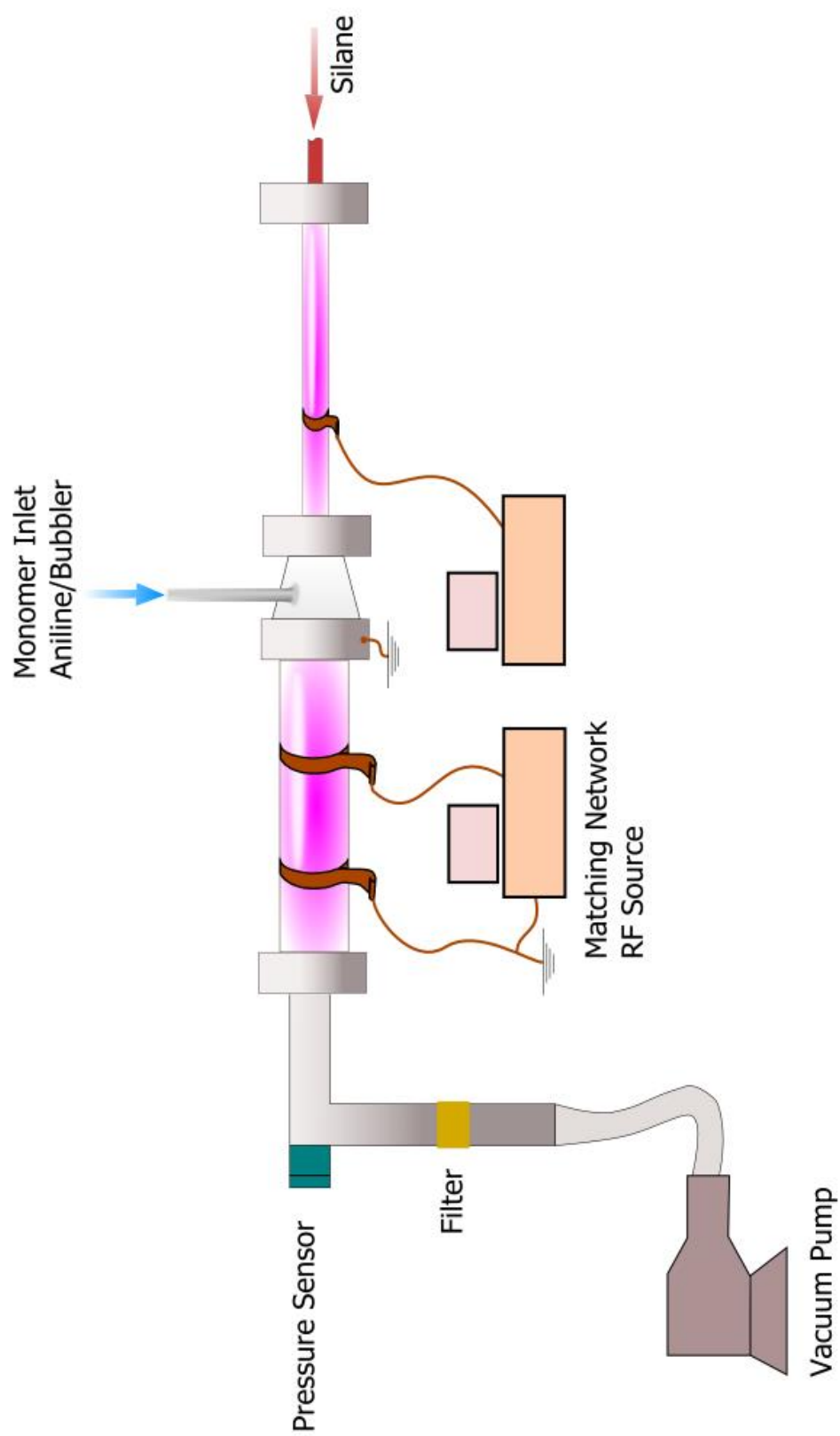
Figure 2-5 Schematic view of plasma polymerization process.

reactor and coated in a second discharge. For this case bubbler system is used to carry the evaporated monomer and connected to the second plasma reactor. The bubbler pressure is kept constant and equal to 30 kPa (absolute pressure). In order to control and increase the aniline monomer flow rate, the bubbler is placed in an oil bath kept at 60 °C and 140 sccm of argon flows through the aniline bubbler. Hydrogen can also be added to the second non-thermal plasma system via a separate supply line. Figure 2-6 represents the experimental setup for the plasma polymerization process which has two stage plasma reactor.

Powder Collection

Silicon nanoparticles, silicon-germanium nanoparticles and polymerized silicon nanoparticles are collected in powder form. The powder is collected by filtering method. After nucleation in the gas-phase, the powder is collected onto a stainless steel filter which is placed downstream of the plasma. In order to avoid any contamination, stainless steel filter is cleaned by sonication in methanol for ten minutes. Figure 2-7 (a) indicates the flat filter which is prepared and cleaned to collect several milligrams of powder Figure 2-7(b) shows the silicon nanoparticles that are collected onto the flat filter and Figure 2-7(c) indicates tubular shape filter and (d) hundreds of milligrams of
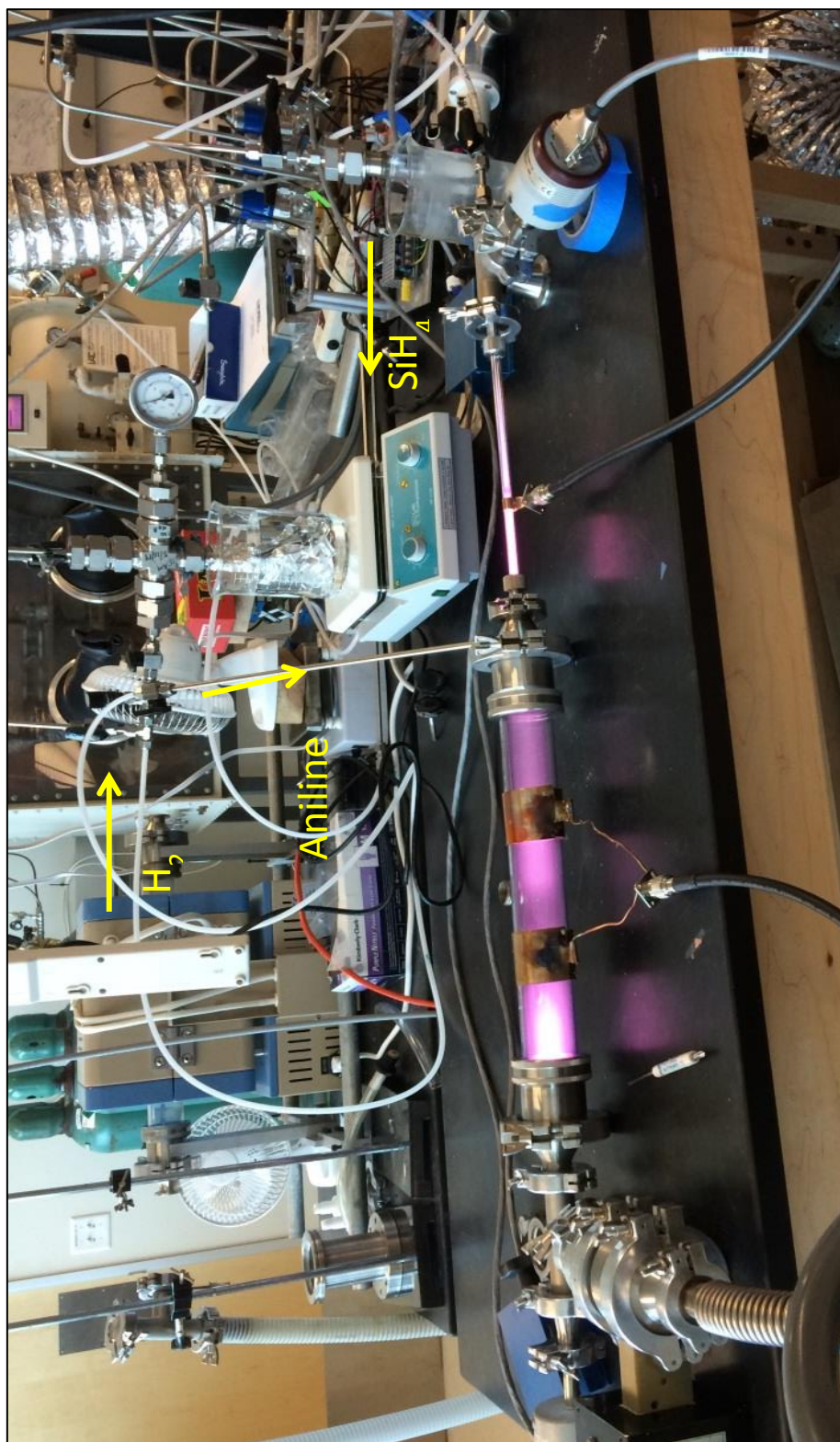
Figure 2-6 Experimental setup plasma polymerization process

silicon nanoparticles collected into the tubular shape filter. Figure 2-8 represents the

experimental setup to produce silicon nanoparticles using chlorinetaed precorsor.
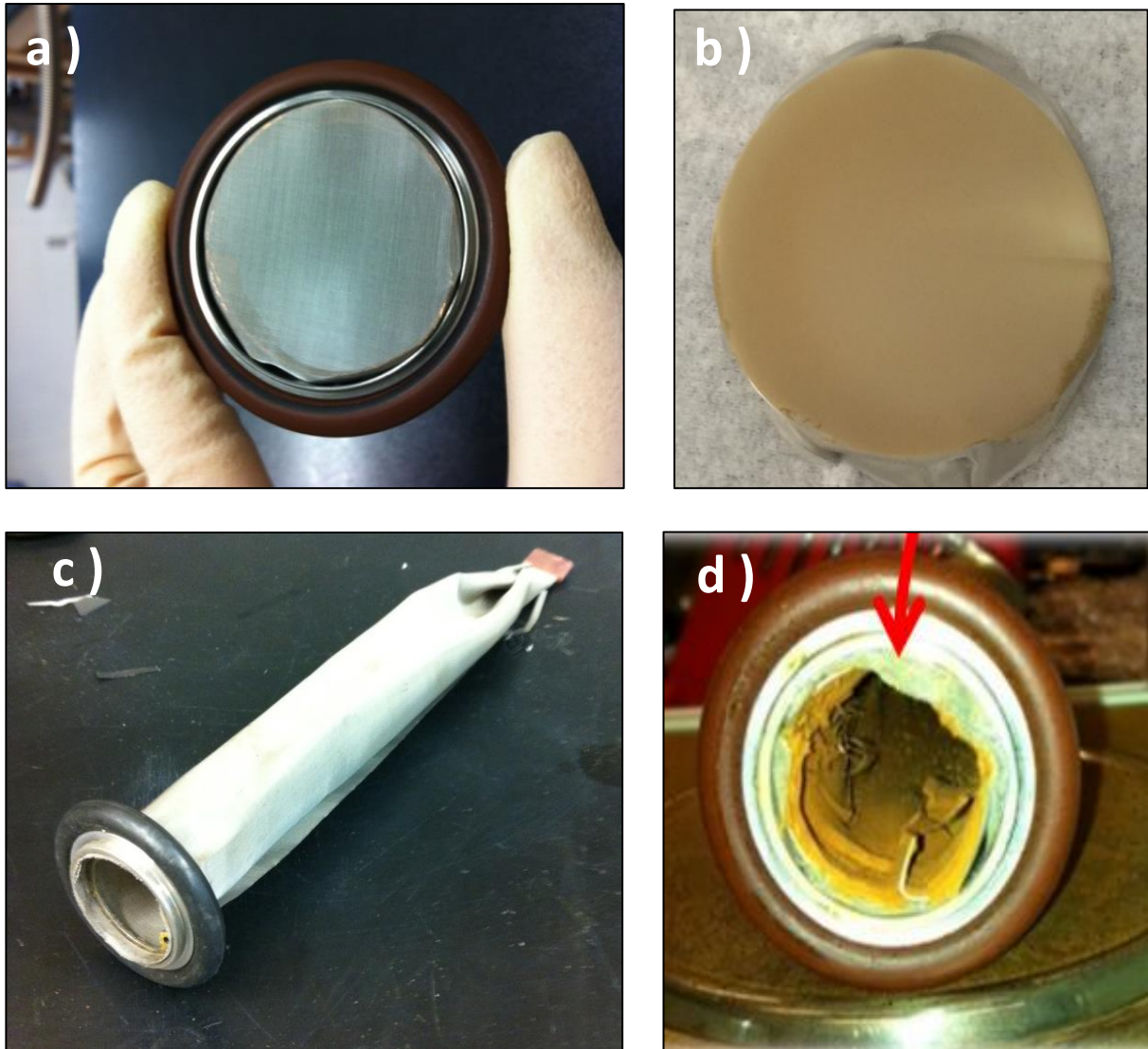
Figure 2-7 a) Stainless steel flat filter b) Silicon powder collected on flat filter c) Stainless steel tubular shape filter d) Silicon powder collected in tubular shape filter

Sample Characterization

In order to determine the size, structure, composition and chemical nature of the nanoparticles, extensive material characterization techniques are performed on the produced powders. X-ray diffraction (XRD), Raman, Scanning electron microscopy (SEM), Energy dispersive spectroscopy (EDS), and Transmission electron microscopy (TEM) are performed to assess size, shape, structure and composite of particles. Fourier transform infrared spectroscopy (FTIR) and X-ray photoelectron spectroscopy (XPS) are used to determine the surface configuration of particles.

Figure 2-8 Experimental setup for non-thermal plasma system

Transmission Electron Microscopy

Transmission electron microscopy (TEM) is one of the crucial tools for the nanocharacterization that allows to determine the particle shape, particle size, size particle distribution and structure.

TEM is performed on a Tecnai T12 transmission electron microscope that operates with 120 kV of accelerating voltage. High resolution TEM images are determined by using 300 kV accelerating voltage. Lattice fringes of the 111 plane of silicon can be determine by TEM. TEM samples are prepared in two different ways. They are prepared by placing lacey carbon grids downstream plasma into the vacuum systems, along the exhaust flow pathway, and nanoparticles are collected as they diffuse onto the TEM grids for couple of seconds. Alternatively, a filter consisting of a fine stainless steel mesh is placed at the reactor outlet to collect several milligrams of powder and then the particles are dispersed in methanol and sonicated for 10 minutes. TEM samples are prepared by drop-casting a dispersion of particles onto lacey carbon grids.

Scanning Electron Microscopy

The morphology of nanoparticles and surface topography are investigated by using Scanning electron microscopy (SEM). SEM analyses are performed using Nova NanoSEM 450 and XL30 FEG instrument which is shown in Figure 2-9. In order to

prepare the anode electrodes, which are used for lithium-ion batteries, to determine the surface properties, 40 mg of Si/polymer particles are added to 10 mg of multiwall carbon nanotubes (MWCNTs) to enhance the electrical conductivity of the layer. The Si/polymer and MWCNTs mixture is dispersed in ethanol and ultrasonicated for 20 min. Copper foil is used as substrate and coated by drop-casting. Some of the electrode
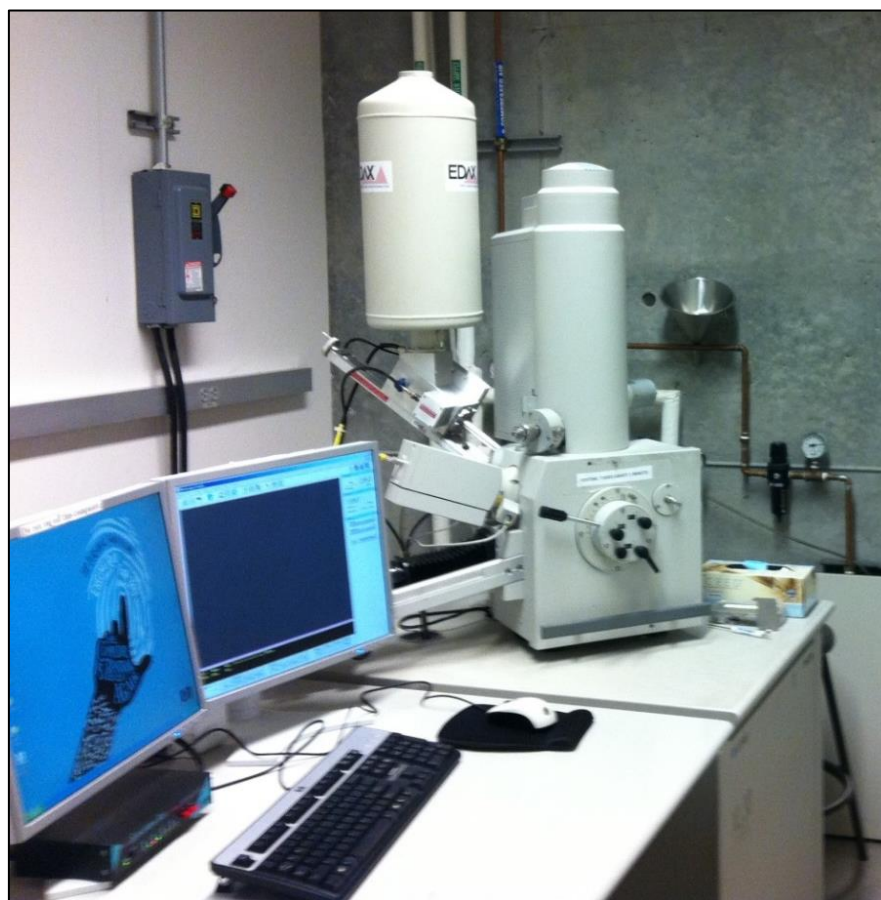
Figure 2-9 Scanning Electron Microscopy (XL 30 FEG)

samples are annealed at under argon flow in a vacuum tube furnace capable of reaching 1000 °C. The differences of the surface properties of electrodes which are mixed with only silicon nanoparticles as control experiment, silicon/polymer nanoparticles, and

annealed silicon/polymer nanoparticles is obtained by SEM analysis. The detailed results will be discussed in chapter 5.

X-Ray Diffraction

X-ray diffraction (XRD) is performed on the produced powders to investigate structural analysis. Powder diffraction is performed on a Bruker D8-Advance instrument using the Cu Kα line at a wavelength of 1.5406 Å. The scanning angle (2Ө) is varied between 10 and 90°. In order to prepare XRD samples, a filter consisting of a fine stainless steel mesh which is placed at the reactor outlet to collect several milligrams of powder that is necessary for XRD characterization. XRD samples are prepared by drop-casting the particle dispersion in chloroform onto a zero-background substrate. Alternatively, the produced powder is pressed onto the zero background without using any chemicals. Lattice spacing, the distance between lattice planes d, can be determined using the Bragg's Law formula [1].

$$2dsin\theta = n\lambda$$

In the formula, λ indicates the wavelength of the incident X-ray, Ө represents the angle between incident and x-ray, and n represents the reflection order which is an integer. Particle size can be determined using the Debye-Scherrer relation [2];

$$D = \frac{k\lambda}{\beta cos\theta}$$

where D is the particle size and k is Scherrer constant which is 0.89. λ represents the X-ray wavelength, β represents the full width half-maximum, and ϴ indicates the Bragg diffraction angle.

Raman Spectroscopy

Raman spectroscopy can be used to investigate the structural analysis and chemical states of the bonds in materials by providing information about molecular vibrations. In this thesis, Raman spectroscopy was performed on a Dilor XY system using a 532 nm laser source. In order to prepare Raman spectroscopy samples, the flat stainless steel filter is placed at the exhaust of the plasma system and several milligrams of nanoparticles are collected. The collected powder is pressed onto a glass slide.

Energy Dispersive Spectrometer

Energy dispersive spectroscopy (EDS) can be used to investigate the chemical characteristics and qualitative elemental analysis on the surface of the sample. In this thesis, the elemental composition is determined by using SEM-EDS XL30 FEG which is shown in Figure 2-9. The preparation procedure of EDS samples are same as SEM samples. Nanoparticles are collected onto the flat filter and dispersed in methanol and ultrasonicated for 10 minutes. Copper foil is used as substrate and is coated with dispersion by drop-casting.

Fourier Transform Infrared Spectroscopy

Fourier Transform Infrared Spectroscopy (FTIR) can be used to determine the surface configuration. In this thesis FTIR is used to analyze the chemical bonding and functional groups in the sample. FTIR analysis is performed using a Newport-Oriel modular interferometer which is shown in Figure 2-10. Although, cadmium telluride (MCT) is more commonly used detector for FTIR, it is not sensitive enough below 600 cm^{-1}, where absorption from Si–Cl bonds is expected. Therefore, Newport-Oriel modular interferometer which is equipped with a deuterated triglycine sulfate (DTGS) detector is used for extended sensitivity between 400 and 5000 cm^{-1}.

In this thesis, the samples are prepared and analyzed in several ways. For precursor effect studies, the samples were collected in situ onto a KBr pellet. In situ FTIR was performed by splitting the flow at the reactor outlet into two parts. While one part is collected either onto TEM grids or on filters for ex situ analysis, the other part is sent through a 1 mm orifice and into an evacuated six-way cross. The particles are accelerated and impacted onto a potassium bromide (KBr) target, which is placed in the optical pathway of an IR beam. The absorption was measured under vacuum without the samples ever being exposed to air.

For the FTIR analysis of polymerized nanoparticles, powder is collected onto the filter and dispersed in chloroform by ultrasonication and by drop-casting onto a zinc selenide ATR crystal. The absorption is monitored as the solvent evaporates and the

data acquisition is initiated only after the disappearance of any feature related to chloroform.

X-ray Photoelectron Spectroscopy

X-ray photoelectron spectroscopy (XPS) is used to determine the composition and the chemical nature of the produced powders. In this thesis, XPS is performed on a Kratos Axis Ultra^{DLD} XPS system equipped with an Al Kα monochromated x-ray source for the core/shell silicon/polyaniline nanoparticles which will be discussed more in details in chapter 5. In order to prepare the XPS samples, stainless steel tubular shape filter is placed at the exhaust of the two-reactor plasma system. 10 milligrams of powder is
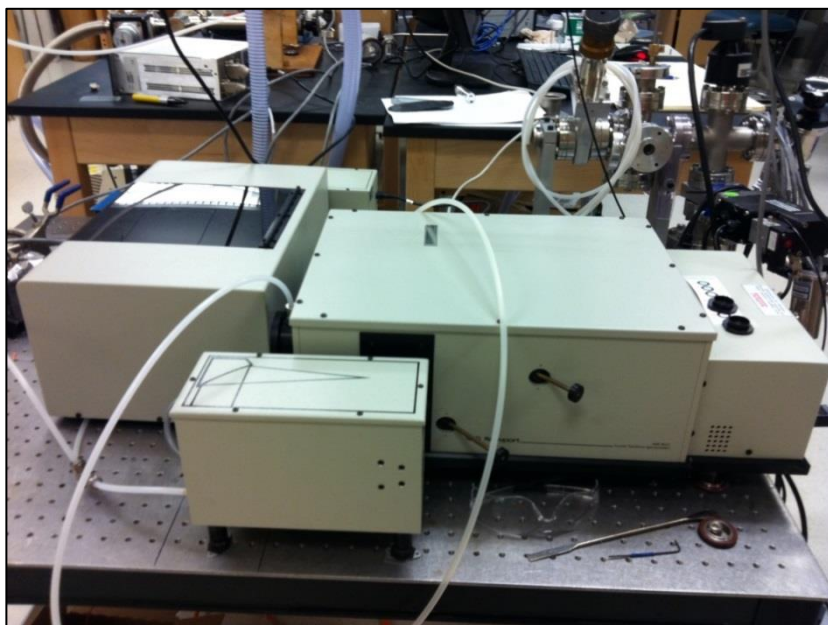
Figure 2-10 Fourier Transform Infrared Spectroscopy

collected into the filter and kept in a vial for XPS analysis.

Size Distribution

Particle size distribution plays an important role for the quality, process and development of the devices. In order to determine the size distribution, agglomeration, and concentration of the nanoparticles by low pressure cascade impactor or differential mobility analyzer (DMA) which is also known as electrostatic classifier. Differential mobility analyzer is an aerosol measurement technique that separates the charged particles based on their electrical mobility [3]. Although it is commonly used technique, analyzing the nanoparticles which are less than 2 nm becomes challenging. In this thesis, particle size and size distribution for the silicon nanoparticles and silicon/polymer core/shell nanoparticles are determined by the analyzing the TEM images. Bright field TEM images are used to determine the sizes of at least 100 particles has been measured. The average particle size is estimated by fitting the distribution with a lognormal function.

Non-thermal Plasma Synthesis

Non-thermal plasma technique has unique properties that differentiate it from other gas-phase nanoparticle synthesis techniques. High production rate, producing negatively charged nanoparticles, and selective nanoparticle heating are the several

advantages of non-thermal plasma system that enhance the quality of nanoparticle based devices.

Nucleation

In non-thermal plasma system, electrons with the temperature of a few eV dissociate the precursor gas molecule. With dissociation of gas molecules, neutral and charged radicals are formed which cause the formation of nanoparticles. Therefore, nucleation process is different for every material due to the different chemical reactions.

During the producing of silicon nanoparticles using hydrogenated precursor silane (SiH$_4$), silane clusters with gaining electron they become negative ions which are also called anions. These negatively charged clusters that form in plasma trigger the nucleation process [4]. Howling et al. showed that positively charged clusters and neutral radicals diffuse to the negatively charged plasma reactor walls as opposed to the anions. Hence, the positive clusters and neutral radicals do not have a chance to grow, but the anions grow in size being exposed to the plasma [5]. Particle nucleation reaction can be shown as [6]:

$$Si_nH_{2n+1}^- + SiH_4 \rightarrow Si_{n+1}H_{2n+3}^- + H_2$$
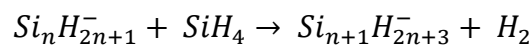
As shown in the reaction, nucleation occurs based on the negatively charged clustering. On the other hand, Watanabe and his coworkers indicated that the nucleation process is based on the neutral reactions by inserting of SiH_2 into neutral clusters [7, 8]. Another nucleation model is developed by Gallagher [9, 10]. Based on his theory, SiH_3 plays an important role for clustering. The clustering starts with attaching electron to SiH_3.

Nanoparticle Charging

Pyrolysis and photolysis are commonly used gas phase nanoparticle synthesis techniques. Although small size silicon nanocrystals can be produced using these techniques, they face to several limitations. For instance, particle agglomeration, which is caused by the neutral particles, and low production rate become challenges for these types of techniques. Low production rate is because of the loss of nanoparticles at the reactor wall which caused by diffusivity. These limitations can overcome by using non-thermal plasma techniques. The particles that are produced using non-thermal plasma system are unipolar negatively charged which prevents the particle agglomeration. Particle charging is a very important property of non-thermal plasmas. In non-thermal plasma the electron temperature, which is between approximately 2 to 5 eV (20,000 to 50,000 K) is much higher than ion temperature, which is close to room temperature. Due to the high thermal velocity of electrons, the plasma reactor walls and the surface of the particles are both negatively charged. Therefore, the electrostatic repulsion of

negatively charged particles prevents particle agglomeration and wide range particle size distribution [11, 12].

Particle charging is explained by the Orbital Motion Limited (OML) theory [13]. The average particle charge can be calculated based on the theory. The following equations shows the electron and ion currents.

$$I_e = \frac{1}{4} e n_e S \sqrt{\frac{8 k_B T_e}{\pi m_e}} \; exp - \frac{e\,|\Phi|}{k_B T_e} \quad , \quad \Phi < 0$$

$$I_i = \frac{1}{4} e n_i S \sqrt{\frac{8 k_B T_i}{\pi m_i}} \; exp - \frac{e\,|\Phi|}{k_B T_i} \quad , \quad \Phi < 0$$

In the equation 1, I_e represents the electron current, S represents particle surface area, e indicates the elementary charge, and k_B is Boltzman constant, m_e shows the electron mass, T_e is electron temperature, and Φ represents the particle potential. In the equation 2, I_i represents the ion current, S represents particle surface area, e indicates the elementary charge, and k_B is Boltzman constant, m_i shows the ion mass, T_i is ion temperature, and Φ represents the particle potential. The average particle charge (Q) can be calculated by using the following formula [11],

$$Q = 4\pi\varepsilon_0 R_p \Phi$$

where ε_0 is the vacuum dielectric constant and R_p is the radius of the particle.

References

[1]   C. Kittel, *Introduction to solid state physics*, 8th ed. Hoboken, NJ: Wiley, 2005.

[2]   T. Pradeep, *Nano : the essentials : understanding nanoscience and nanotechnolgy*. New York ; London: McGraw-Hill, 2008.

[3]   M. Hosokawa, *Nanoparticle technology handbook*, 1st ed. Amsterdam, Netherlands ; Boston Mass.: Elsevier, 2007.

[4]   M. T. Swihart, "Electron affinities of selected hydrogenated silicon clusters (SixHy, x=1-7, y=0-15) from density functional theory calculations," *Journal of Physical Chemistry A,* vol. 104, pp. 6083-6087, Jun 29 2000.

[5]   A. A. Howling, L. Sansonnens, J. L. Dorier, and C. Hollenstein, "Time-Resolved Measurements of Highly Polymerized Negative-Ions in Radio-Frequency Silane Plasma Deposition Experiments," *Journal of Applied Physics,* vol. 75, pp. 1340-1353, Feb 1 1994.

[6]   J. Perrin, C. Bohm, R. Etemadi, and A. Lloret, "Possible routes for cluster growth and particle formation in RF silane discharges," *Plasma Sources Science & Technology,* vol. 3, pp. 252-261, Aug 1994.

[7]   Y. Watanabe, M. Shiratani, T. Fukuzawa, H. Kawasaki, Y. Ueda, S. Singh*, et al.*, "Contribution of short lifetime radicals to the growth of particles in SiH4 high frequency discharges and the effects of particles on deposited films," *Journal of Vacuum Science & Technology A,* vol. 14, pp. 995-1001, 1996.

[8]   T. Fukuzawa, K. Obata, H. Kawasaki, M. Shiratani, and Y. Watanabe, "Detection of particles in rf silane plasmas using photoemission method," *Journal of applied physics,* vol. 80, pp. 3202-3207, 1996.

[9]   A. Gallagher, "Model of particle growth in silane discharges," *Physical Review E,* vol. 62, p. 2690, 2000.

[10]   A. Gallagher, A. A. Howling, and C. Hollenstein, "Anion reactions in silane plasma," *Journal of Applied Physics,* vol. 91, pp. 5571-5580, May 1 2002.

[11]   M. Sankaran, *Plasma processing of nanomaterials*. Boca Raton: CRC Press, 2012.

[12]   U. Kortshagen and U. Bhandarkar, "Modeling of particulate coagulation in low pressure plasmas," *Physical Review E,* vol. 60, pp. 887-898, Jul 1999.

[13]   J. E. Allen, B. M. Annaratone, and U. de Angelis, "On the orbital motion limited theory for a small body at floating potential in a Maxwellian plasma," *Journal of Plasma Physics,* vol. 63, pp. 299-309, May 2000.

Chapter 3 Silicon nanocrystal production through non-thermal plasma synthesis: a comparative study between silicon tetrachloride and silane precursors

Overview

Synthesis and characterization of silicon nanoparticles which are using non-thermal plasma reactor will be presented in this chapter. Silicon tetrachloride ($SiCl_4$) and silane (SiH_4) are used as silicon precursors to produce silicon nanoparticles. Direct comparison between the use of a chlorinated precursor and the use of silane, and discussion the consequences of precursor choice on both the process parameters and the material properties will be also investigated in this chapter. Surface modification of silicon nanoparticles and characterization of functionalized particles will be discussed in chapter 5. presence of chlorine at the particle surface, and possibly also within the particle core, has important consequences on the crystallization rate, which implies that a higher power is required to produce high-quality material when silicon tetrachloride is the precursor of choice. Particles produced from silicon tetrachloride are very prone to oxidation in air, indicating that even more special care will have to be taken during the processing of this material for any of its potential applications compared to the case of the hydrogen terminated particles. The presented work in this chapter was published in Nanotechnology [1].

Introduction

The rapidly increasing interest in silicon nanostructures is motivated by important advantages of this material compared to other semiconductors commonly investigated in the broad field of nanotechnology, such as II–VI semiconductors and metal chalcogenides. Silicon is the second most abundant element on the planet; it is relatively cheap and it is non-toxic in its bulk form. Silicon-based nanostructures are potentially compatible with already developed integrated circuit (IC) architectures and/or microfabrication schemes. Several types of silicon-based nanostructure are under intense investigation. For instance, quantum confined silicon in the form of either porous silicon [2], nanoparticles dispersed in a dielectric matrix [3], or free standing quantum dots [4] is promising for many applications including the fabrication of highly efficient light emitting devices [5] or photovoltaic devices [6]. Free standing silicon nanocrystals are potential building blocks of single particle transistors [7] and a variety of other devices [8]. Silicon nanocrystals have also been used to produce bulk nanostructured silicon samples for thermoelectric applications [9], and have been integrated into the anode of lithium-ion batteries [10]. Silicon nanowires are also attracting increasing interest for both thermoelectric and photovoltaic applications [11-13].

In this chapter, we focus on the synthesis of free standing silicon nanocrystals using different precursors with sizes below 10 nm. The continuous flow, non-thermal plasma reactor described in [14] is one of the possible synthetic approaches for the

production of high-quality silicon nanocrystals. Other approaches include gas-phase techniques, such as laser-induced [15] or furnace [16] pyrolysis of silane, and liquid-phase techniques that use silicides [17] as precursors, or thermal reduction of silsesquioxanes [18]. This report focuses on the non-thermal plasma synthesis of nanocrystals. While the process described in [14] uses silane (SiH_4) as a precursor, we address the feasibility of another precursor, silicon tetrachloride ($SiCl_4$), for the production of silicon nanocrystals in a non-thermal plasma reactor. The main advantage of silicon tetrachloride is that it is significantly cheaper than silane. For the same reason, silicon tetrachloride has also attracted interest as a silane replacement for the growth of amorphous silicon thin films [19]. Chlorinated precursors such as germanium tetrachloride ($GeCl_4$) have also already been used for the non-thermal plasma synthesis of germanium nanocrystals [20]. Previous results on the synthesis of silicon nanocrystals starting from silicon tetrachloride have been recently published by Gresback et al in [21]. The authors use a very high frequency (VHF, 70 MHz excitation) plasma reactor to nucleate and grow silicon nanocrystals with size smaller than 5 nm, although they do not provide a direct comparison between hydrogenated (SiH_4) and chlorinated ($SiCl_4$) precursors. In our study, we have used a radio-frequency (RF) non-thermal plasma reactor to produce silicon nanocrystals starting from either silane or silicon tetrachloride. We have compared the process parameters and the material properties for these two cases, and found that, while it is possible to produce high-quality nanocrystals starting from silicon tetrachloride, the process parameters are radically

different for these two precursors and the material properties are deeply affected by the precursor choice.

This chapter is organized as follows: section 2 describes in detail the equipment used for material synthesis and characterization. Section 3 presents the collected data, which is then discussed in section 4. The last section contains the concluding remarks and acknowledgments.

Experimental details

Silicon particle preparation

Silicon nanocrystals have been produced using either silane (SiH_4) or silicon tetrachloride ($SiCl_4$) as precursors using a non-thermal plasma reactor design based on the one described in [14]. The reactor has been modified to increase the nanomaterial production rate.

The schematic view of experimental setup is shown in Figure A. The system contains plasma reactor, rotary pump, bubbler system, vacuum fittings, power source, and T-type matching network. The plasma reactor consists of a 30 cm long Pyrex tube with an outer diameter equal to 2.54 cm, connected at both ends to Ultra-Torr vacuum fittings and evacuated using a rotary pump. The base pressure for the system is <10

mTorr. The plasma is generated between a ring electrode wrapped around the tube and one of the Ultra-Torr flanges, typically the one on the pump side of the system.

The electrical input power is supplied using a 13.56 MHz power supply. The copper ring electrode is 2.54 cm wide, and kept at a distance of 7 cm from the nearest metal flange. A T-type matching network is used to minimize reflected power. Silane is supplied from a compressed tank at a concentration of 1.37%, balance argon. Silicon tetrachloride is supplied using a bubbler system, which is described in chapter 2 in details, designed to control independently the bubble pressure and the flow rate of the gas carrier flowing through the bubbler. For the samples discussed in this chapter, the bubbler pressure was equal to 100 kPa gage pressure. The bubbler is maintained in a water–ice bath to keep the temperature constant, which is critical to ensure reproducibility. Hydrogen is also added to the gas mixture which is not required when silane is used as a precursor. The reactor pressure is equal to 3.5 Torr for the samples discussed in this chapter. An automatically controlled butterfly valve on the pump side of the system is used to control the pressure. Silicon nanoparticle synthesis using silicon tetrachloride process is presented in Figure 3-1
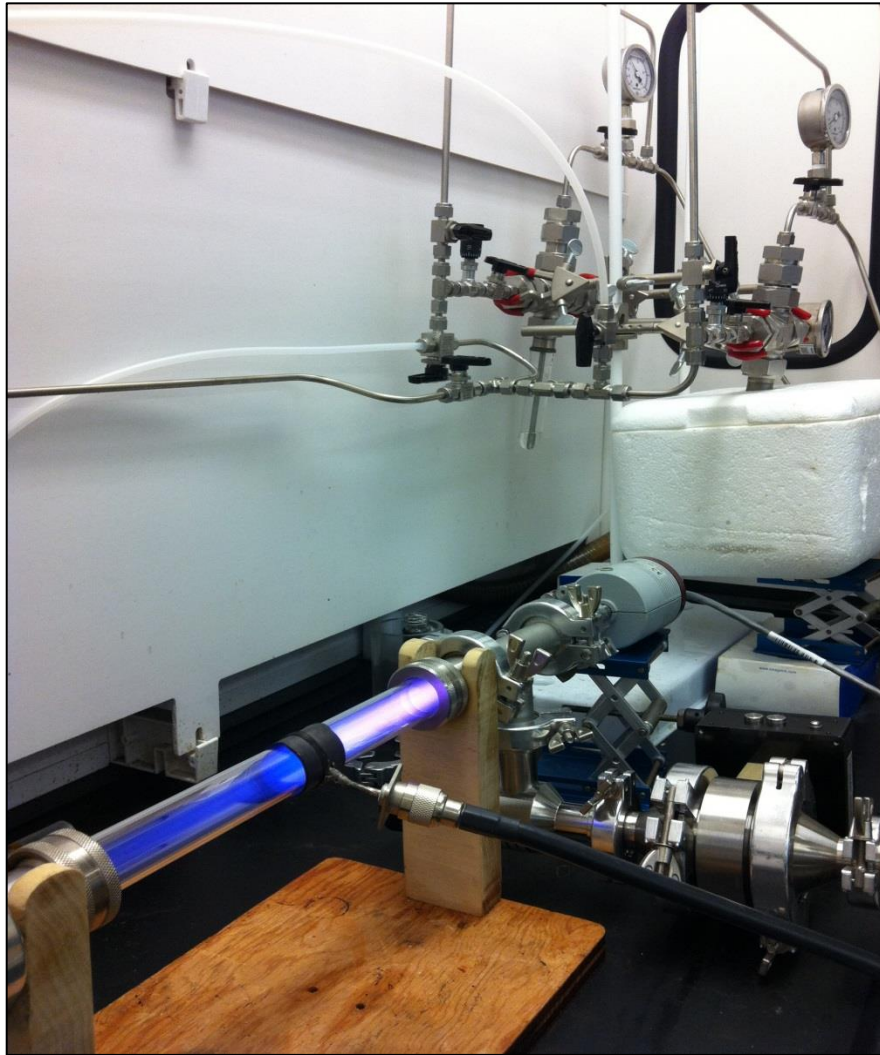
Figure 3-1 Producing silicon nanoparticles using silicon tetrachloride as a silicon precursor.

Material Characterization Technique

In order to characterize the produced silicon nanoparticles, extensive material characterization is performed on the produced powder. TEM is performed on a Tecnai T12 120 kV transmission electron microscope. The TEM samples are prepared by placing lacey carbon grids into the vacuum systems, along the exhaust flow pathway, and nanoparticles are collected as they diffuse onto the grids. Alternatively, a filter

consisting of a fine stainless steel mesh is placed at the reactor outlet to collect several milligrams of powder, necessary for Raman and XRD characterization. Raman spectroscopy was performed on a Dilor XY system using a 532 nm laser source. Powder diffraction was performed on a Bruker D8-Advance diffractometer using Cu Kα radiation (λ = 1.5406 Å). In situ FTIR was performed by splitting the flow at the reactor outlet into two parts. While one part is collected either onto TEM grids or on filters for *ex situ* analysis, the other part is sent through a 1 mm orifice and into an evacuated six-way cross. The particles are accelerated and impacted onto a potassium bromide (KBr) target, which is placed in the optical pathway of an IR beam. FTIR analysis was performed using a Newport-Oriel modular interferometer, equipped with a deuterated triglycine sulfate (DTGS) detector for extended sensitivity between 400 and 5000 cm^{-1}. A more commonly used mercury cadmium telluride (MCT) detector is not sensitive enough below 600 cm^{-1}, where absorption from Si–Cl bonds is expected.

Results

In this session, structural and material characteristics of silicon nanoparticles that are produced using either silicon tetrachloride or silane will be investigated. For the samples discussed in this chapter, we have kept the flow rate of the argon passing through the $SiCl_4$ bubbler constant and equal to 70 standard cubic centimeters per minute (sccm). The reactor pressure during nucleation and growth of the particles is

kept at 3.5 Torr. The bubbler pressure is kept constant and equal to 100 kPa. Hydrogen is added to the system for silicon tetrachloride case. For the silane case, hydrogen addition is not required.

Mass Production

Based on the given conditions, we calculate the $SiCl_4$ flow rate using the following relation:

$$Q_{SiCl_4} = Q_{Ar} \frac{P_{vapor}[SiCl_4]}{P_{bubbler} - P_{vapor}[SiCl_4]} \qquad (2)$$

In the relation, Q_{SiCl4} and Q_{Ar} represent the $SiCl_4$ and argon volumetric flow rates. $P_{vapor}[SiCl4]$ is the precursor vapor pressure at a given temperature, and $P_{bubbler}$ is the pressure of the bubbler that contains the precursor. The precursor vapor pressure is calculated using publicly available data [22]. For the experiments described in this report, we calculate that the $SiCl_4$ flow rate is equal to 3.9 sccm. Based on different experimental analysis, we find that the two parameters controlling the efficiency with which the precursor is converted into nanoparticles are the amount of hydrogen that is added to the reaction and the RF power input. In Figure 3-2 we report the mass production rate of nanomaterial in units of milligrams per hour. These data are obtained by measuring the mass deposited onto a stainless steel filter placed downstream of the

reactor after several minutes of run time. The mass production rate increases with

hydrogen addition and reaches a maximum at a flow rate of 100 sccm, which roughly

corresponds to a molar ratio between H_2 and $SiCl_4$ equal to 25. Under these conditions,

the production rate is equal to approximately 140 mg h^{-1} and 50% of the silicon

delivered by the precursor is converted into nanoparticles. We find that the input power

affects the conversion efficiency, with an optimal input power value of 175 W. Further

increase of the H_2 to $SiCl_4$ ratio does not improve the conversion efficiency, which is

maximized and equal to 50% for our reactor design. When exactly the same reactor is
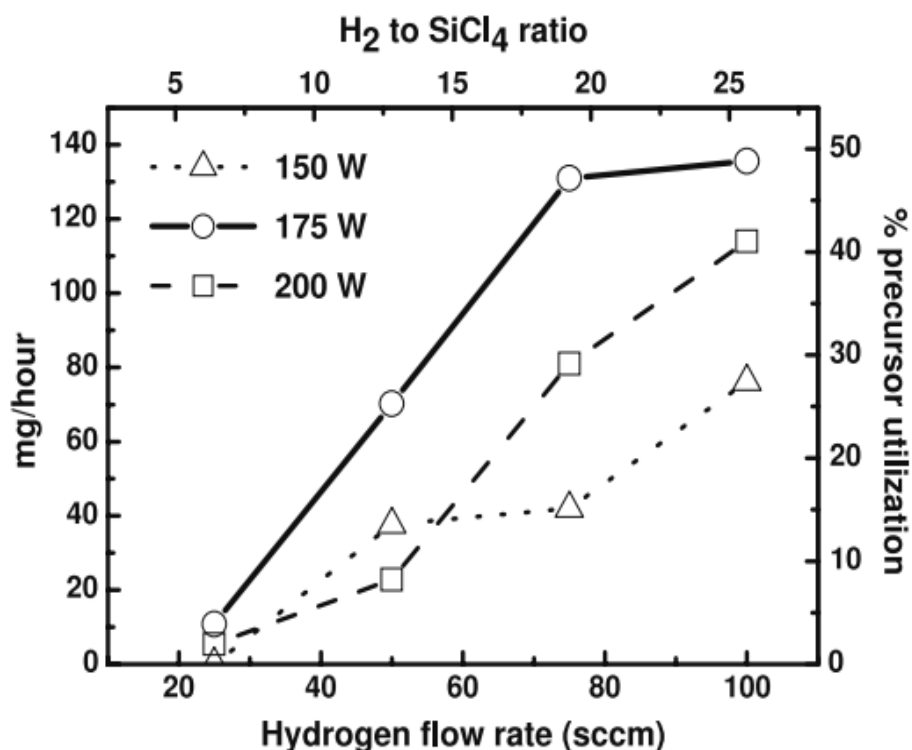
Figure 3-2 Mass production rate of silicon nanocrystals as a function of hydrogen flow rate and power input. The corresponding precursor utilization rate is shown on the left y-axis. The corresponding H2 to SiCl4 atomic ratio is shown on the top x-axis

used with silane as a precursor, we measure a higher precursor utilization rate. We run the process with a flow rate of 170 sccm of 1.37% SiH4 in argon, at the same pressure of 3.5 Torr and with an RF power input of 120 W, and obtain a production rate of 130 mg h^{-1}. The silane flow rate is 2.3 sccm, and the precursor conversion efficiency is 80%. Notice that this value is significantly higher than the 50% utilization rate reported in [14], where a smaller diameter reactor (0.95 cm OD) was used, likely leading to increased material loss to the reactor wall. We keep the total flow rate close to 170 sccm for both the silane and the silicon tetrachloride case so that the residence time in the reactor based on the flow velocity and a reactor length of 7 cm is the same for both cases and equal to 56 ms.

Silicon Nanoparticles Crystallography

Figure 3-3 shows TEM micrographs for silicon nanocrystals produced using either silicon tetrachloride or silane. For the SiCl4 case, the particles are produced using 70 sccm of argon flowing through the bubbler, 100 sccm of H2 and 200 W of power input. For the silane case, the total flow rate is 170 sccm of 1.37% SiH4 in argon and the power is 150 W. The pressure is equal to 3.5 Torr and the residence time is equal to 56 ms for both cases. In Figure 3-3 (a) we show a bright field TEM micrograph of nanoparticles produced using silane. The particle size distribution is fairly narrow with all the particles being between 5 and 10 nm in size. A lower magnification bright field TEM micrograph is
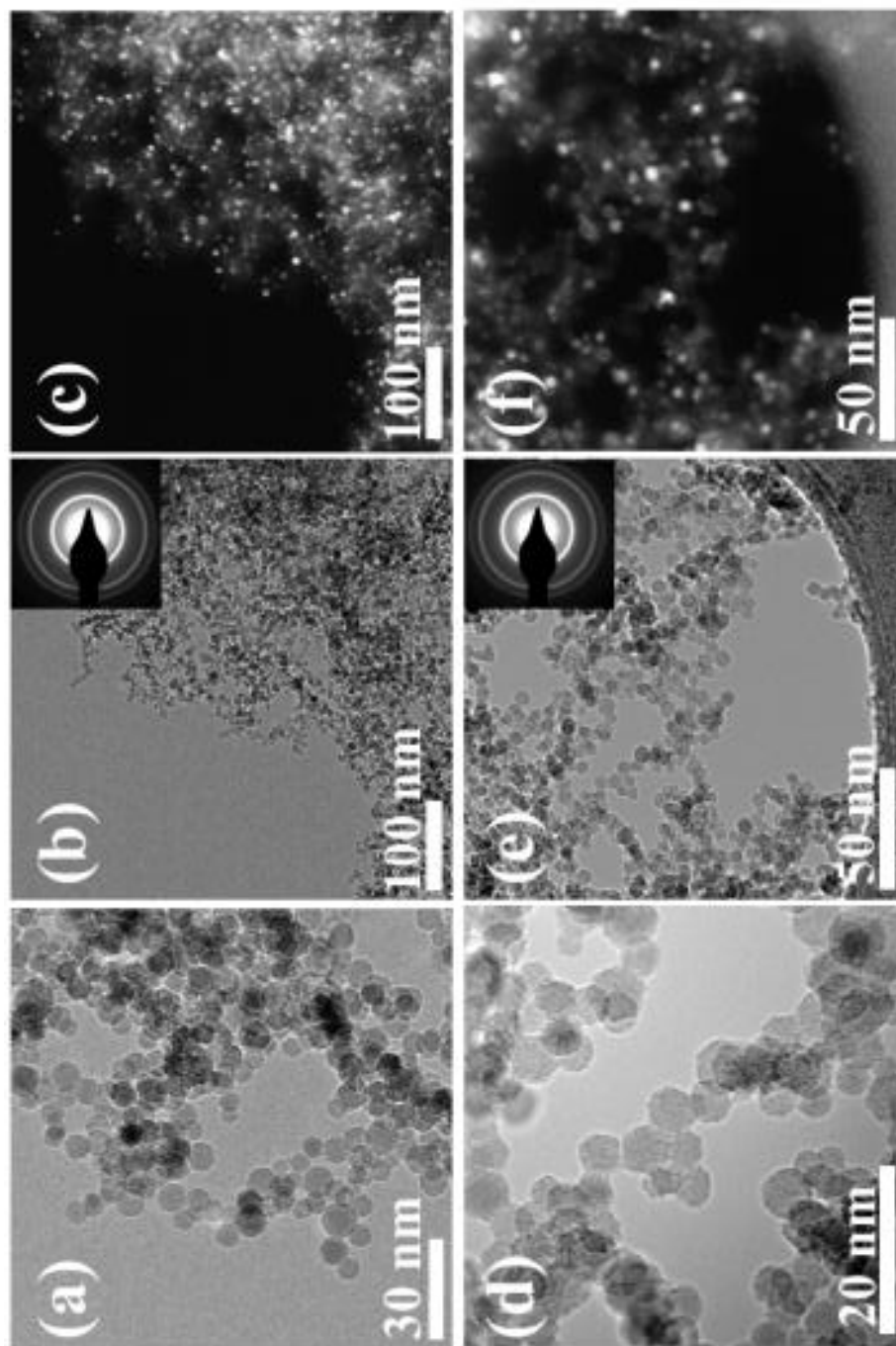
Figure 3-3 TEM micrographs of silicon nanocrystals. (a), (b) Bright field micrographs of nanoparticles produced using silane as precursor. (c) Dark field micrograph corresponding to (b), indicating the presence of nanocrystals. In the inset of (b), the selected area diffraction pattern shows polycrystalline rings. (d), (e) Bright field micrographs of nanoparticles produced using silicon tetrachloride as precursor. (f) Dark field micrograph corresponding to (e). In the inset of (e), the selected area diffraction pattern shows polycrystalline rings.

shown in Figure 3-3 (b) with the corresponding dark field micrograph in Figure 3-3 (c), indicating that the large majority of the nanoparticles have a crystalline structure. This conclusion is also supported by the analysis of several high-magnification images, not shown here, for the powder produced using silane, in which the lattice fringes from the crystallites are easily identifiable. A selected area diffraction pattern is shown in the inset of Figure 3-3 (b). The appearance of polycrystalline ring is expected since several hundred particles participate in the formation of the diffraction pattern. In Figure 3-3 (d) we show a bright field TEM micrographs for nanoparticles produced using silicon tetrachloride. The particle size distribution is very close to the case of the silane-produced material. Additional bright and dark field micrographs are shown in Figure 3-3 (e) and (f) respectively, indicating that the sample has a high degree of crystallinity. As for the case of the silane-produced sample, the majority of the nanoparticles have a crystalline structure. In the inset of Figure 3-3 (e) we show a selected area diffraction pattern for the sample produced using silicon tetrachloride, confirming the presence of crystalline particles in the sample. As for the inset in Figure 3-3 (b), hundreds of particles contribute to the formation of the diffraction pattern.

The conclusion that the degree of crystallinity is high is supported by several high-magnification images, such as the one shown in Figure 3-4. The particles in Figure 3-4 were produced using $SiCl_4$ as precursor, under the same production parameters as for the sample shown in Figure 3-3 (d)–(f). Lattice fringes from the (111) planes confirm that the particles are crystalline. It is important to note that during high-resolution TEM
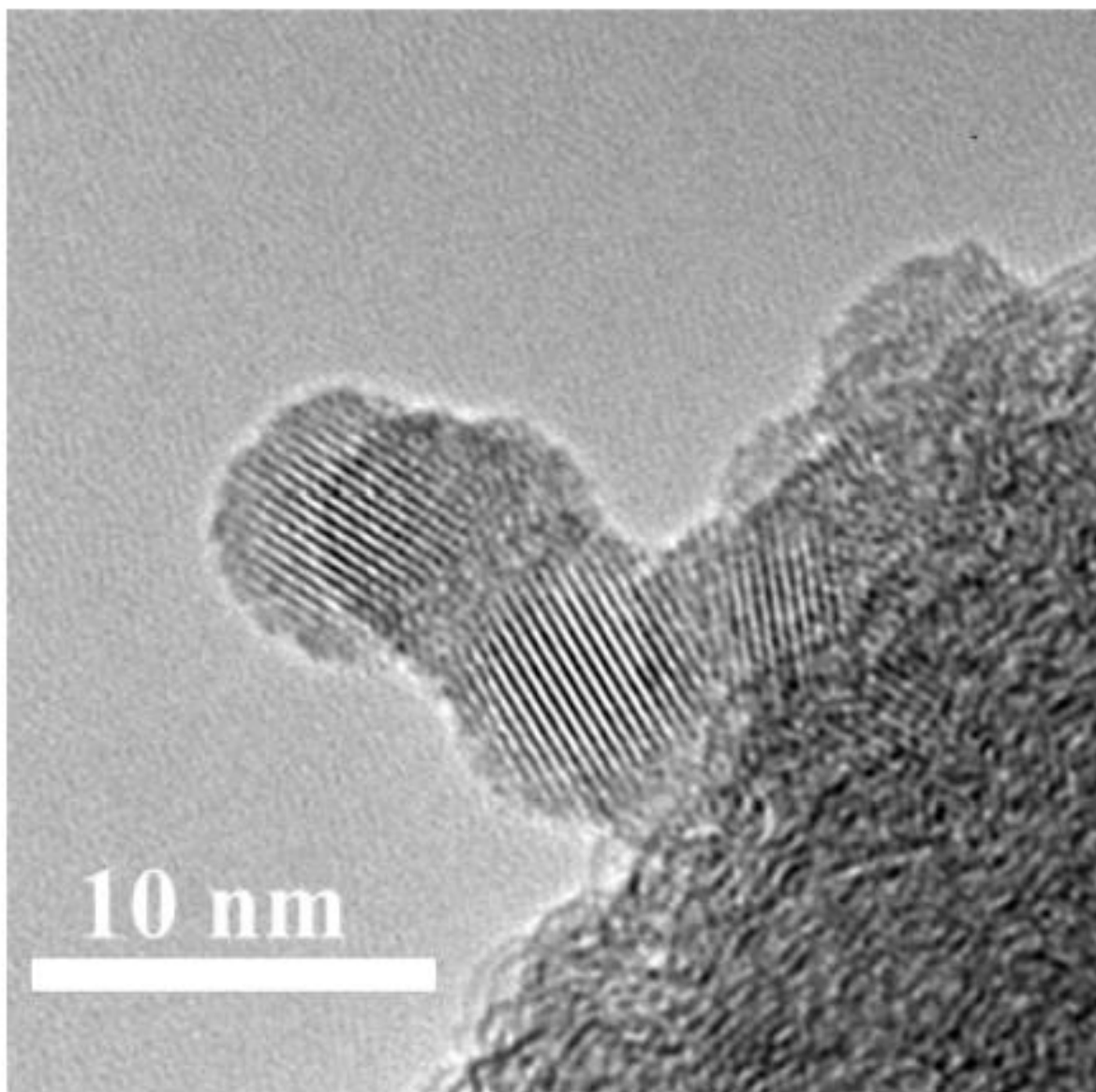
Figure 3-4 High-magnification TEM micrograph of silicon nanocrystals produced using silicon tetrachloride, corresponding to the sample shown in figures 2(d)–(f). Fringes from the (111) lattice planes are clearly distinguishable.

analysis it was straightforward to identify lattice fringes throughout the sample, confirming that the ensemble of particles has a high degree of crystallinity. The TEM analysis shows that high quality, free standing silicon nanocrystals can be produced using $SiCl_4$ as a precursor, and that there seem to be no discernible differences between the particles produced using either $SiCl_4$ or SiH_4 at least with respect of their size distribution and their structure.

Further structural analysis of the particles synthesized using silicon tetrachloride is presented in Figure 3-5 for material produced with 70 sccm of Ar and 100 sccm of H_2, and with input power of 100 and 175 W. Figure 3-5 indicates the Raman spectroscopy of silicon nanoparticles.

Raman analysis shows a single broad peak centered at 485 cm^{-1} for powder produced with an input power of 100 W. For powder produced with an input power of 175 W a clear peak at 517 cm^{-1} is observed with a shoulder at lower wavenumbers. We have performed a two-peak Gaussian fit and found contributions from a peak centered at 485 cm^{-1} with a 77 cm^{-1} width, and from a peak centered at 517 cm^{-1} with an 11 cm^{-1} width. In accordance with the literature on the Raman characterization of amorphous and microcrystalline silicon [23], we attribute the lower wavenumber contribution to the amorphous phase, and the 517 cm^{-1} peak to the crystalline phase. The crystalline phase is detected in Raman spectra as a sharp feature at 520 cm^{-1} in bulk material [23], and a shift in the peak position to wavenumbers as low as 512 cm^{-1} is well known to be
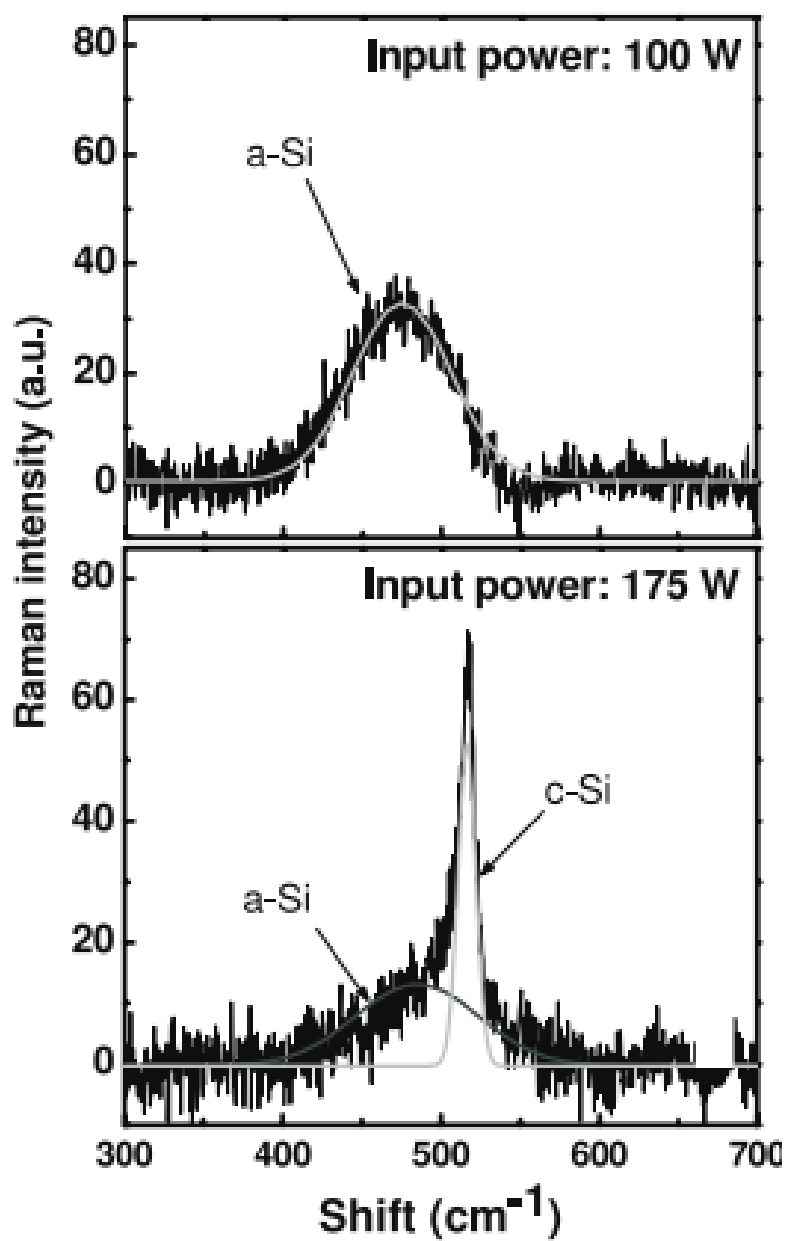
Figure 3-5 Results of Raman spectroscopy for silicon nanoparticles produced using 3.9 sccm SiCl$_4$, 70 sccm Ar, 100 sccm H$_2$, 100 W and 175 W electrical power input

induced by small size effects [23, 24]. Additional studies are necessary to clearly deconvolute the influence of other effects that can induce a shift in the peak position of the signal due to the crystalline phase. For instance, the authors in [24] conclude that the presence of compressive stress shifts the peak position close to 520 cm^{-1} even for small crystals. For the case of free standing nanoparticles, the issue of stress induced by the presence of a native oxide shell and its influence on the Raman characterization has not been addressed yet. Such study goes beyond the scope of this publication. Raman characterization clearly confirms that, when the electrical input power is sufficiently high, crystalline material can be produced when using silicon tetrachloride as precursor. A shoulder centered at 485 cm^{-1} is present even for material produced at a higher power input level, and this behavior is also observed in samples produced using silane as precursor. The authors of [23, 24] observe a similar peak shape for PECVD deposited microcrystalline silicon, and attribute the amorphous-like component to 'surface-like' modes arising from cluster surfaces and from grain boundaries. Similar peak shapes have been reported in [21, 25] for other free standing nanocrystals. The TEM analysis presented in Figure 3-3 confirms that, despite the presence of the 485 cm^{-1} shoulder, the material is crystalline and the ensemble crystalline fraction of the sample is very high. XRD, which is shown in Figure 3-6, further supports this conclusion, since clear peaks from the [111], [220] and [311] crystallographic planes at 28.47°, 47.35° and 56.18° respectively are observed for powder produced using a 175 W power input level. Although barely above the background noise level, peaks from the [400] and [331]
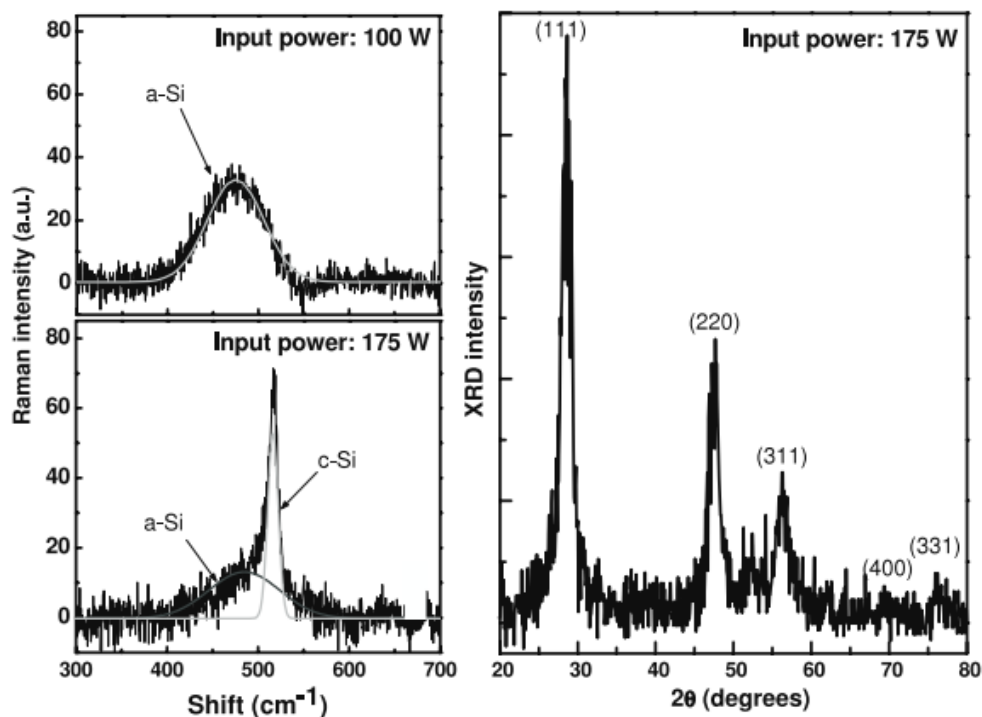
Figure 3-6 XRD results for silicon nanoparticles produced using 3.9 sccm SiCl$_4$, 70 sccm Ar, 100 sccm H$_2$, and 175 W electrical power input

planes at 69.13° and 76.37° are observed. We analyzed the XRD data using the Williamson–Hall method and found an average crystal size of 6 nm, in good agreement with the TEM observation.

The data presented in Figures 3.3–3.6 confirm that crystalline material with a high production rate can be obtained when SiCl$_4$ is used as a precursor. Nevertheless, there are significant differences in the process when SiCl$_4$ is used compared to the silane case. As already shown in Figure 3-2, the addition of significant amounts of hydrogen is necessary to increase the precursor utilization rate for the case of SiCl$_4$. This is opposite to the silane case, where significant addition of hydrogen slows down the nucleation

rate and reduces the mass production rate. Another important difference is with respect

of the influence of input RF power over the structure of the particles for the two

precursor cases. We have fitted the Raman scattering spectrum for several samples

using two Gaussian peaks, allowing the peak position for the amorphous-like

component to vary between 480 and 495 cm^{-1}, and the peak position for the crystalline

component to vary between 512 and 520 cm^{-1} [23]. The peak area for the amorphous

component is referred to as A_a, and the peak area for the crystalline component is

referred to as A_c. It is fairly common to use the area ratio $\frac{A_c}{A_c+A_a}$ as a measure of the

crystalline fraction in the sample. Such an approach is not straightforward, since factors

such as the contribution from 'surface-like' modes (as already discussed) and the

presence of strain can greatly affect the relative strength of the crystalline and

amorphous signals. For a detailed discussion on this topic, see [24]. We use the area

ratio $\frac{A_c}{A_c+A_a}$ to monitor the onset of crystallization in our system, and we plot $\frac{A_c}{A_c+A_a}$

versus electrical power input for the two precursor cases in Figure 3-7. For the case of

powder produced using silane, a significant contribution from the crystalline peak is

already present for an input power of 60 W. The TEM analysis shown in Figure 3-3

suggests that for an input power of 150 W the ensemble crystalline fraction is high. In

comparison, the powder produced using silicon tetrachloride is fully amorphous even

when the power input is 100 W. A clear crystalline contribution is observed for a power

input of 125 W, and TEM analysis suggests that the powder is fully crystalline at a power

input of 175 W. We also report that we have not found a significant influence of the

hydrogen-to-silicon tetrachloride ratio over the particle structure. This conclusion was

reached by performing a Raman and TEM characterization on all the samples discussed

in Figure 3-2.
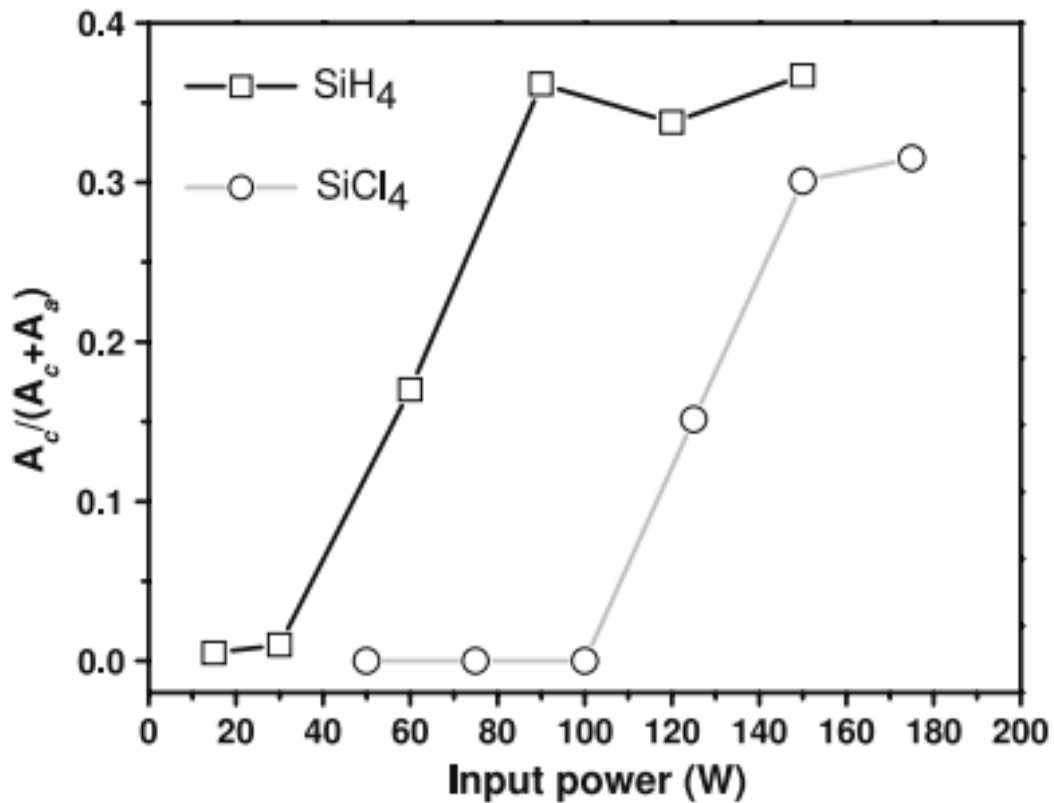
Figure 3-7 Dependence of ratio of Ac =.Ac C Aa / on electrical power input for material produced using either silane or silicon tetrachloride as precursor. Ac and Aa are respectively the area of the peaks corresponding to the crystalline and amorphous signals in the Raman spectra. The ratio is proportional to the fraction of the material with crystalline structure

Silicon Nanoparticles Surface Analysis

The surface of the silicon nanocrystals also differs greatly depending on the precursor choice. This is an extremely important aspect for nanomaterials, whose properties and functionality are strongly influenced by their surface configuration. Figure 3-8 shows the FTIR analysis of silicon powder which are produced using either
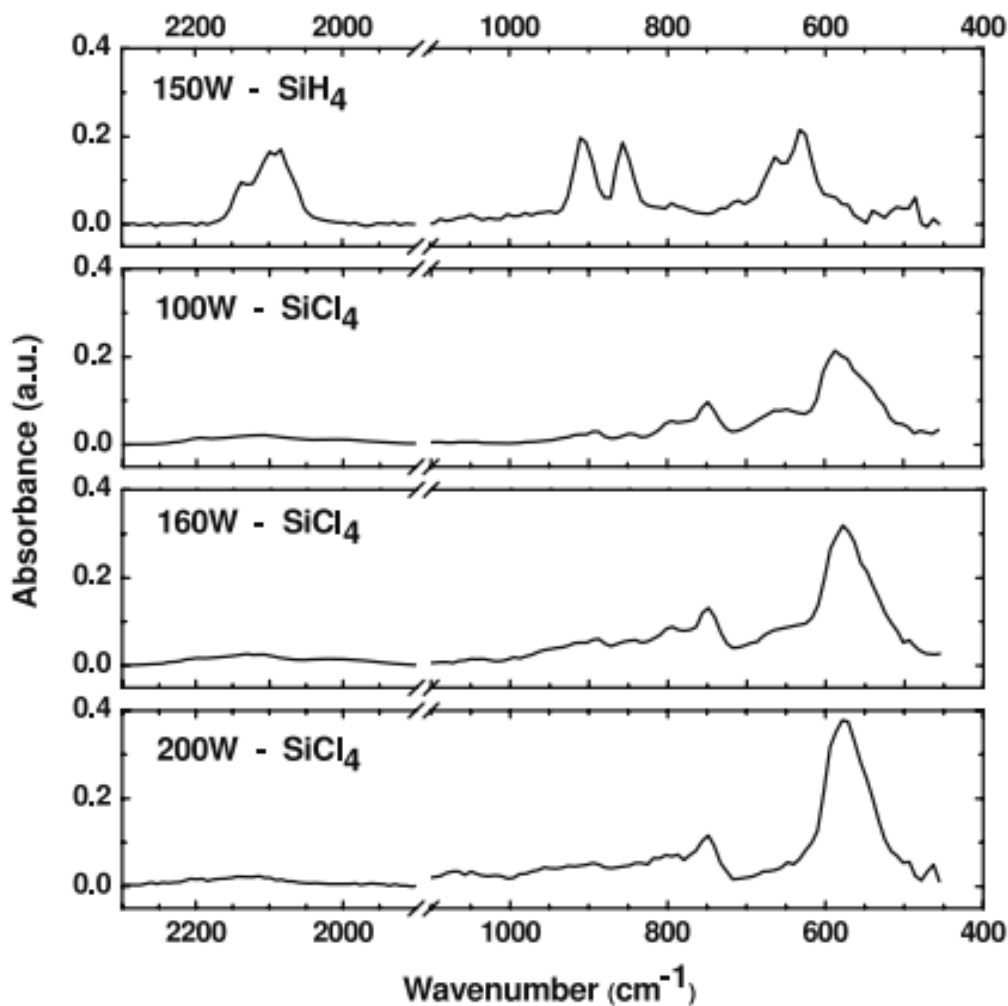
Figure 3-8 FTIR absorption spectra for powder produced either silane (on top) or silicon tetrachloride (three bottom spectra) for different power input levels.

silane or silicon tetrachloride at different applied power.

In Figure 3-8 we show IR absorption spectra for the case of silicon nanocrystals produced using SiH_4 with an input power of 150 W and of silicon nanocrystals produced using $SiCl_4$ with input powers of 100, 160 and 200 W. For the SiH_4 case, the sample was produced using a flow rate of 170 sccm of 1.37% SiH_4 in argon. For the $SiCl_4$ spectra, the flow rate of the argon flowing through the bubbler is 70 sccm, and the hydrogen flow rate is 100 sccm. The samples were collected in situ onto a KBr pellet, as described in the experimental section, and the absorption was measured under vacuum without the samples ever being exposed to air. The weight of the KBr pellet was measured before and after the powder was collected. This allows quantification of the mass of the powder that is responsible for the IR absorption. For the spectra shown in Figure 3-8, the mass was typically between 0.5 and 1.5 mg. The intensity of each spectrum shown in Figure 3-8 has been normalized to the mass of the powder collected on the KBr holder, so that a semi-quantitative comparison between different samples is obtained. The most obvious difference between the sample produced using silane and the samples produced using silicon tetrachloride is the presence of strong absorption from SiHx surface species for the silane sample, while this peak is much weaker for the silicon tetrachloride samples. For the silane sample, clear signals from SiHx (x = 1–3) stretching vibrational modes are detected at ~2100 and at ~620 cm^{-1}, while wag and scissor modes from SiH_2 and SiH_3 are detected at ~850 and ~900 cm^{-1}. For the silicon tetrachloride

70

case, the SiHx feature at ~2100 cm^{-1} is roughly one order of magnitude weaker, while a strong and broad absorption peak centered at 570 cm^{-1} is observed.

A comprehensive discussion of FTIR characterization of chlorinated silicon surfaces can be found in [26]. The authors report that absorption from Si–Cl stretching and wagging modes are expected to appear as sharp peaks at 584 cm^{-1} and 527 cm^{-1} respectively for the case of a flat Si(111) surface. Extended exposure of flat silicon surfaces to chlorine gas gives rise to a broad 560 cm^{-1} feature that is attributed to SiClx moieties with structural and chemical inhomogeneity. The same absorption feature probably contributes to the signal that we observe in our samples, since the highly curved nanocrystal surface is very likely conducive to an inhomogeneous surface configuration. In the same report [26] a broad feature centered at 590 cm^{-1} was observed for an HF treated Si(100) surface which is inherently rougher than the Si(111) case, further justifying our assignment of the broad 570 cm^{-1} peak to SiClx surface groups. Additional absorption peaks for the silicon tetrachloride samples can be observed at 740 and 780 cm^{-1}, which we tentatively attribute to SiClx species as well. All the samples have very little absorption at 1050 cm^{-1}, where the signal from silicon oxide is expected. This is in contrast with what is reported in [21], where in situ FTIR analysis of silicon nanocrystals produced in a plasma reactor using silicon tetrachloride as precursor shows that silicon oxide may be present at the particle surface even before air exposure, likely because of partial etching of the quartz reactor wall. The exact reason for this difference is not clear at this point.

The FTIR data in Figure 3-8 also indicate that chlorine may be trapped in the nanoparticles during nucleation and growth. While bulk Si–H bonds are IR active and detectable at a 2000 cm^{-1}, bulk Si–Cl bonds are predicted to be IR active and detectable at 532 cm^{-1} [27] and have been experimentally reported at 545 cm^{-1} [19]. The broad SiClx peak centered at 570 cm^{-1} extends to 520 cm^{-1}, with the shoulder at lower wavenumbers being more pronounced for the 100 and 160 W samples, which have lower crystalline fraction, compared to the 200 W sample. The contribution from bulk Si–Cl stretching modes cannot be ruled out. In Figure 3-9 we present the same absorption spectra shown in Figure 3-8, but with focus on the absorption peak centered at 2100 cm^{-1}. Notice that the scale is different between the silane case and the three spectra from silicon tetrachloride samples, indicating that the absorption in this region is roughly an order of magnitude stronger for the sample produced using silane. For the silane sample, the 2100 cm^{-1} peak can be deconvoluted into three components corresponding to SiH$_3$ (~2135 cm^{-1}), SiH$_2$ (2110 cm^{-1}) and SiH (2090 and 2070 cm^{-1}) vibrational stretching modes. For the silicon tetrachloride samples, the shape of the absorption peak in this area is significantly different. We notice that the peak maximum is shifted to slightly higher wavenumbers and that a peak can be easily distinguished at 2200 cm^{-1}. We expect this blue-shift to be introduced by the presence of chlorine atoms in the vicinity of silicon hydride bonds, i.e. various SiClxHy surface species. A similar blue-shift was observed in [28] as a flat hydrogen terminated silicon surface was progressively exposed to chlorine gas. A more surprising feature in Figure 3-9 is the
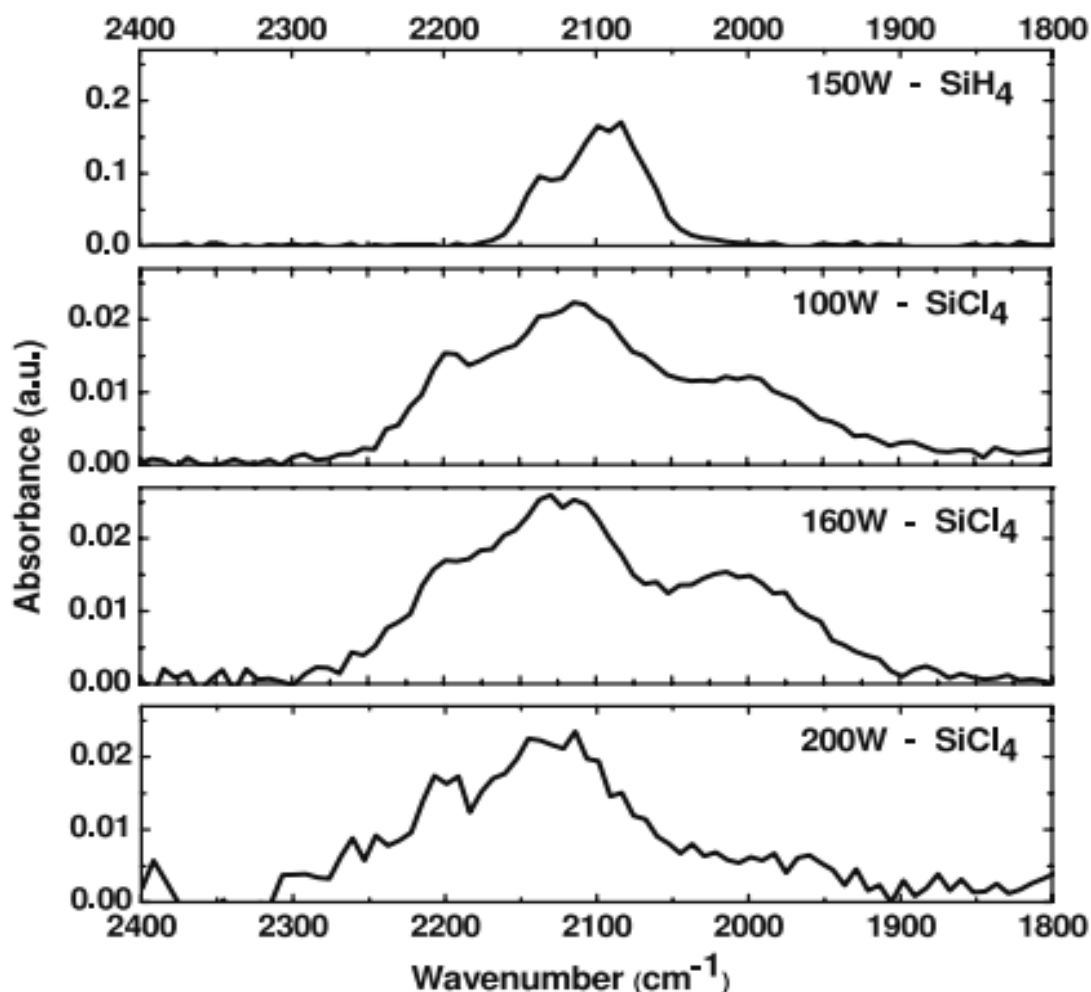
Figure 3-9 Same spectra as for figure 5 with x-range adjusted to better visualize the shape of the peak centered at ~2100 cm^{-1}, due to SiHx stretching modes. The top spectrum, for powder produced using silane, is plotted on a 10x scale to provide a better comparison of the peak shape

presence of a strong and broad peak centered at 2000 cm^{-1}, which is generally observed in amorphous silicon thin films and attributed to bulk SiH vibrational modes. This peak is not present for the spectrum obtained from the silane-produced particles, and it is

relatively weak for the case of particles produced using silicon tetrachloride with a power input of 200 W. It must be mentioned that we have produced silicon nanoparticle from silane under a wide range of conditions, such as very small power to produce amorphous material, or under very high hydrogen dilution, and under no circumstance have we measured absorption at 2000 cm^{-1}.

Several spectra have also been collected to investigate the dependence over hydrogen dilution at a given power input, and we find negligible changes in the absorption spectra, indicating that the surface configuration of silicon nanocrystals produced using silicon tetrachloride cannot be readily controlled by simply modifying the gas composition.

Finally, we analyze the stability of silicon nanocrystals produced using silicon tetrachloride against oxidation in air, which has important consequences on the processability of the material for various practical applications. In Figure 3-10 we present FTIR absorption spectra from silicon nanocrystals produced by flowing 70 sccm of argon through the bubbler, with the addition of 100 sccm of H$_2$ and with a power input of 200 W. After acquiring the first spectrum, the chamber in which the particles are collected is refilled with air for 1 min and re-evacuated, and the second spectrum is collected. The process is then repeated and the sample is exposed to air for nine additional minutes before re-evacuating the chamber and acquiring the new spectrum. A clear increase in absorption between 1000 and 1100 cm^{-1} indicates rapid oxidation,
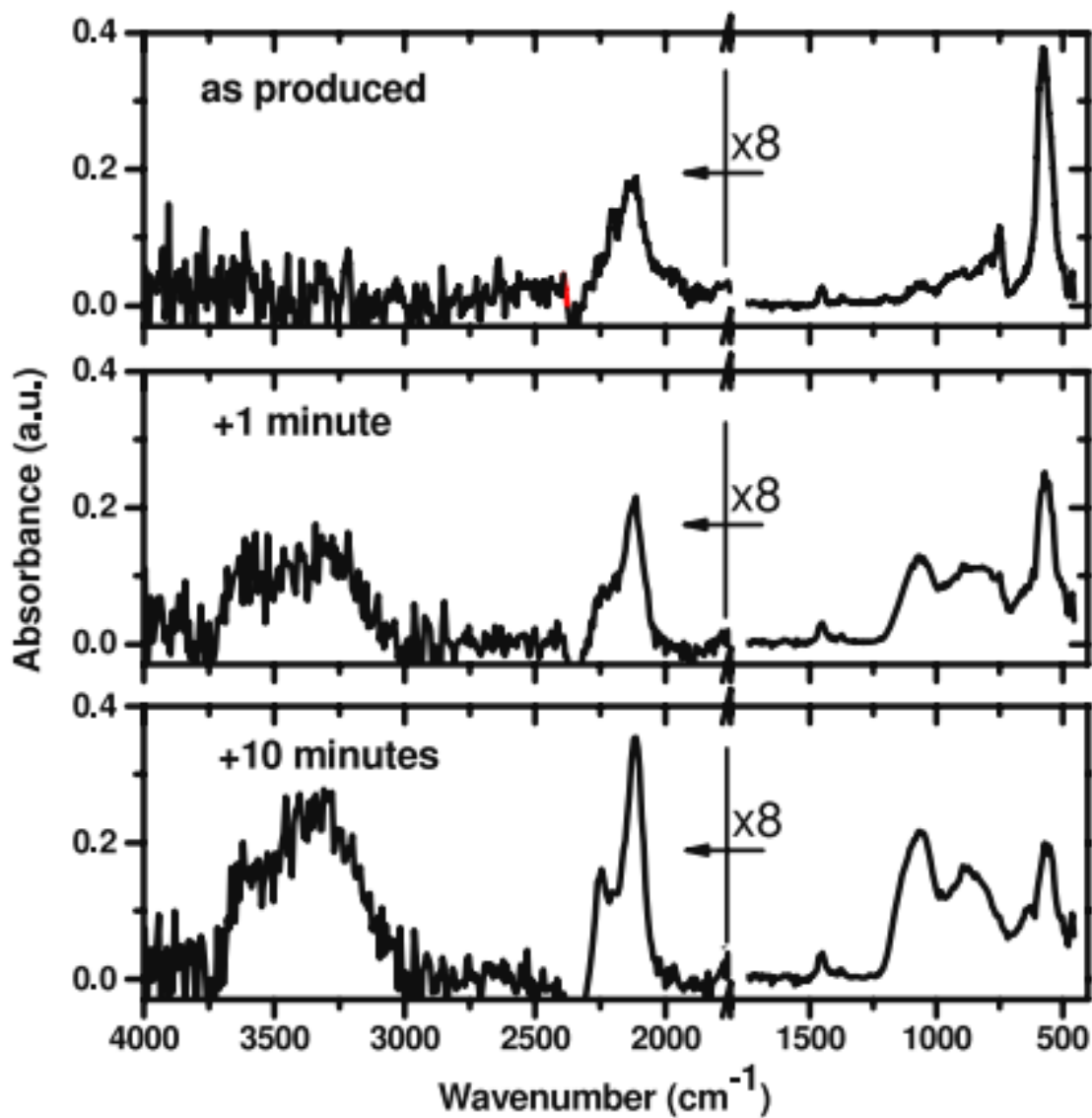
Figure 3-10 Change in FTIR absorption after exposure in air for a sample produced using silicon tetrachloride as precursor

accompanied by a decrease in the absorption signal from the SiClx species at 570 cm^{-1}.

In Figure 3-8 we also notice an increased absorption between 3000 and 3700 cm^{-1}, due to hydroxyl species, and a significant change in the shape of the ~2100 cm^{-1} peak. After a total of 10 min of exposure to air, the peak centered at 2100 cm^{-1}, due to SiHx species,

almost doubles in intensity, an observation also reported in [21]. In addition, the growth of a new peak at 2250 cm^{-1} is observed, which is generally assigned to Si–Hx stretching vibrations in the presence of back bonded oxygen. The same experiment performed on silane-produced particles shows very little change in the absorption spectrum, with the appearance of only a small oxide peak at 1050 cm^{-1} after 10 min exposure to air. The nanoparticles produced using silicon tetrachloride are much more susceptible to oxidation than the nanoparticles produced using silane.

Discussion

The non-thermal plasma process for the synthesis of silicon nanocrystals is deeply influenced by the precursor choice. The central result of our study is that it is possible to produce 5–10 nm silicon nanocrystals with high ensemble crystalline fraction and at a rate of 140 mg h^{-1} using a low-cost chlorinated precursor and using a radio-frequency generated non-thermal plasma. Still, the process is very different compared to the case of silane-produced particles.

First of all, the gas-phase chemistry needs to be modified to enable the nucleation of particles. This is achieved by addition of hydrogen to the system. While the characterization of the gas-phase chemistry occurring in our reactor is beyond the scope of this paper, which focuses on the properties of the produced nanomaterial, we offer a preliminary discussion of the consequences of the precursor choice on the

76

plasma chemistry. In the silane case, nucleation is initiated by electron-impact induced formation of silicon-containing radicals [29]. Our observations indicate that this is not the case when silicon tetrachloride is used. Without any hydrogen addition, no powder is produced and we also observe minimal growth of a film on the inner walls of the reactor. While various radicals are likely to be formed by electron impact, the addition of minimal amounts of an electronegative element such as chlorine to the discharge is well known to deeply affect the plasma chemistry. For instance, a simple visual inspection of the light emission from the reactor indicates that the discharge is much brighter in the case of the silane containing plasma, while it is very dim when silicon tetrachloride is used, indicating that the gas composition leads to a rapid quenching of the plasma. The powder production rate increases rapidly with the addition of hydrogen, as shown in Figure 3-2. We suggest that the addition of hydrogen to the discharge and the subsequent formation of atomic hydrogen by electron-impact dissociation provide additional pathways for the formation of silicon-containing radicals in the discharge. This was already observed in [30], where H_2 addition to a $SiCl_4$–Ar microwave plasma increased the $SiCl_4$ dissociation rate. The proposed dissociation reaction is a radical-molecule process such as the following:

$$SiCl_x + H^{\cdot} \ \rightarrow SiCl_x^{\cdot} + \ HCl$$
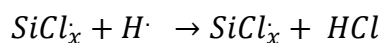
Additional reactions between the chlorosilicon radicals and silicon tetrachloride molecules lead to the formation of heavier radicals and the nucleation of powder. The

fact that there is an optimum input power level for the nucleation production of nanocrystals using a chlorinated precursor deserves further investigation.

What is more relevant for this study is the influence of the precursor choice on the material properties. While the structural analysis performed by TEM, Raman and XRD (Figures 3.3–3.6) indicates that high-quality crystalline material is produced starting from silicon tetrachloride, the data shown in Figure 3-7 indicate that a significantly higher power input is required to produce crystalline material when the chlorinated precursor is used. For the silane case, the presence of crystalline materials is clearly detected with a power input of 60 W. For the silicon tetrachloride case, an input power of 125 W is needed to observe a similar contribution from the 520 cm^{-1} peak in the Raman spectra. Since the residence time is the same for both the silane and the silicon tetrachloride case (56 ms), and since the production rate is very similar (140 mg h^{-1} from silicon tetrachloride and 130 mg h^{-1} from silane), we can conclude that from a practical point of view the process requires twice the power input when silicon tetrachloride is used. This can be interpreted as a consequence of the fact that the plasma is less intense (lower plasma density) because of the presence of an electronegative element. Crystallization of nanoparticles in non-thermal plasmas is a consequence of heat released during recombination of ions at the particle surface [31], and a lower plasma density leads to a decreased energy flux towards the nanoparticles immersed in the discharge. The authors believe that, while this interpretation is reasonable, measurements of the plasma properties and chemistry need to be performed to confirm

78

this. Moreover, additional material-related considerations are consistent with the fact that a higher energy input is needed to produce nanocrystals from chlorinated precursors:

(a) FTIR data shown in Figure 3-8 indicate that the particles produced from silicon tetrachloride are mainly terminated by chlorine. Theoretical calculations by Ma et al [32] show that either the introduction of chlorine into a silicon nanocrystal or coverage of its surface with a high fraction of chlorine can destabilize its structure and introduce significant distortion in the Si–Si bond length.

(b) The FTIR analysis shown in Figure 3-9 indicates that for a power of 100 and 160 W there is significant absorption from bulk SiH, which has never been observed for nanoparticles produced using silane. This is less noticeable for nanocrystals produced from silicon tetrachloride with a power input of 200 W, which has a higher crystalline fraction compared to the 100 and 160 W cases.

(c) The possible contribution from bulk Si–Cl stretching modes to the broad absorption feature centered at 570 cm^{-1} (see figure 5) indicates that chlorine may be included in the core of the particle during growth. Absorption from bulk Si–Cl is expected to be centered at 545 cm^{-1} [19]. As already mentioned, inclusion of chlorine in the silicon network is expected to destabilize its structure [32] and lead to stretching of the Si–Si bonds.

These considerations indicate that amorphous nanoparticles produced using silane have a different structure than amorphous particles produced using silicon tetrachloride, and that the precursor choice has important consequences on the particle structure during growth and crystallization. Our experimental observation and direct comparison between the use of silane and silicon tetrachloride as precursors supports the findings reported in [32]: the presence of chlorine in the system leads to straining and destabilization of the nanocrystal structure. We argue that an increase in the energy flux towards the nanoparticle, achieved by increasing the electrical power input and consequently the intensity of the discharge, is needed to produce samples with a high crystalline fraction.

Another major difference between the silicon nanocrystals nucleated and grown from silicon tetrachloride, compared to those obtained from silane, is the substantially inferior stability against oxidation in air. Silicon nanoparticles produced from silane have a hydrogen terminated surface, and this configuration allows for oxidation to proceed over a time scale of tens of minutes. While the Si–H bonds are stable in air, they do not protect strained Si–Si back-bonds from reaction with oxidizing species [33-35], most importantly water vapor. Our observations confirm that for powder produced using silane there is little to no change in the SiH$_x$ configuration during the first few minutes of exposure to air. The data shown in Figure 3-9 clearly indicate that for the case of powder produced using silicon tetrachloride significant oxidation occurs within the first minute of exposure to air, and that the early oxidation step is accompanied by a rapid

removal of surface SiCl$_x$ moieties. The increase in the absorption from SiH$_x$ moieties at 2100 cm^{-1} during the first few minutes of oxidation, shown in Figure 3-9, is not well understood at this point. Insertion of water molecules into strained Si–Si bonds at the particle surface may lead to an increase in the number of surface Si–H bonds, but an absolute increase in the absorption from Si–H vibrational modes during oxidation has never been observed from particles produced using silane, which have a hydride terminated surface. Further studies are needed to provide a detailed explanation of the initial oxidation mechanism for chlorine terminated silicon particles. Nevertheless, the decreased stability against oxidation has important practical consequences, since even more care in the handling of the material is required to avoid oxidation, which may be detrimental for several opto-electronic applications. The fact that the particle surface is chlorine terminated and not hydrogen terminated may also present an opportunity to develop novel and useful surface modification strategies. While alkylation with alkenes is an easy and common route to modify the surface of hydrogen terminated nanoparticles [36], chlorine terminated silicon surfaces are expected to readily react with other molecules such as Grignard reagents [37, 38].

Conclusions

We confirm that silicon nanocrystals can be produced at a high production rate using silicon tetrachloride as a precursor. We present a direct comparison between the

use of a chlorinated precursor and the use of silane, and discuss the consequences of precursor choice on both the process parameters and the material properties. In particular, we show that the presence of chlorine at the particle surface, and possibly also within the particle core, has important consequences on the crystallization rate, which implies that a higher power is required to produce high-quality material when silicon tetrachloride is the precursor of choice. Particles produced from silicon tetrachloride are very prone to oxidation in air, indicating that even more special care will have to be taken during the processing of this material for any of its potential applications compared to the case of the hydrogen terminated particles.

References

[1]   O. Yasar-Inceoglu, T. Lopez, E. Farshihagro, and L. Mangolini, "Silicon nanocrystal production through non-thermal plasma synthesis: a comparative study between silicon tetrachloride and silane precursors," *Nanotechnology,* vol. 23, Jun 29 2012.

[2]   A. G. Cullis, L. T. Canham, and P. D. J. Calcott, "The structural and luminescence properties of porous silicon," *Journal of Applied Physics,* vol. 82, pp. 909-965, Aug 1 1997.

[3]   T. W. Kim, C. H. Cho, B. H. Kim, and S. J. Park, "Quantum confinement effect in crystalline silicon quantum dots in silicon nitride grown using SiH4 and NH3," *Applied Physics Letters,* vol. 88, Mar 20 2006.

[4]   D. Jurbergs, E. Rogojina, L. Mangolini, and U. Kortshagen, "Silicon nanocrystals with ensemble quantum yields exceeding 60%," *Applied Physics Letters,* vol. 88, Jun 5 2006.

[5]   K. Y. Cheng, R. Anthony, U. R. Kortshagen, and R. J. Holmes, "High-Efficiency Silicon Nanocrystal Light-Emitting Devices," *Nano Letters,* vol. 11, pp. 1952-1956, May 2011.

[6]   C. Y. Liu, Z. C. Holman, and U. R. Kortshagen, "Optimization of Si NC/P3HT Hybrid Solar Cells," *Advanced Functional Materials,* vol. 20, pp. 2157-2164, Jul 9 2010.

[7]   Y. P. Ding, Y. Dong, A. Bapat, J. D. Nowak, C. B. Carter, U. R. Kortshagen*, et al.*, "Single nanoparticle semiconductor devices," *Ieee Transactions on Electron Devices,* vol. 53, pp. 2525-2531, Oct 2006.

[8]   S. Oda, "NeoSilicon materials and silicon nanodevices," *Materials Science and Engineering B-Solid State Materials for Advanced Technology,* vol. 101, pp. 19-23, Aug 15 2003.

[9]   N. Petermann, N. Stein, G. Schierning, R. Theissmann, B. Stoib, M. S. Brandt*, et al.*, "Plasma synthesis of nanostructures for improved thermoelectric properties," *Journal of Physics D-Applied Physics,* vol. 44, May 4 2011.

[10]   J. K. Lee, K. B. Smith, C. M. Hayner, and H. H. Kung, "Silicon nanoparticles-graphene paper composites for Li ion battery anodes," *Chemical Communications,* vol. 46, pp. 2025-2027, 2010.

[11] C. K. Chan, H. L. Peng, G. Liu, K. McIlwrath, X. F. Zhang, R. A. Huggins*, et al.*, "High-performance lithium battery anodes using silicon nanowires," *Nature Nanotechnology,* vol. 3, pp. 31-35, Jan 2008.

[12] A. I. Hochbaum, R. K. Chen, R. D. Delgado, W. J. Liang, E. C. Garnett, M. Najarian*, et al.*, "Enhanced thermoelectric performance of rough silicon nanowires," *Nature,* vol. 451, pp. 163-U5, Jan 10 2008.

[13] J. M. Spurgeon, S. W. Boettcher, M. D. Kelzenberg, B. S. Brunschwig, H. A. Atwater, and N. S. Lewis, "Flexible, Polymer-Supported, Si Wire Array Photoelectrodes," *Advanced Materials,* vol. 22, pp. 3277-+, Aug 10 2010.

[14] L. Mangolini, E. Thimsen, and U. Kortshagen, "High-yield plasma synthesis of luminescent silicon nanocrystals," *Nano Letters,* vol. 5, pp. 655-659, Apr 2005.

[15] X. G. Li, Y. Q. He, S. S. Talukdar, and M. T. Swihart, "Process for preparing macroscopic quantities of brightly photoluminescent silicon nanoparticles with emission spanning the visible spectrum," *Langmuir,* vol. 19, pp. 8490-8496, Sep 30 2003.

[16] M. L. Ostraat, J. W. De Blauwe, M. L. Green, L. D. Bell, H. A. Atwater, and R. C. Flagan, "Ultraclean two-stage aerosol reactor for production of oxide-passivated silicon nanoparticles for novel memory devices," *Journal of the Electrochemical Society,* vol. 148, pp. G265-G270, May 2001.

[17] D. Neiner, H. W. Chiu, and S. M. Kauzlarich, "Low-temperature solution route to macroscopic amounts of hydrogen terminated silicon nanoparticles," *Journal of the American Chemical Society,* vol. 128, pp. 11016-11017, Aug 30 2006.

[18] C. M. Hessel, E. J. Henderson, and J. G. C. Veinot, "Hydrogen silsesquioxane: A molecular precursor for nanocrystalline Si-SiO2 composites and freestanding hydride-surface-terminated silicon nanoparticles," *Chemistry of Materials,* vol. 18, pp. 6139-6146, Dec 26 2006.

[19] J. Chevallier, S. Kalem, S. Aldallal, and J. Bourneix, "Optical and Electrical-Properties of Chlorinated and Hydrogenated Amorphous-Silicon Prepared by Glow-Discharge," *Journal of Non-Crystalline Solids,* vol. 51, pp. 277-290, 1982.

[20] R. Gresback, Z. Holman, and U. Kortshagen, "Nonthermal plasma synthesis of size-controlled, monodisperse, freestanding germanium nanocrystals," *Applied Physics Letters,* vol. 91, Aug 27 2007.

[21]   R. Gresback, T. Nozaki, and K. Okazaki, "Synthesis and oxidation of luminescent silicon nanocrystals from silicon tetrachloride by very high frequency nonthermal plasma," *Nanotechnology,* vol. 22, Jul 29 2011.

[22]   C. L. Yaws, *Handbook of vapor pressure*. Houston: Gulf Pub. Co., 1994.

[23]   Z. Iqbal and S. Veprek, "Raman-Scattering from Hydrogenated Microcrystalline and Amorphous-Silicon," *Journal of Physics C-Solid State Physics,* vol. 15, pp. 377-392, 1982.

[24]   C. Ossadnik, S. Veprek, and I. Gregora, "Applicability of Raman scattering for the characterization of nanocrystalline silicon," *Thin Solid Films,* vol. 337, pp. 148-151, Jan 11 1999.

[25]   R. Anthony and U. Kortshagen, "Photoluminescence quantum yields of amorphous and crystalline silicon nanoparticles," *Physical Review B,* vol. 80, Sep 2009.

[26]   S. Rivillon, F. Amy, Y. J. Chabal, and M. M. Frank, "Gas phase chlorination of hydrogen-passivated silicon surfaces," *Applied Physics Letters,* vol. 85, pp. 2583-2585, Sep 27 2004.

[27]   W. B. Pollard, "Vibrational Resonance Modes in Amorphous-Silicon Alloys," *Physical Review B,* vol. 29, pp. 857-865, 1984.

[28]   G. A. Ferguson, S. Rivillon, Y. Chabal, and K. Raghavachari, "The Structure and Vibrational Spectrum of the Si(111)-H/Cl Surface," *Journal of Physical Chemistry C,* vol. 113, pp. 21713-21720, Dec 31 2009.

[29]   U. V. Bhandarkar, M. T. Swihart, S. L. Girshick, and U. R. Kortshagen, "Modelling of silicon hydride clustering in a low-pressure silane plasma," *Journal of Physics D-Applied Physics,* vol. 33, pp. 2731-2746, Nov 7 2000.

[30]   N. Mayo, U. Carmi, I. Rosenthal, R. Avni, R. Manory, and A. Grill, "Mechanism and Kinetics of Tetrachlorosilane Reactions in an Argon-Hydrogen Microwave Plasma," *Journal of Applied Physics,* vol. 55, pp. 4404-4412, 1984.

[31]   L. Mangolini and U. Kortshagen, "Selective nanoparticle heating: Another form of nonequilibrium in dusty plasmas," *Physical Review E,* vol. 79, Feb 2009.

[32]   Y. S. Ma, X. B. Chen, X. D. Pi, and D. R. Yang, "Theoretical Study of Chlorine for Silicon Nanocrystals," *Journal of Physical Chemistry C,* vol. 115, pp. 12822-12825, Jul 7 2011.

[33]   Y. H. Ogata, F. Kato, T. Tsuboi, and T. Sakka, "Changes in the environment of hydrogen in porous silicon with thermal annealing," *Journal of the Electrochemical Society,* vol. 145, pp. 2439-2444, Jul 1998.

[34]   D. Mariotti, V. Svrcek, J. W. J. Hamilton, M. Schmidt, and M. Kondo, "Silicon Nanocrystals in Liquid Media: Optical Properties and Surface Stabilization by Microplasma-Induced Non-Equilibrium Liquid Chemistry," *Advanced Functional Materials,* vol. 22, pp. 954-964, Mar 7 2012.

[35]   V. Svrcek, D. Mariotti, T. Nagai, Y. Shibata, I. Turkevych, and M. Kondo, "Photovoltaic Applications of Silicon Nanocrystal Based Nanostructures Induced by Nanosecond Laser Fragmentation in Liquid Media," *Journal of Physical Chemistry C,* vol. 115, pp. 5084-5093, Mar 31 2011.

[36]   L. Mangolini, D. Jurbergs, E. Rogojina, and U. Kortshagen, "Plasma synthesis and liquid-phase surface passivation of brightly luminescent Si nanocrystals," *Journal of Luminescence,* vol. 121, pp. 327-334, Dec 2006.

[37]   E. Johansson, P. T. Hurley, B. S. Brunschwig, and N. S. Lewis, "Infrared Vibrational Spectroscopy of Isotopically Labeled Ethyl-Terminated Si(111) Surfaces Prepared Using a Two-Step Chlorination/Alkylation Procedure," *Journal of Physical Chemistry C,* vol. 113, pp. 15239-15245, Aug 27 2009.

[38]   J. M. Buriak, "Organometallic chemistry on silicon and germanium surfaces," *Chemical Reviews,* vol. 102, pp. 1271-1308, May 2002.

Chapter 4 Characterization of Si–Ge Alloy Nanocrystals Produced in a Non-thermal Plasma Reactor

Overview

In this paper we demonstrate the synthesis of high quality crystalline silicon–germanium alloy nanoparticles using the combination of a non-thermal plasma reactor and chlorinated precursors. The produced particles have potential applications in several fields including for the production of advanced thermoelectric materials. The use of silicon and germanium tetrachloride has clear advantages with respect of hydrogenated precursors (silane and germane) from both the cost and safety points of view. Nanocrystals smaller than 10 nm have been produced with excellent control over the alloy composition. Characterization by Raman, XRD and TEM confirm that the produced material is not composed of a mixture of silicon and germanium nanoparticles, but rather by an ensemble of crystals in which each particle is composed of an alloy of silicon and germanium

Introduction

Group IV nanocrystals are attracting increasing interest because of their desirable properties and their many potential applications. These include, but are not limited to, the development of novel electronic devices, of photovoltaic cells that are manufacturable using low-cost, roll-to-roll techniques, and the development of

improved thermoelectric devices for direct heat-to-electrical energy conversion. Silicon and germanium nanocrystals are environmentally safe, and silicon is the second most abundant element on the planet. Germanium is rarer and considerably more expensive than silicon, and its use is not considered to be compatible with large scale applications. Still silicon–germanium alloys have been used for several years in specialized applications. They have been used in the Radioisotope Thermoelectric Generators powering NASA space-crafts since 1976 [1]. The addition of germanium to the silicon lattice reduces the material thermal conductivity and increases the value of thermoelectric figure of merit, ZT. Another approach for improving the efficiency of thermoelectric devices is the reduction of grain size [2], since phonon scattering at the grain boundaries of bulk nanostructured materials reduces the material thermal conductivity.

Bulk nanostructured materials are usually produced by high temperature and pressure sintering of nanopowders [3]. Nanostructuring for the case of silicon–germanium based devices is expected to allow reducing the amount of germanium in the alloy [4], paving the way for their large scale commercial utilization. This motivates our interest in the synthesis of very small (< 10 nm) silicon–germanium nanocrystals. Silicon–germanium alloy particles have been produced using a variety of techniques, including thermal evaporation [5] and laser-induced pyrolysis [6]. The non-thermal plasma synthesis approach has also been shown to be particularly promising for the

synthesis of group IV nanocrystals. Silicon nanocrystals smaller than 5 nm can be produced at a high rate and with a narrow size distribution using continuous flow plasma reactors and silane (SiH_4) as precursor [7]. The synthesis of germanium nanocrystals in a non-thermal plasma reactor starting from germanium tetrachloride ($GeCl_4$) as precursor was demonstrated in [8]. Alloy silicon–germanium nanocrystals have been produced in a non-thermal plasma reactor starting from a mixture of silane (SiH_4) and germane (GeH_4) [9]. The use of these chemicals is problematic because these precursors are stored as pyrophoric compressed gasses. Germane in particular poses a serious health hazard and it would be desirable to avoid its use. In this paper we demonstrate the synthesis of alloy nanocrystals starting from silicon and germanium tetrachloride as precursors. The first clear advantage with respect of silane and germane is the fact that a simple bubbler system can be used to safely deliver the precursors. Moreover, these precursors are significantly cheaper than their hydrogenated counterpart, which makes their use attractive for applications that aim at large scale production.

Experimental Details

We have already shown that high quality silicon nanocrystals smaller than 10 nm can be produced using silicon tetrachloride as precursor [10]. In our previous study we used a 1 in. quartz tube reactor operating at a pressure of 3.5 Torr, with a radio-

frequency (RF) excitation at 13.56 MHz to sustain a non-thermal plasma. We found that heavy dilution with hydrogen is necessary to nucleate powder in the gas phase, most likely because of the formation of atomic hydrogen which extracts chlorine from the precursor and leads to the formation of silicon-containing radicals. We have modified the system by adding a precursor delivery system for germanium tetrachloride. The overall system is then comprised of two bubblers with independent control over their pressures and over the flow rates of each carrier gas. Hydrogen is separately added to the reactor inlet line. Silicon tetrachloride and germanium tetrachloride are purchased from Sigma Aldrich. After extensive investigation of the influence of process parameters on the material properties, we decide to discuss a dataset in which the flow rates of the argon carrier gasses flowing through the silicon and germanium tetrachloride bubblers are constant and equal to 70 and 14 sccm respectively. Hydrogen is added to the reactor at a rate of 100 sccm. This value of hydrogen flow rate is based on our previous study [10] which suggested that sufficient hydrogen dilution is needed to achieve an optimum production rate. This is consistent with a nanoparticle nucleation pathway that is initiated by the hydrogen-induced abstraction of chlorine from the precursor molecules, as discussed in [10]. The pressure is kept at 3.5 Torr, and the RF power input is equal to 175 W. The silicon tetrachloride bubbler is kept in an ice bath while the germanium tetrachloride bubbler is operated at room temperature. The silicon tetrachloride bubbler pressure is kept at 100 kPa (gauge pressure), so that the corresponding silicon tetrachloride flow rate is constant and equal to 3.9 sccm. The germanium tetrachloride

bubbler pressure is varied to control the ratio of silicon to germanium in the reactor. Pressures equal to −50, 0, 50 and 100 kPa (gauge pressure) were used for the germanium tetrachloride bubbler. The corresponding germanium tetrachloride flow rates are 3.34, 1.49, 0.96 and 0.71 sccm.

The residence time in the reactor, based on the flow velocity, is 56 ms. After nucleation in the gas-phase, the powder is collected onto a stainless steel filter which is carefully cleaned by sonication to avoid any contamination. The powder is then sonicated in chloroform. XRD, Raman, SEM and TEM were performed to assess size, structure and composition of the particles. XRD samples were prepared by drop-casting the particle dispersion in chloroform onto a zero-background substrate. Raman samples were prepared by drop-casting the same dispersion onto silicon wafers coated with a 200 nm thick c

opper film. SEM was performed by drop-casting onto copper foil, and TEM was performed by drop-casting the onto holey-carbon grids. XRD was performed on a Bruker D8-Advance instrument using the CuKα line at a wavelength of 1.5406 Å. Raman was performed on a Horiba LabRam HR instrument equipped with a 532 nm laser. SEM analysis, complete with EDS, was performed using a XL30 FEG. TEM analysys was performed on both a Tecnai T12 with 120 kV accelerating voltage and a FEI with 300 kV accelerating voltage. This last instrument has elemental analysis capabilities (EDS).

Results and Discussion

We used XRD as a first screening technique to verify that alloyed silicon–germanium nanocrystals are produced. In Figure 4-1 we show the XRD scans for a pure silicon sample, a pure germanium sample and a silicon–germanium sample produced with a germanium bubbler pressure of–50 kPa (gauge pressure). For the pure silicon sample we observe three distinct peaks at 28.471°, 47.351°, and 56.181°, corresponding to the [111], [220] and [311], crystallographic planes of diamond silicon. For Ge, the same planes generate peaks at 27.301°, 45.341°, and 53.731°. For the sample produced
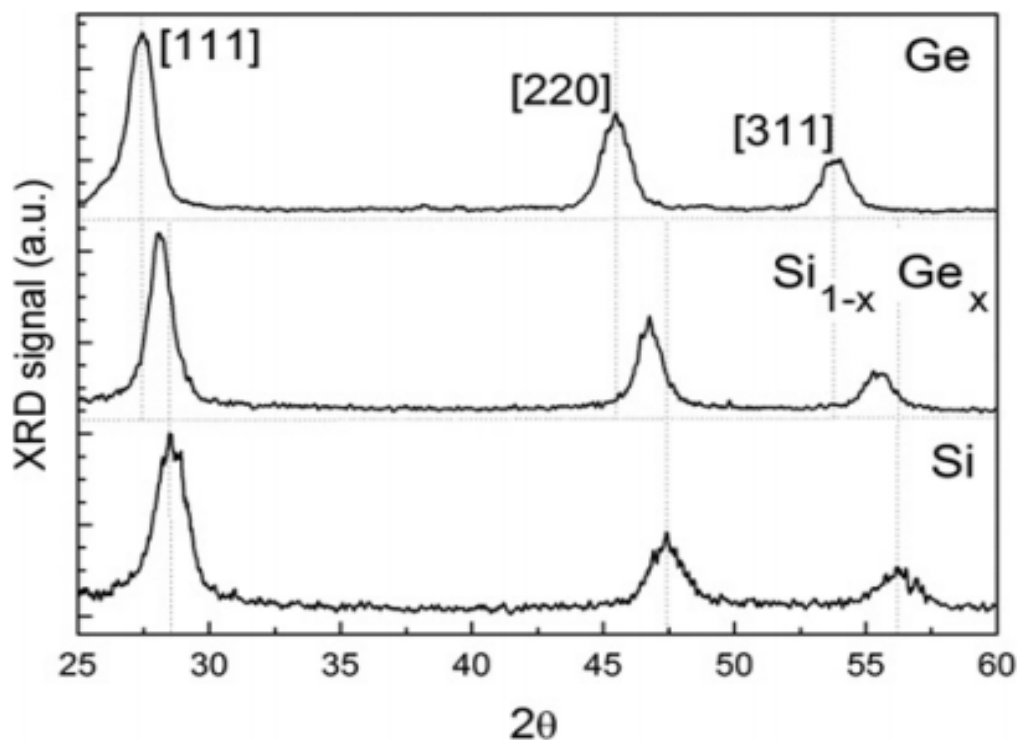
Figure 4-1 XRD of pure germanium, pure silicon and silicon–germanium nanocrystals. As expected, the silicon–germanium sample has peak position intermediate between the pure silicon and the pure germanium cases.

with both the silicon and the germanium precursors supplied to the reactor, the peak positions are intermediate between those of the pure Si and pure Ge cases, as shown in Figure 4-1. For the [111] plane we measure a peak position of 28.131°. This result alone does not prove that alloyed nanocrystals are produced, since a similar pattern can be produced by a mixture of silicon and germanium nanocrystals, although we notice that the full width–half maximum of the [111] peaks is very similar for the three cases (~2.3°). This is a promising indication that the crystal size is similar for the three cases and that the silicon–germanium sample is composed of an alloyed material, since a mixture of silicon and germanium nanocrystals would result in a much broader XRD peak. Under the assumption that the particles are actually composed of a silicon–germanium alloy, we proceed to calculate the lattice constant. We find a value of 5.494 Å (the lattice constant is 5.431 Å for silicon and 5.657 Å for germanium), which corresponds to a geranium atomic fraction of 31.5% (weight fraction equal to 54%).

We have used Raman to obtain critical evidence that the nanoparticles are indeed composed of an alloyed mixture of silicon and germanium. Bulk Si, SiGe alloy, and Ge Raman peaks are known to appear at 520, 410, and 300 cm^{-1}, respectively. In Figure 4-2 we show the Raman spectra for a sample produced at a germanium bubble pressure of–50 kPa (gauge pressure). Three distinct peaks are observed at 275, 400, and 500 cm^{-1}, which correspond to the Si–Si, Si–Ge, and Ge–Ge bonds, respectively. We performed careful measurements at different laser powers to completely avoid any shift
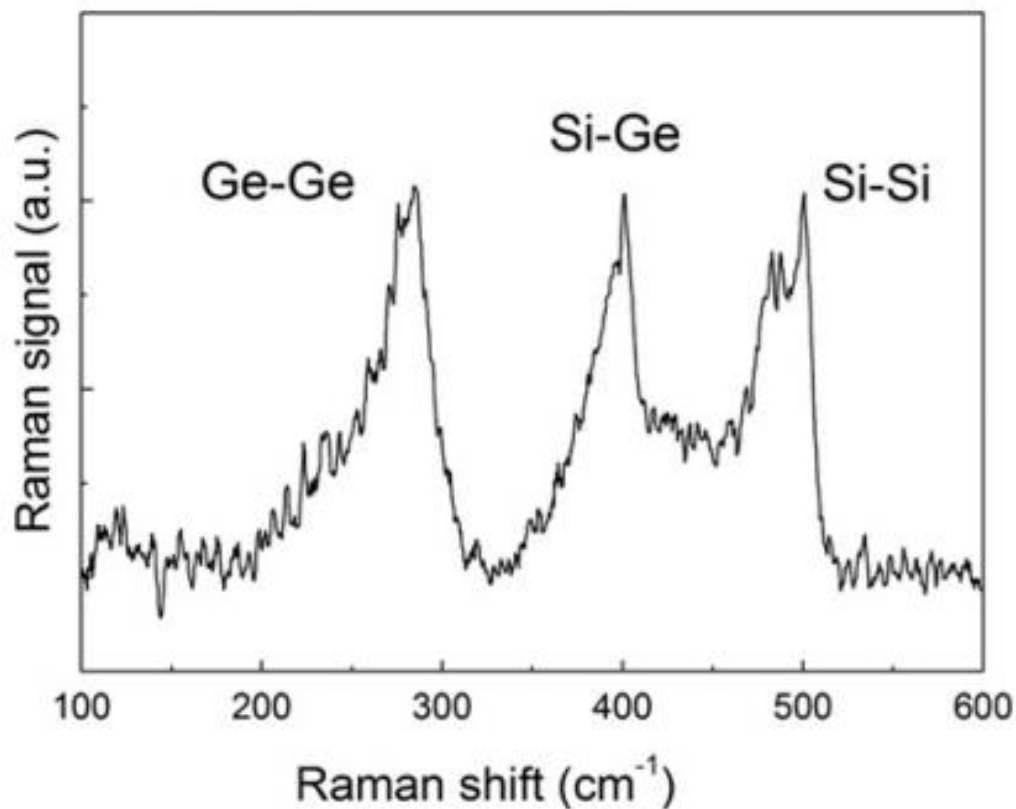
Figure 4-2 Raman spectra of a silicon–germanium sample. Beside the ~ 500 cm^{-1} (Si–Si) and the ~290 cm^{-1} (Ge–Ge) peaks, a clear peak at 400 cm^{-1} (Si–Ge) is present.

in the peak position due to sample heating. The shifts in the peak positions that we observe can be partially explained by the confinement of phonons into small volumes [5, 11]. In addition, the presence of Ge into the lattice induces a shift in the Si–Si Raman frequency. Alonso and Winner found that the shift in the Si–Si peak position correlates with the atomic fraction of germanium (x) according to the relation 520–70x [12]. Using this relation we find a germanium atomic fraction of~30%, in agreement with the XRD

94

measurement. The Raman data clearly shows that the particles are in the form of Si–Ge alloy instead of a mixture of pure Si and Ge nanoparticles.

TEM analysis further supports this conclusion. In Figure 4-3 (a) we show a high-magnification micrograph showing that the particle size is between 5 and 10 nm. Lattice fringes are clearly visible, confirming that the particles have crystalline structure. The selected area diffraction pattern (see inset), taken at lower magnification and formed using several hundreds of nanocrystals, confirms this conclusion. Figure 4-3(b) shows a digital micrograph acquired on a FEI 300 kV instrument with EDS capabilities. EDS was performed first using a larger spot size, which covers tens of nanocrystals. The result of this measurement is shown in Figure 4-3(c). EDS was then repeated using a small probe size, so that only one nanocrystal is sampled. The result of this measurement is shown in Figure 4-3(d). Despite the obvious difference in signal strength, the shape of the EDS spectra is very similar. This is additional evidence that each nanoparticle has a composition equal to the average sample composition, and that each nanoparticle is composed of both silicon and germanium.

Finally, in Figure 4-4 we show the dependence of the sample composition over the precursors flow rates into the non-thermal plasma reactor. The composition is determined by SEM–EDS. The dependence is roughly linear. Raman analysis on each of these samples confirms the formation of Si–Ge alloys. For the sample produced at a germanium bubbler pressure of−50 kPa (gauge pressure), which has the highest
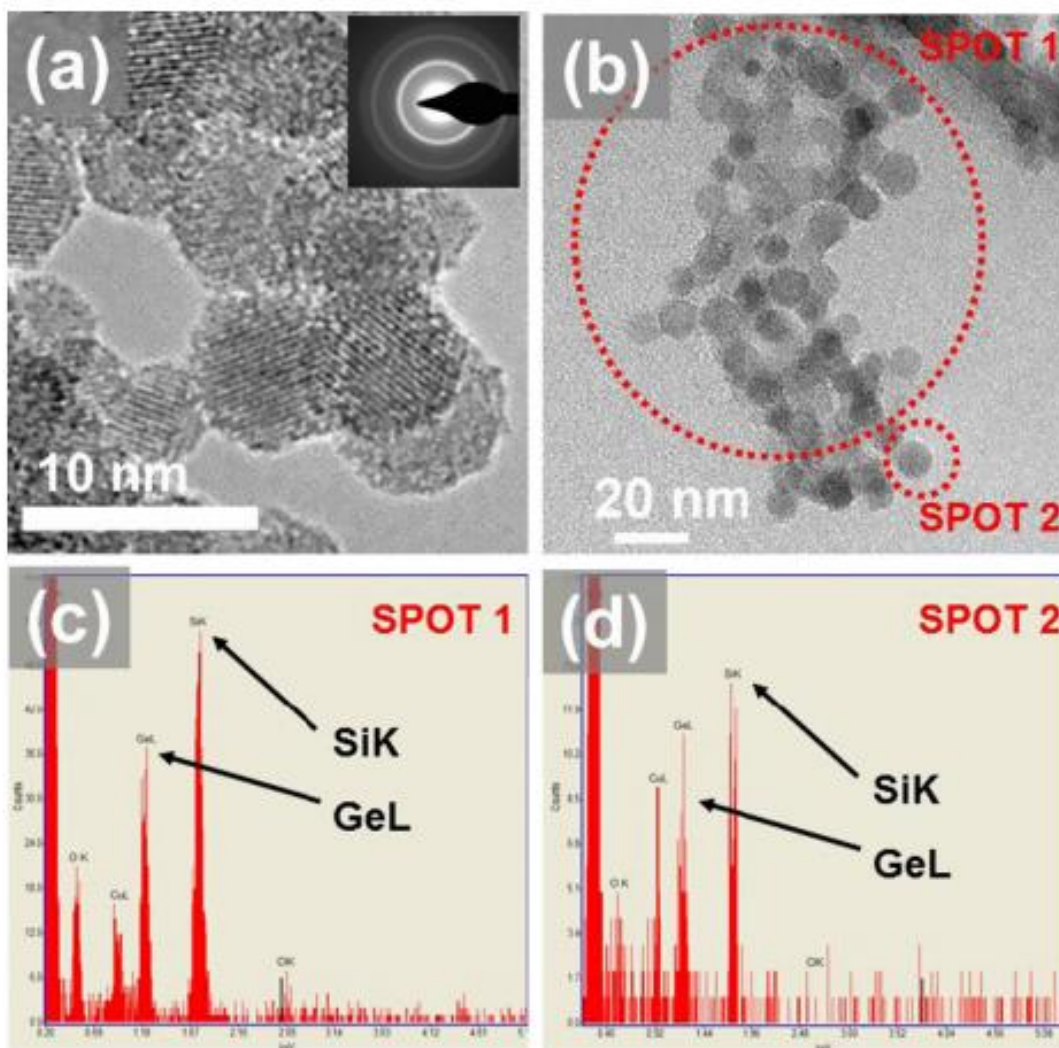
Figure 4-3 (a) High magnification micrograph of SiGe nanocrystals. Particle size is uniformly below 10 nm, and [111] lattice fringes are clearly visible. Inset: selected area diffraction pattern generated from hundreds of particles, resulting in well-defined polycrystalline rings. This image was acquired on a Tecnai T12. (b) Micrographs of SiGe nanocrystals with clear label of the spot sizes that are used for elemental analysis. This measurement was performed on a FEI 300. (c) and (d) are the EDS spectra corresponding to the larger spot and the smaller spot indicated in Fig. 3b

germanium tetrachloride flow rate, we measure a germanium atomic fraction of 29%, in reasonable agreement with the XRD and Raman measurements. The system is controllable and can reproducibly produce $Si_{1-x} Ge_x$ samples with $0 < x < 0.3$. We have limited the germanium atomic fraction to this range since this is the range of interest for thermoelectric applications.
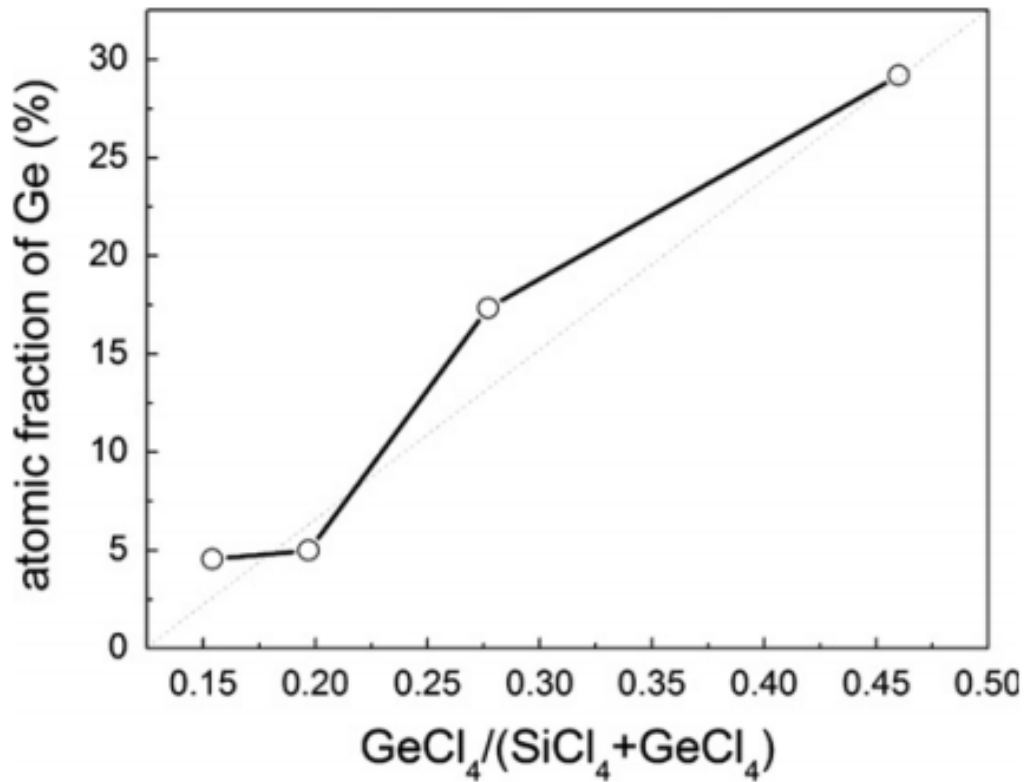
Figure 4-4 atomic fraction Atomic fraction in the SiGe nanopowder (y-axis), as measured by SEM-EDS, as a function of the germanium tetrachloride flow rate over the total precursor flow rate (x-axis).

Conclusions

We have presented extensive and conclusive evidence that silicon–germanium alloy nanocrystals can be produced using a non-thermal plasma reactor in combination with chlorinated precursors. The use of such precursors provides advantages with respect of hydrogenated precursors in terms of safety of handling and in terms of cost. In the future we will investigate the use of the plasma-produced nanocrystals in thermoelectric devices.

References

[1]   D. M. Rowe, *CRC handbook of thermoelectrics*. Boca Raton, FL: CRC Press, 1995.

[2]   M. S. Dresselhaus, G. Chen, M. Y. Tang, R. G. Yang, H. Lee, D. Z. Wang*, et al.*, "New directions for low-dimensional thermoelectric materials," *Advanced Materials,* vol. 19, pp. 1043-1053, Apr 20 2007.

[3]   G. Joshi, H. Lee, Y. C. Lan, X. W. Wang, G. H. Zhu, D. Z. Wang*, et al.*, "Enhanced Thermoelectric Figure-of-Merit in Nanostructured p-type Silicon Germanium Bulk Alloys," *Nano Letters,* vol. 8, pp. 4670-4674, Dec 2008.

[4]   S. K. Bux, R. G. Blair, P. K. Gogna, H. Lee, G. Chen, M. S. Dresselhaus*, et al.*, "Nanostructured Bulk Silicon as an Effective Thermoelectric Material," *Advanced Functional Materials,* vol. 19, pp. 2445-2452, Aug 10 2009.

[5]   C. W. Lin, S. Y. Lin, S. C. Lee, and C. T. Chia, "Structural and optical properties of silicon-germanium alloy nanoparticles," *Journal of Applied Physics,* vol. 91, pp. 2322-2325, Feb 15 2002.

[6]   F. Erogbogbo, T. H. Liu, N. Ramadurai, P. Tuccarione, L. Lai, M. T. Swihart*, et al.*, "Creating Ligand-Free Silicon Germanium Alloy Nanocrystal Inks," *Acs Nano,* vol. 5, pp. 7950-7959, Oct 2011.

[7]   L. Mangolini, E. Thimsen, and U. Kortshagen, "High-yield plasma synthesis of luminescent silicon nanocrystals," *Nano Letters,* vol. 5, pp. 655-659, Apr 2005.

[8]   R. Gresback, Z. Holman, and U. Kortshagen, "Nonthermal plasma synthesis of size-controlled, monodisperse, freestanding germanium nanocrystals," *Applied Physics Letters,* vol. 91, Aug 27 2007.

[9]   X. D. Pi and U. Kortshagen, "Nonthermal plasma synthesized freestanding silicon-germanium alloy nanocrystals," *Nanotechnology,* vol. 20, Jul 22 2009.

[10]   O. Yasar-Inceoglu, T. Lopez, E. Farshihagro, and L. Mangolini, "Silicon nanocrystal production through non-thermal plasma synthesis: a comparative study between silicon tetrachloride and silane precursors," *Nanotechnology,* vol. 23, Jun 29 2012.

[11]   S. F. Ren, W. Cheng, and P. Y. Yu, "Microscopic investigation of phonon modes in SiGe alloy nanocrystals," *Physical Review B,* vol. 69, Jun 2004.

[12]   M. I. Alonso and K. Winer, "Raman spectra of c-Si $_{1-x}$ Ge $_x$ alloys," *Physical Review B,* vol. 39, p. 10056, 1989.

Chapter 5 Core/Shell Silicon/Polyaniline Particles via In-flight Plasma-Induced Polymerization

Overview

Although silicon nanoparticles have potential applications in many relevant fields, there is often the need of post-processing steps to tune the property of the nanomaterial and to optimize it for targeted applications. In particular surface modification is generally necessary to both tune dispersibility of the particles in desired solvents to achieve optimal coating conditions, and to interface the particles with other materials to realize functional heterostructures. In this contribution we discuss the realization of core/shell silicon/polymer nanoparticles realized using a plasma-initiated in-flight polymerization process. Silicon particles are produced in a non-thermal plasma reactor using silane as a precursor. After synthesis they are aerodynamically injected into a second plasma reactor into which aniline vapor is introduced. The second plasma initiates the polymerization reactor leading to the formation of a 3–4 nm thick polymer shell surrounding the silicon core. The role of processing conditions on the properties of the polymeric shell is discussed. Preliminary results on the testing of this material as anode for lithium ion batteries are presented.

Introduction

Non-thermal plasmas have by now established themselves as a powerful nanoparticle synthesis and processing tool. While the initial focus concentrated on the production of silicon nanoparticles for applications in electronics [1-3], it was soon realized that the scalability of non-thermal plasma reactors is compatible with the large-scale production requirements inherent with energy-related applications, such as photovoltaics [4] and for light emission [5]. Most recently, the successful plasma synthesis of nanoparticles composed on other relevant materials such as ZnO [6] and Cu_2S [7] has been reported. While these reports demonstrate the promise of non-thermal plasma processing of materials, post-processing steps are often necessary to tune the nanoparticle property and to integrate them into functional devices. For instance, silicon nanoparticles are often functionalized using standard wet-chemistry techniques to make them dispersible in the desired solvents [8, 9]. This is necessary to realize high-quality films for the fabrication of nanoparticle-based light emitting devices (LEDs) [5] or to uniformly disperse particles into a polymer matrix for energy storage applications [10]. While surface modification via batch-processing in the liquid phase is a viable strategy, it lacks the capability of achieving fast-processing times and it can utilize significant amounts of solvents. This motivates the interest towards gas-phase post-processing techniques. For instance, the surface of silicon nanoparticles can be alkylated by reacting the particles in-flight with the appropriate molecular chain (typically an alkene) either using a thermally initiated reaction [11] or a non-thermal plasma initiated

reaction [12]. This last approach involves the use of two distinct plasma reactors in series. The first reactor converts the silicon precursor (silane) into nanoparticles while the second, after the addition of the organic molecule vapor, activates the surface grafting process. A similar approach has also been demonstrated for the in-flight coating of silicon particles with a fluorocarbon polymeric shell with the goal of stabilizing the particle optoelectronic properties against oxidation in air [13]. In-flight post-processing has also been successfully applied to the case of metallic nanoparticles which have been coated with a silica layer using a UV photoreactor [14].

In this contribution we investigate the in-flight coating of silicon nanoparticles with a polyaniline layer via the plasmainitiated polymerization of the appropriate monomer, in this case aniline. While plasma-induced polymerization has already been investigated for the surface modification of flat surfaces [15, 16], to our knowledge this is the first attempt of utilizing this process to coat nanoparticle surfaces in-flight. Our choice of polyaniline as a polymer shell is motivated by the potential use of silicon nanomaterials for lithium-ion battery applications. There are several issues hindering the use of nanosilicon for such application. Beside the fracturing of silicon particles due to the volume expansion upon lithiation, which can be easily resolved by using particles smaller than ~150 nm   [17], it is also important to (a) achieve a good electrical conductivity in the active layer [18-20] and (b) prevent the direct contact between the silicon particle and the standard electrolyte formulation (lithium hexafluorophosphate

in ethyl carbonate/diethyl carbonate mixture), which leads to the formation of an unstable and insulating solid electrolyte interface (SEI) onto the silicon surface [21]. We have therefore investigated the use of an in-flight non-thermal plasma coating approach to achieve core/shell silicon/polyaniline particles, and we have performed preliminary tests of this material as anode for lithium-ion batteries. Conducting polymers are already being investigated for such application in conjunction with silicon nanoparticles. The authors in [22] use a standard liquid-phase polymerization scheme to coat the surface of silicon particles with polyaniline and realize anodes with good capacity and stability upon cycling. A similar approach, although involving the formation of an hydrogel during the liquid-phase polymerization reaction, lead to the realization of anodes with lifetimes approaching 1000 cycles [23].

It would be highly desirable to realize similar materials using a scalable approach, such as the non-thermal plasma one, while avoiding liquid-phase batch reactions. This paper is organized as following: the nanoparticle synthesis and surface modification technique is described in details, confirming that we have successfully achieved a core/shell silicon/polymer structure. The influence of process parameters on the polymer structure and oxidation state has also been investigated. Preliminary results on the testing of this material in lithium-ion half cell batteries are discussed and recommendations for future work in this area are provided.

Experimental Details

Si/Polymer Core/Shell Nanoparticles Preparation

A schematic of the two-stage plasma reactor developed for the realization of core/shell silicon/polymer nanopowders is shown in Figure 5-1. Silicon nanoparticles are continuously nucleated and grown in a continuous flow non-thermal plasma reactor similar to the one described in [24]. The first reactor consists of a 1.25 cm outer diameter quartz tube. The first plasma is generated using a ring electrode placed 7 cm away from the ultratorr fitting downstream of the plasma. A 1 mm orifice is placed between the two reactors to effectively separate the two reaction volumes. The second
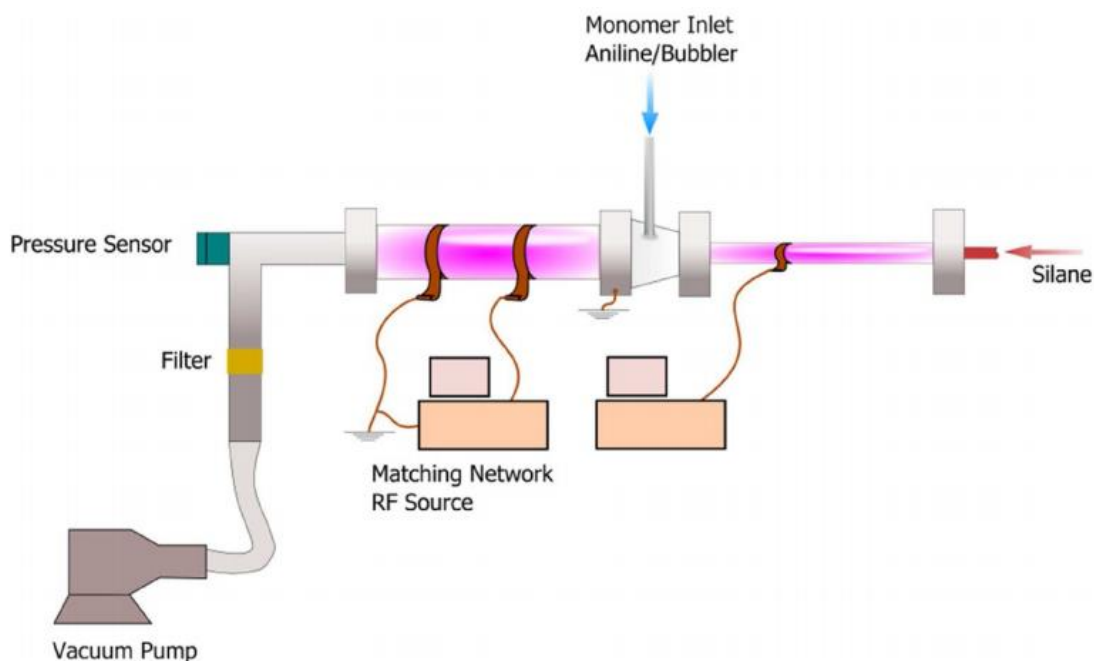
Figure 5-1 Schematic of the two-stage reactor used for the synthesis of silicon nanoparticles and their in-flight coating with a polymer shell.

reactor consists of a 2.54 cm outer diameter quartz tube with a ring electrode placed 10 cm downstream of the ultratorr vacuum fitting. Typically, 80 sccm of silane (SiH4) diluted in argon (1.37% by volume) is supplied to the system. For these conditions, the pressure in the first reactor is ~1000 Pa. The pressure in the second reactor is controlled using an automated butterfly valve and kept between 300 and 500 Pa Torr. The flow across the orifice separating the two reaction volumes is chocked, ensuring that the nucleation and growth reactions occurring in the first stage are effectively separated from the in-flight coating process occurring in the second reactor. The electrical power is supplied by two independent radio frequency (RF, 13.56 MHz) amplifiers. Typically 100 W is more than sufficient to produce crystalline material in the first reactor. A much lower power (13 W) is used in the second plasma reactor for the samples discussed in this chapter

Aniline is the typical precursor for the liquid-phase growth of a polyaniline (PANI). We choose to use the same monomer for our in-flight process. Aniline is fed into the system via an inlet placed immediately downstream of the orifice separating the two plasmas. Aniline is evaporated and carried to the reactor using a bubbler system. The bubbler pressure is kept constant and equal to 30 kPa (absolute pressure). In order to control and increase the aniline monomer flow rate, the bubbler is placed in an oil bath kept at 60 °C. 140 sccm of argon flows through the aniline bubbler. The calculated aniline flow rate, using data for the aniline vapor pressure available in chemistry

handbooks, is around 3.6 sccm. Hydrogen can also be added to the second non-thermal

plasma system via a separate supply line. The powder is collected by filtering

downstream of the second plasma. The production rate of Si/polymer powder is

approximately 90 mg h^{-1}. Si nanoparticles without polymer shell are produced using the

same system without igniting the second discharge for control experiments.

Material Characterization

The produced Si/polymer nanoparticles are characterized using variety of

techniques. Scanning electron microscopy (SEM), transmission electron microscopy

(TEM), x-ray photoelectron spectroscopy (XPS) and Fourier transform infrared

spectroscopy (FTIR) are performed to determine the size, structure, composition and

chemical nature of the produced powder. TEM is performed on a Tecnai T12 120 kV

transmission electron microscope. TEM samples are prepared by drop-casting a

dispersion of particles onto lacey carbon grids. A Nova NanoSEM 450 instrument is used

for SEM analysis. X-ray photoelectron spectroscopy (XPS) was performed on a Kratos

Axis Ultra^{DLD} XPS system equipped with an Al Kα monochromated x-ray source. The FTIR

characterization is performed using a Newport-Oriel modular spectrometer equipped

with a deuterated trigylcine sulfate (DTGS) detector. The spectra are recorded in the

400–5000 cm^{-1} wavenumber range. The samples are prepared by dispersing the powder

in chloroform by ultrasonication and by drop-casting onto a zinc selenide ATR crystal.

We monitor the absorption as the solvent evaporates and the data acquisition is

initiated only after the disappearance of any feature related to chloroform. The spectra are acquired with a 4 cm^{-1} of resolution and a scanning frequency of 40 kHz.

Electrode Preparation

The electrochemical performance of the plasma-produced nanomaterials is tested by preparing coin cell batteries and by testing them onto a potentiostat from Arbin Instruments. In a typical protocol, 40 mg of Si/polymer particles are added to 10 mg of multiwall carbon nanotubes (MWCNTs) to enhance the electrical conductivity of the layer. The MWCNTs are purchased from Sigma Aldrich (Part Number 724769, outer diameter 6–9 nm, length 5 µm). The mixture is dispersed in ethanol and ultrasonicated for 20 min. Copper foil is used as substrate and coated by drop-casting. The weight loading is obtained by baking at low temperature (100 °C) in a convection oven to remove any solvent residue and by measuring masses of the foil before and after coating. Typically, the weight loading is kept close to 1 mg cm^{-2}. In addition, the coating can be annealed under argon flow in a vacuum tube furnace capable of reaching 1000 °C. The coin cell batteries are assembled in a glove box filled with argon. Lithium foil is used as the counter electrode. A polymer film (from MTI Inc., part Number: EQ-bsf-0025-60C) is used as separator. A 1 M solution of lithium hexafluorephosphate (LiPF6) in ethylene carbonate (EC)/diethyl carbonate (DEC) (1:1 v/v) (from MTI Inc., part Number: EQ-Be-LiPF6) is used as electrolyte. The cells are charged and discharged between 0 V and 1.5 V.

Results and Discussions

In Figure 5-2 we show a selection of TEM images for particles which have undergone the in-flight surface-initiated polymerization process. Figure 5.2(a) indicates that the particles have a spherical shape with sizes between 10 and 20 nm. The selected area diffraction pattern shown in the inset of figure 5.2(a) confirms that they have crystalline structure. The higher magnification images in figures 5.2(b) and (c) suggest that an amorphous shell surrounds the particle core. The thickness of the amorphous shell is between 2 and 3 nm, which exceeds the typical thickness for a native oxide layer growth at room temperature (~1 nm).

We have determined the particle size distribution for this sample by analyzing the TEM bright field images. The size of at least 100 particles has been measured and
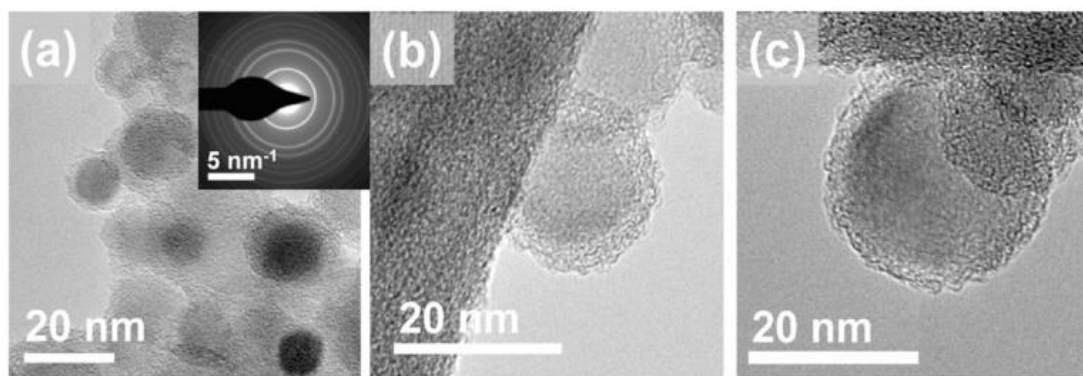
Figure 5-2 TEM micrographs of silicon nanoparticles coated with a polyaniline shell. A lower magnification image is shown in (a) indicating that the particles are around 10 nm in size. Higher magnification images (b) and (c) show that the particles are coated with a 2–3 nm thick amorphous shell. The selected area diffraction pattern shown in the inset of (a) confirms that the particles have a crystalline structure.

the corresponding size distribution is shown in Figure 5-3. We show the results of the same analysis but for a sample which was not coated in-flight with polyaniline (i.e. without flowing aniline and without igniting the second discharge). The nanoparticle synthesis parameters for the first plasma reactor are unchanged compared to the aniline-coated sample. The average particle size is estimated by fitting the distribution with a lognormal function. For the uncoated sample we find an average of 12.6 nm, while the average is 17.3 nm for the coated sample. This is consistent with the polyaniline shell thickness of approximately 2–3 nm shown in Figure 5-2.
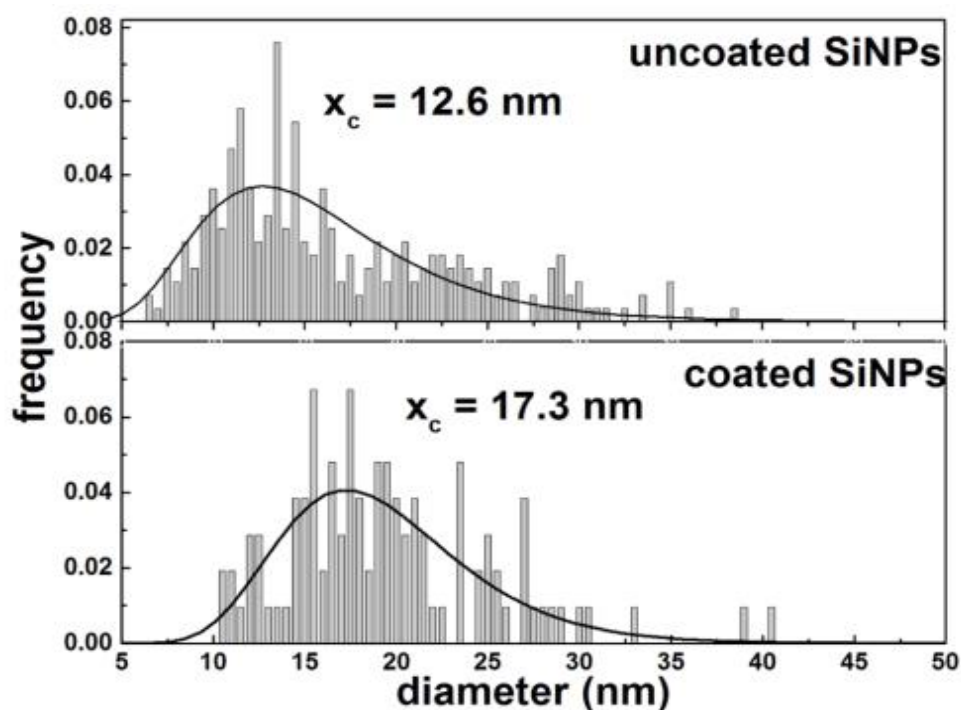
Figure 5-3 Particle size distributions for silicon particles without (top) and with (bottom) polyaniline shell. The continuous lines result from fitting with a lognormal function. The size distributions are obtained by analyzing several TEM micrographs.

In Figure 5-4 and Figure 5-5 we present the results of chemical analysis (FTIR and XPS respectively) performed on the nanoparticles produced in our 2-stages reactor. We have supplied hydrogen to the second non-thermal plasma with variable flow rate in the 0–5 sccm range with the goal of investigating its role on the chemical nature of the polymer shell. Typically, polyaniline obtained from standard liquid-phase polymerization techniques can be present in different forms with greatly different electrical transport
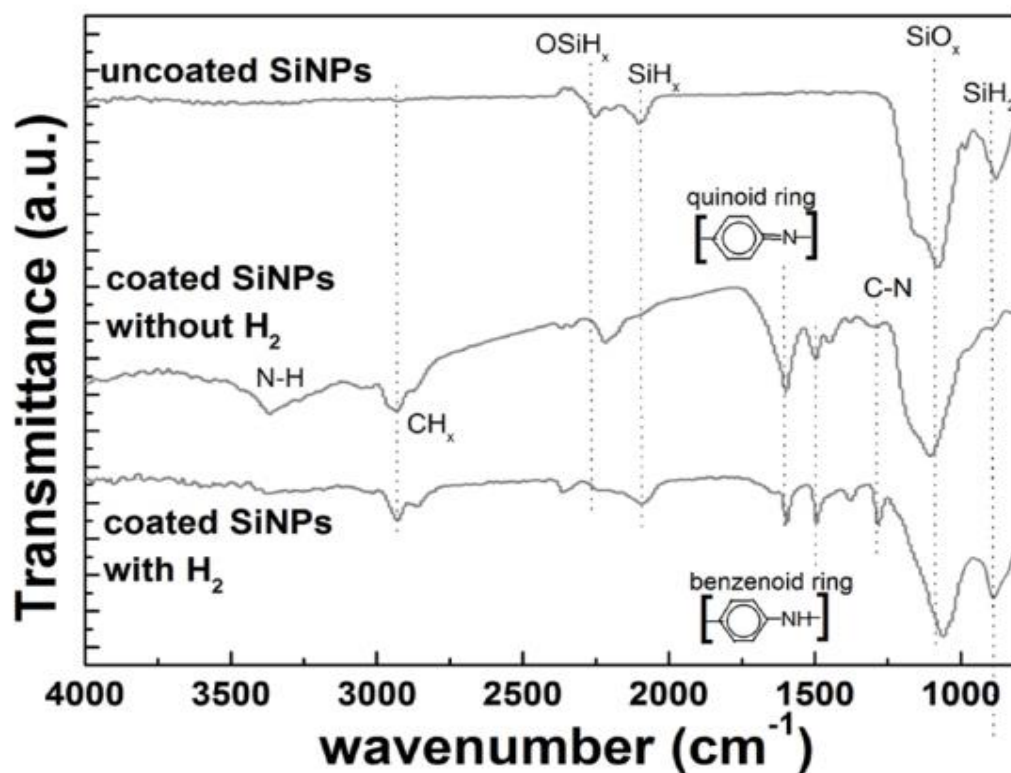
Figure 5-4 FTIR transmittance spectra for silicon nanoparticles without any polymeric coating (top spectrum) and with polymeric coating (two bottom spectra). The middle spectrum corresponds to a sample which has been coated without any addition of hydrogen to the second plasma reactor, while 5 sccm of hydrogen has been added to the second reactor for the case of the bottom spectrum. See text for a detailed interpretation of the spectra.
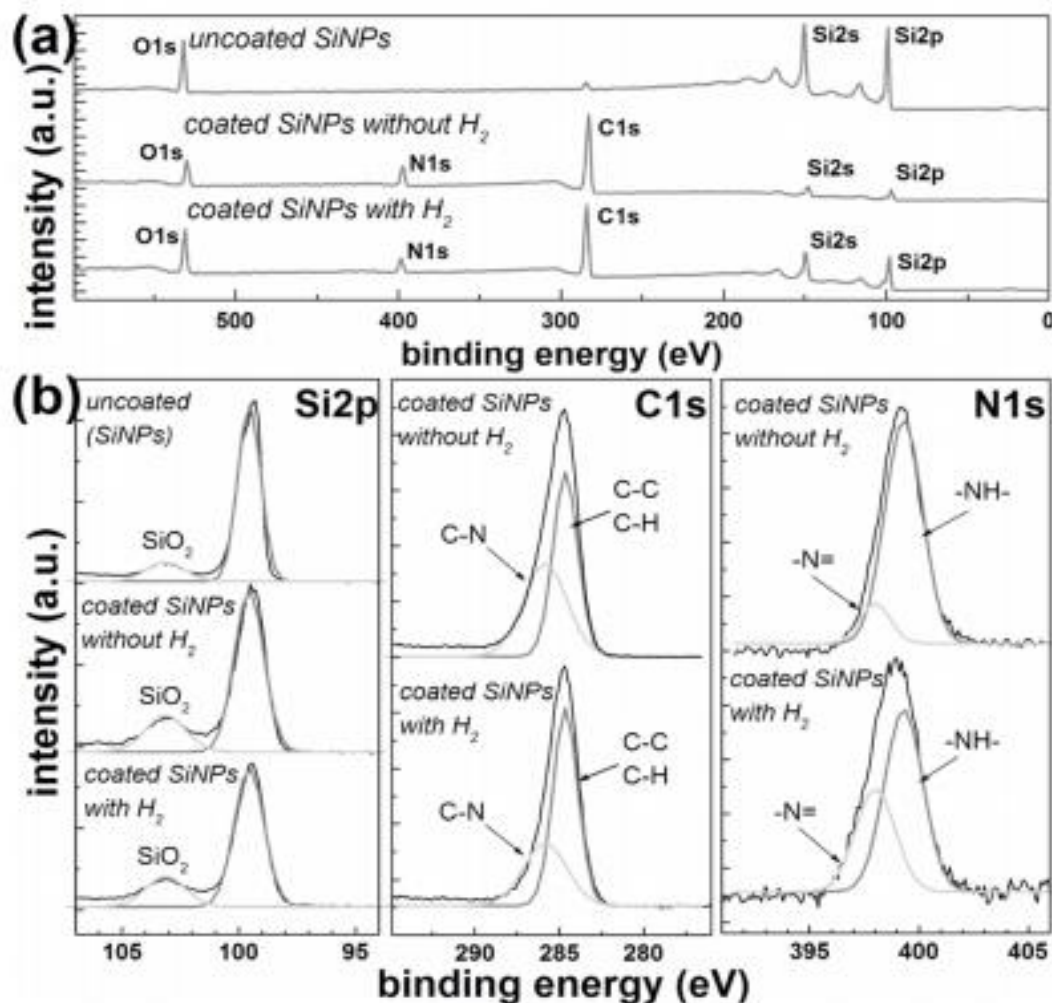
Figure 5-5 (a) XPS survey scans for samples produced without any additional coating (control sample) and for polymer-coated samples, with and without addition of hydrogen to the second plasma reactor. (b) High resolution scans for the Si2p, C1s and N1s peaks for the same samples shown in 5a. The C1s and N1s peaks are not shown for the control sample since it is not coated by the polymer shell.

properties [25]. To briefly summarize, polyaniline is in the pernigraniline form when it is composed only of quinoid units (i.e. with the imine =N- group binding the aromatic rings) and it is in the leucoemeraldine form when composed of only benzenoid units (i.e. with the amine –NH- group binding the aromatic rings). When equal fractions of quinoid

and benzenoid units are present, polyaniline is in the emeraldine form. The protonated form of emeraldine (emeraldine salt) is conductive and the desired one in most applications. Protonation can be achieved in standard liquid-phase produced polyaniline by post-treatment with an acid. The FTIR data for our samples are shown in figure 4. The uncoated silicon particles (top spectrum) show clear sign of surface oxidation (broad peak between 1000 and 1100 cm^{-1}). These particles were in fact exposed to air before being deposited onto the ATR crystal for analysis. Peaks due to residual surface hydride moieties are present around 860 cm^{-1} and 2100 cm^{-1}. The 860 cm^{-1} is due to scissor-mode vibrations in SiH$_2$, while the 2100 cm^{-1} is the stretching mode vibration in SiH$_x$ (1 < x < 3) [26]. A satellite of the silicon hydride peak at 2100 cm^{-1} is present at higher wavenumber (2230 cm^{-1}) and it is well-known to be due to surface hydrides with backbonded oxygen. For the case of the coated particles we show the spectra for both a sample produced without the addition of hydrogen (middle spectrum) to the second discharge and a sample with the addition of 5 sccm of hydrogen (bottom spectrum) to the second reactor. Both of these samples show clear sign of oxidation of the silicon surface, suggesting that the polymer shell is not an effective blocking layer to oxygen diffusion. Interestingly, the configuration of residual surface silicon hydrides is different in these two samples. When hydrogen is added to the second plasma, we observe features that are similar to those obtained for the uncoated sample, such as the SiH$_2$ scissor mode peak at 860 cm^{-1} and the SiH$_x$ stretching mode peak at 2100 cm^{-1} with satelline peak at 2230 cm^{-1} (although less noticeable for the case of the bottom

112

spectrum). Analysis of the middle spectrum reveals that the 860 cm^{-1} peak is absent

when hydrogen is not added to the second reactor and that the peak at 2100 cm^{-1} is

absent as well. Another peak is present at 2180 cm^{-1}, at lower wavenumber compared

to the satellite peak due to the stretching mode of silicon hydrides moieties in presence

of back-bonded oxygen. We tentatively attribute this feature to silicon hydride modes in

presence of nitrogen back-bonding, since the lower shift compared to oxygen back-

bonding is consistent with the lower atomic mass of nitrogen. This suggests that some

nitridation of the surface has occurred although it is difficult to comment to what extent

this takes place, given the partial overlap of the broad absorption features due to silicon

oxide (1000–1100 cm^{-1}) and silicon nitride (900–1100 cm^{-1}) [27, 28]. The sample

exposed to aniline without any addition of hydrogen also shows clear absorption from

N–H at 3370 cm^{-1}, a feature usually observed in amines [29]. Both samples exposed to

aniline show clear signatures from carbon-nitrogen stretching modes around 1300 cm^{-1}

[30, 31] and from the CH$_x$ stretching mode at 2950 cm^{-1}. Most importantly, signatures

from both the quinoid and the benzenoid units are clear at 1600 cm^{-1}and 1500 cm^{-1}

respectively [30, 31]. The magnitude of these two signals is similar when hydrogen is

added to the second discharge, while the absorption from the quinoid group at 1600

cm^{-1} is somewhat larger when hydrogen is not added to the gas-phase reactor. This may

also be due to a partial overlap of the quinoid signal at 1600 cm^{-1} with absorption from

the N-H group, which also leads to absorption at the same wavenumber [29]. The

presence of N-H groups in this sample is confirmed by the presence of a broad peak at

3370 cm^{-1}, as discussed earlier. We should also point out that the absorption from the C–N bond around 1300 cm^{-1} is larger for the case of the sample processed in presence of hydrogen. It has been reported that this absorption feature is weaker when only benzenoid units are present in the polymer while it increases when the fraction of quinoid units is higher [32]. This is a consequence of the different electronic configuration of this bond in these two structures [32]. To a certain extent this contradicts the observation of slightly higher absorption from the quinoid group at 1600 cm^{-1} for the sample produced without hydrogen (middle spectrum). A quantitatively more precise analysis of the relative contribution from quinoid and benzenoid units is provided by XPS analysis.

The results from the FTIR analysis suggest that the plasma-grown polymeric shell has many features in common with those of liquid-phase produced polyaniline, such as the one described in [31] also for the case of silicon nanocrystals. FTIR analysis suggests that there are subtle changes in the chemical nature of the polymer as the gas-phase composition is tuned. We have performed XPS analysis to further investigate this. The results of the XPS analysis are shown in Figure 5-5. For these scans the hydrogen flow rate was 5 sccm, identical to the one used for the FTIR analysis shown in Figure 5-4. Charge neutralization was performed during the data acquisition. To eliminate any residual shift in energy due to charging effects, we have monitored the position of the Si2p peak which is expected to have it maximum at 99.3 eV. We have shifted the energy

axis in our spectra accordingly. Figure 5-5(a) shows the survey scans for uncoated silicon

particles (top), coated without any hydrogen addition to the second plasma (middle)

and with hydrogen addition to the second plasma (bottom). These scans show the

presence of silicon, carbon, nitrogen and oxygen in our samples. In table 1we show the

elemental composition of the samples based on the analysis of these XPS spectra. The

presence of peaks from carbon and nitrogen confirms the grafting of aniline onto the

particle surface. The addition of hydrogen causes a decrease in amounts of carbon and

nitrogen which we interpret as a reduction in the thickness of the polymer shell.

In Figure 5-5(b) we show the high-resolutions scans for the Si2p, C1s and N1s

peaks for samples exposed to aniline with and without hydrogen addition to the gas-

phase reactor. For completeness we show the Si2p spectrum for the uncoated particles

as well. The Si2p signal has been deconvoluted using two gaussian profiles. The fitting

procedure, performed using the Origin data analysis software, finds two peaks at 99.3

eV and at 103 eV. The peak at 103 eV is routinely assigned to silicon oxide. We cannot

rule out the presence of silicon-nitrogen bonding in our samples, which would appear as

a contribution at intermediate energies between the Si2p peak at 99.3 eV and the oxide

peak at 103 eV, but it is difficult to reliably quantify its presence in our aniline-treated

samples. As already mentioned earlier during the discussion of the FTIR data, it is also

not simple to distinguish between absorption from silicon oxide and silicon nitride. We

conclude that the silicon nitride contribution in our material is probably low and due to

the anchoring of aniline onto the particle surface via Si–N bonding. The density of such bonds in our samples is likely much lower than that of Si–O bonds since the presence of a polymer shell does not prevent the growth of a native oxide layer, which typically has a thickness of 1 nm for this kind of particles [33]. The XPS data shown in figure 5for the Si2p peak confirms that the amount of silicon oxide present in our coated samples is very similar to that present in the control, untreated sample with a native oxide surface. The C1s peak around 285 eV has also been deconvoluted using two gaussian profiles into a contribution peaking at 284.6 eV due to C–C and C–H bonding and a contribution peaking at 285.5 eV due to C–N bonding [34]. This analysis confirms the presence of the carbon-nitrogen bonding expected for polyaniline films, and also indicates that there is only a minor change in the ratio between the 284.6 eV peak (C–C and C–H) and the 285.5 eV peak (C–N) when hydrogen is added to the second plasma reactor. The most important change as a function of processing conditions is observed for the N1s peak centered around 400 eV. There is extensive literature on the identification of imine or amine configurations using XPS [25, 31, 35, 36]. The imine group is usually assigned to a peak centered at 398 eV, whereas the amine group is identified by a peak centered at 399.3 eV [25, 31, 35, 36]. We have deconvoluted the N1s peak using two gaussian profiles and found that the amine bonding is predominant for the sample processed without hydrogen addition, while a clear relative increase in the signal from the imine group is observed when hydrogen is added to the gasphase in the second plasma step. This result is consistent with the FTIR data which shows a large absorption at 3350 cm^{-1}

116

from the N–H group for samples produced without addition of hydrogen. Also, as already mentioned before, the samples produced with hydrogen show a larger absorbance from the C–N peak around 1300 cm^{-1}, consistent with a higher density of quinoid groups [32]. While this result may be counterintuitive, we offer a hypothesis that justifies this behavior. While the elemental carbon-to-nitrogen ratio is does not change significantly after the addition of hydrogen to the gas-phase (this ratios between the C1s and the N1s peak areas is 6.2 for the sample to which hydrogen is not added and 7.5 for the sample to which hydrogen is added, as reported in table 1), we observe a change in the carbon-to-silicon ratio, from 11 to 2.6 as hydrogen is added to the system (see table 1). This is due to the reduced thickness of the polymer shell, which results in a higher sensitivity of the XPS to the silicon surface. TEM data, not shown here for brevity, confirms that the polymer shell is much thinner when hydrogen is added to the second plasma. It is in fact impossible to conclusively measure the thickness of the polymer shell and to distinguish it from the native oxide layer. FTIR data is consistent with this hypothesis, since the spectrum for the sample produced with hydrogen addition shows many features similar to that of the control uncoated sample, in particular with respect of the higher density of silicon hydride moieties as indicated by the peaks at 2100 cm^{-1} and at 860 cm^{-1}. The 860 cm^{-1} scissor mode peak is absent for the sample processed without hydrogen addition, and the Si-H$_x$ stretching vibrations are shifted to a wavenumber (2180 cm^{-1}) that is intermediate between that of the unoxidized surface (2100 cm^{-1}) and the 2230 cm^{-1} feature due to back-bonding to oxygen. As discussed

earlier, we tentatively motivate this shift as back-bonding of the silicon to nitrogen. The addition of hydrogen to the gas stream likely deactivates the polymerization process, leading to both a lower density of aniline molecules grafted onto the particle surface and to a lower thickness of the polymer shell. Another reasonable consequence of this is the higher susceptibility of the polymer shell to aging and oxidation, which has been shown to correlate in XPS analysis with the higher density of imine groups compared to amine groups [32], consistent with our results.

To summarize, the combination of FTIR and XPS analysis confirms the successful coating of the silicon particles with a polyaniline-like polymeric shell. To our knowledge this is the first report of the in-flight plasma-induced polymerization of aniline onto nanoparticles. Such material could be relevant for several applications such as for sensing and for biological applications. Our focus is in energy-related applications and we have therefore decided to investigate the use of these nanoparticles for energy storage.

In order to test the quality of the plasma-polymerized material, we have prepared half-cells using lithium foil as counter electrode. Si/polymer nanoparticles produced without the addition of hydrogen to the second reactor have been dispersed in ethanol, mixed with multi-walled carbon nanotubes and coated by drop casting onto copper foil. Nanotubes are added to the electrode material to increase its conductivity [10]. A SEM micrograph of one of this coating is shown in Figure 5-6. The film appears to
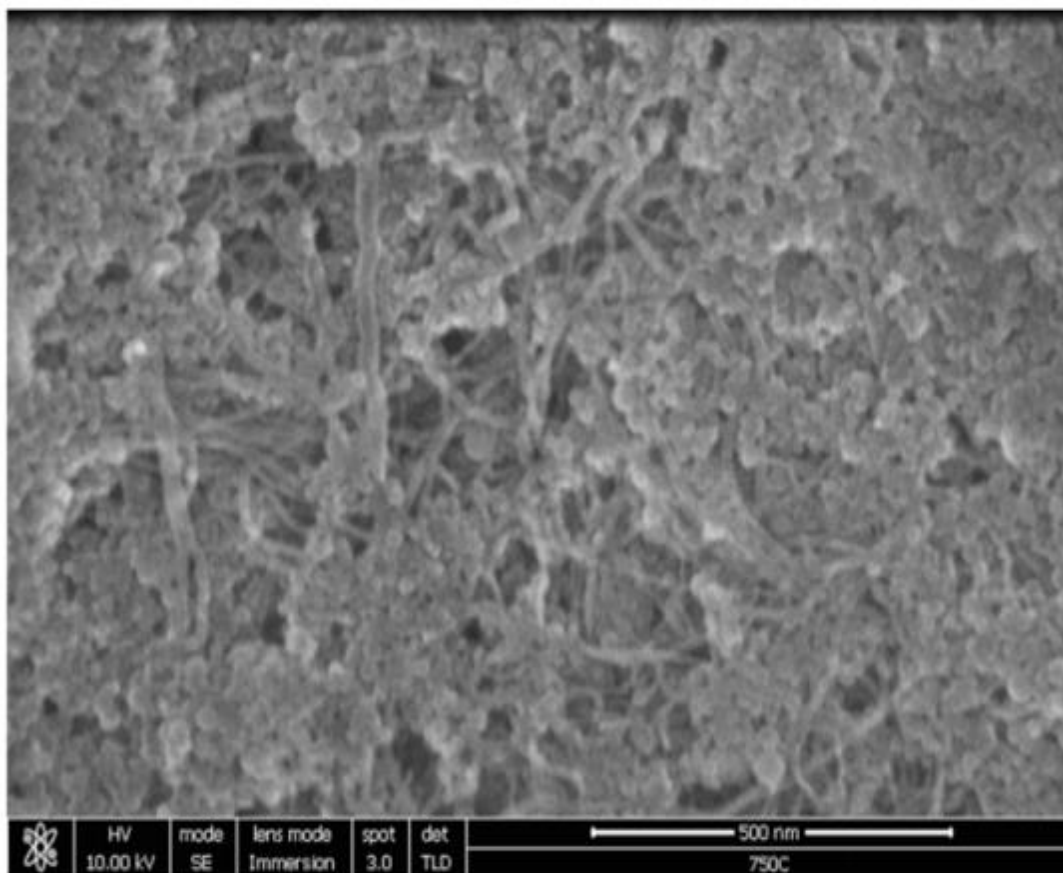
Figure 5-6 SEM micrograph of a coating of Si/polymer core/shell particles used for testing as anode for lithium-ion batteries. MWCNTs are added to enhance the conductivity of the layer.

be uniform and with a relatively low density, which is actually necessary to make sure that the electrolyte can penetrate the active layer and enable the device functionality.

Control samples have been prepared using nanoparticles without the polymer shell. We have found that the presence of the shell alone is not sufficient to stabilize the device performance. Without any additional post-treatment, these batteries do not survive the first charge-discharge cycle, and the presence of the polymer shell does not

offer a clear advantage compared to the non-coated particles. In our opinion this is due to two factors. First the electrical conductivity of the polymer shell is probably low because of its oxidation state. The data shown in Figure 5-4 and Figure 5-5 suggests that for the material is in the leucoemeraldine form (i.e. fully reduced benzenoid units are dominant). For the case of liquidphase polymerized polyaniline, optimal electrical transport is obtained when using the emeraldine form (which has equal density of quinoid and benzenoid units) especially after chemical doping. We have performed preliminary attempts to chemically dope our material via immersion into an acid bath, although such attempts have so far failed, likely because of the starting oxidation state of the polymeric shell. In addition, we have yet to find the optimal binder that can guarantee mechanical stability of the active layer upon cycling. This is particularly crucial for the case of silicon, since its large volume change during cycling generates significant stress in the film.

We have therefore performed high-temperature annealing of the coating in order to improve its mechanical integrity with the additional goal of increasing the electrical conductivity of the carbon component. This approach sacrifices the theoretical advantages offered by having a potentially conductive polymer shell. In this case the polymer shell acts as a precursor to the formation of an amorphous carbon matrix which surrounds the silicon particles [10]. It is desirable to start with particles that are uniformly coated by the polymer to improve the structural quality of the film after

annealing. We have performed several annealing test using a vacuum furnace continuously flushed with a small flow rate of argon, and established that our material shows clear improvement in cycling stability after annealing at 550 °C. In Figure 5-7 we compare the discharge capacity in units of m Ah/gram for an electrode annealed at this temperature compared to a nonannealed sample. While the non-annealed sample quickly decays to practically zero capacity within 10 cycles, the annealed electrode achieves significantly higher specific capacity in the first cycle ($\sim$2600 mAh gram^{-1}) and
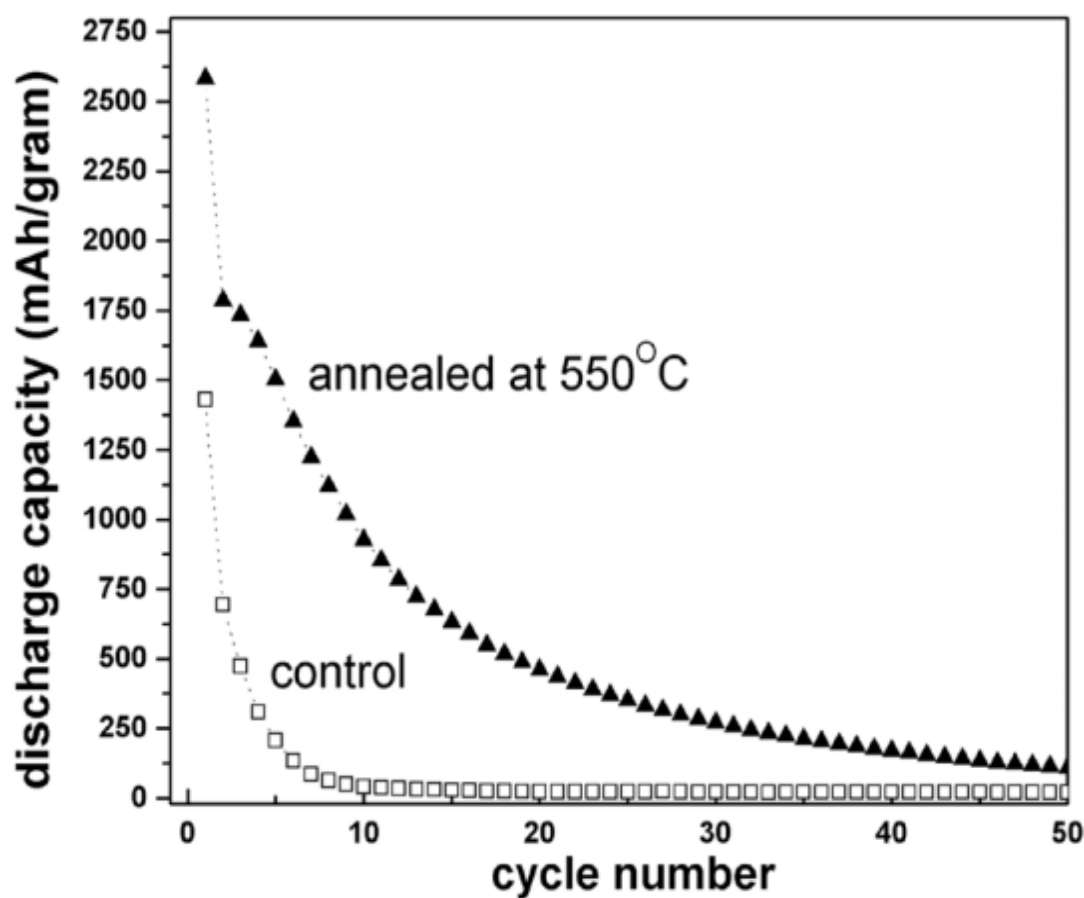

Figure 5-7 Discharge capacity as a function of cycle number for a control sample (not annealed) and a sample annealed in argon at a temperature of 550 °C.

maintains a capacity exceeding 500 mAh gram^{-1} for 20 cycles.

It is important to also mention that there are additional limitations to this process due to the inherently energetic environment provided by non-thermal plasmas [37]. We have found that it is important to supply very low power to the second discharge (13 W, barely sufficient to sustain the plasma) since running the system at even slightly higher power (20 W) leads to the carbonization of the silicon particle and to the formation of a silicon carbide interface between the silicon and the carbon-based shell. This phenomenon has also been observed for a similar system during in-flight coating of the silicon particles with an amorphous carbon shell starting from acetylene as precursor [38]. In Figure 5-8 we show the XRD spectrum for a sample produced using a power of 20 W in the second non-thermal plasma. A clear peak corresponding to the (1 1 1) plane of 3C-SiC is identifiable. Silicon carbide does not participate to the lithiation process therefore the carbonization reaction is detrimental to the device performance [39]. The ability of a non-thermal process to form silicon carbide, a high-melting point material, is remarkable and will be subject of future investigation.

Figure 5-9 represents collected samples that are prepared using two-stage non-thermal plasma process. The powder is collected on the stainless steel filter at different second plasma power input. We obtained that while 13 W sufficient to sustain the plasma, higher powers causes the formation of silicon carbide between silicon nanoparticles and polymer shell.
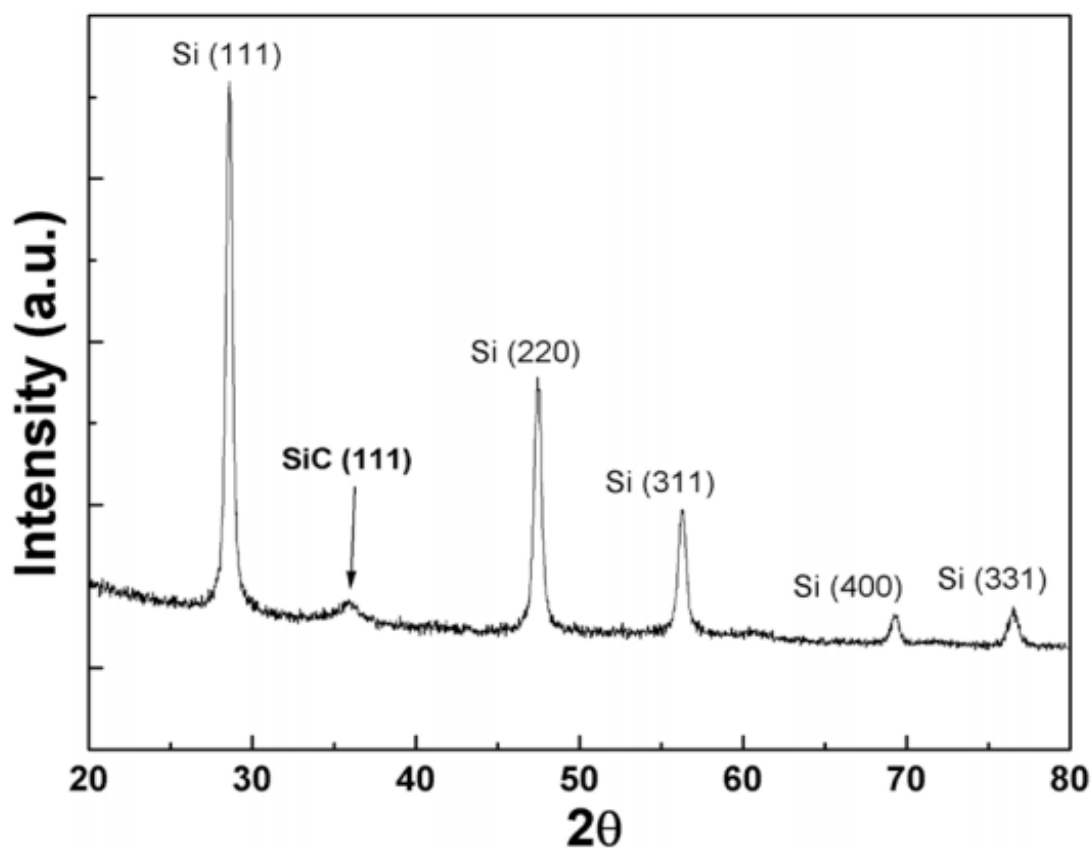

Figure 5-8 XRD spectrum of powder produced with a 20 W input electrical power in the second plasma reactor compared to the 13 W used for the Si/polymer core/shell powder. A clear peak corresponding to the (1 1 1) plane of silicon carbide is distinguishable.
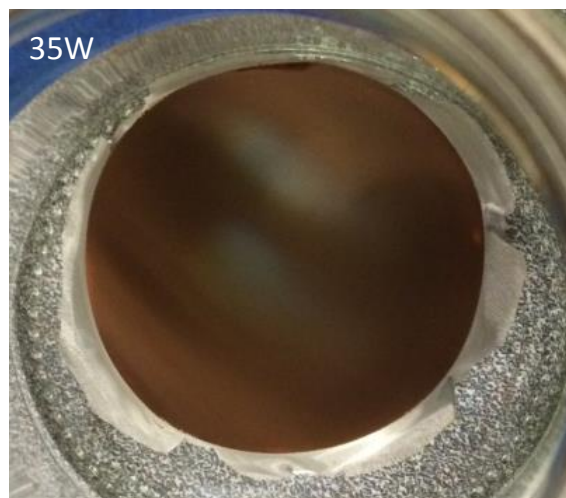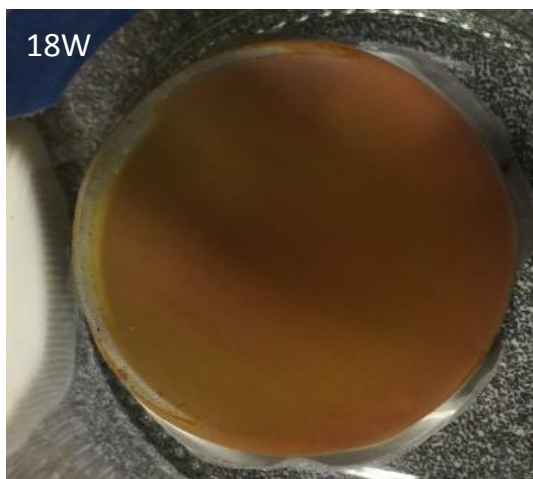
Figure 5-9 Collected powder on stainless steel filters using two-stage plasma polymerization process at 18 W, 35 W, 60 W, and 100 W

Conclusions

A non-thermal plasma-based process for the synthesis of silicon nanoparticles and their in-flight coating with a plasma polymerized shell has been developed. This process takes advantage of the many unique properties of non-thermal plasmas, such as the unipolar charging of the particles and the presence of highly reactive species, to produce core/shell silicon/polyaniline-like nanoparticles. We have demonstrated that it is possible to tune the chemistry of the shell by modifying the gas-phase composition during the polymerization step. We have performed a preliminary investigation of the use of these nanoparticles in electrochemical energy storage applications. The coating of the silicon particle with a polymer shell offers a way to uniformly disperse the particles into a carbon matrix after high-temperature treatment. While further improvements are needed before being directly applicable in such applications, we report a promising improvement in the stability of an anode for lithium-ion batteries based on such material, compared to the case of uncoated silicon particles.

References

[1]   M. Otobe, T. Kanai, T. Ifuku, H. Yajima, and S. Oda, "Nanocrystalline silicon formation in a SiH4 plasma cell," *Journal of Non-Crystalline Solids,* vol. 198, pp. 875-878, May 1996.

[2]   A. Dutta, M. Kimura, Y. Honda, M. Otobe, A. Itoh, and S. Oda, "Fabrication and electrical characteristics of single electron tunneling devices based on Si quantum dots prepared by plasma processing," *Japanese journal of applied physics,* vol. 36, p. 4038, 1997.

[3]   Y. P. Ding, Y. Dong, A. Bapat, J. D. Nowak, C. B. Carter, U. R. Kortshagen*, et al.*, "Single nanoparticle semiconductor devices," *Ieee Transactions on Electron Devices,* vol. 53, pp. 2525-2531, Oct 2006.

[4]   C.-Y. Liu, Z. C. Holman, and U. R. Kortshagen, "Hybrid solar cells from P3HT and silicon nanocrystals," *Nano letters,* vol. 9, pp. 449-452, 2008.

[5]   K.-Y. Cheng, R. Anthony, U. R. Kortshagen, and R. J. Holmes, "Hybrid Silicon Nanocrystal–Organic Light-Emitting Devices for Infrared Electroluminescence," *Nano letters,* vol. 10, pp. 1154-1157, 2010.

[6]   P. Felbier, J. Yang, J. Theis, R. W. Liptak, A. Wagner, A. Lorke*, et al.*, "Highly luminescent ZnO quantum dots made in a nonthermal plasma," *Advanced Functional Materials,* vol. 24, pp. 1988-1993, 2014.

[7]   E. Thimsen, U. R. Kortshagen, and E. S. Aydil, "Plasma synthesis of stoichiometric Cu 2 S nanocrystals stabilized by oleylamine," *Chemical Communications,* vol. 50, pp. 8346-8349, 2014.

[8]   X. Li, Y. He, and M. T. Swihart, "Surface functionalization of silicon nanoparticles produced by laser-driven pyrolysis of silane followed by HF-HNO3 etching," *Langmuir,* vol. 20, pp. 4720-4727, 2004.

[9]   F. Hua, M. T. Swihart, and E. Ruckenstein, "Efficient surface grafting of luminescent silicon quantum dots by photoinitiated hydrosilylation," *Langmuir,* vol. 21, pp. 6054-6062, 2005.

[10]   L. Zhong, J. Guo, and L. Mangolini, "A stable silicon anode based on the uniform dispersion of quantum dots in a polymer matrix," *Journal of Power Sources,* vol. 273, pp. 638-644, 2015.

[11]   Y.-C. Liao and J. T. Roberts, "Self-assembly of organic monolayers on aerosolized silicon nanoparticles," *Journal of the American Chemical Society,* vol. 128, pp. 9061-9065, 2006.

[12]   L. Mangolini and U. Kortshagen, "Plasma-Assisted Synthesis of Silicon Nanocrystal Inks," *Advanced Materials,* vol. 19, pp. 2513-2519, 2007.

[13]   X. Pi, R. Liptak, J. D. Nowak, N. Wells, C. Carter, S. Campbell*, et al.*, "Air-stable full-visible-spectrum emission from silicon nanocrystals synthesized by an all-gas-phase plasma approach," *Nanotechnology,* vol. 19, p. 245603, 2008.

[14]   A. M. Boies, J. T. Roberts, S. L. Girshick, B. Zhang, T. Nakamura, and A. Mochizuki, "SiO2 coating of silver nanoparticles by photoinduced chemical vapor deposition," *Nanotechnology,* vol. 20, p. 295604, 2009.

[15]   D. S. Wavhal and E. R. Fisher, "Hydrophilic modification of polyethersulfone membranes by low temperature plasma-induced graft polymerization," *Journal of Membrane Science,* vol. 209, pp. 255-269, 2002.

[16]   S.-D. Lee, G.-H. Hsiue, P. C.-T. Chang, and C.-Y. Kao, "Plasma-induced grafted polymerization of acrylic acid and subsequent grafting of collagen onto polymer film as biomaterials," *Biomaterials,* vol. 17, pp. 1599-1608, 1996.

[17]   X. H. Liu, L. Zhong, S. Huang, S. X. Mao, T. Zhu, and J. Y. Huang, "Size-dependent fracture of silicon nanoparticles during lithiation," *Acs Nano,* vol. 6, pp. 1522-1531, 2012.

[18]   J. Guo, A. Sun, X. Chen, C. Wang, and A. Manivannan, "Cyclability study of silicon–carbon composite anodes for lithium-ion batteries using electrochemical impedance spectroscopy," *Electrochimica Acta,* vol. 56, pp. 3981-3987, 2011.

[19]   C. Martin, O. Crosnier, R. Retoux, D. Bélanger, D. M. Schleich, and T. Brousse, "Chemical Coupling of Carbon Nanotubes and Silicon Nanoparticles for Improved Negative Electrode Performance in Lithium-Ion Batteries," *Advanced Functional Materials,* vol. 21, pp. 3524-3530, 2011.

[20]   J. H. Ryu, J. W. Kim, Y.-E. Sung, and S. M. Oh, "Failure modes of silicon powder negative electrode in lithium secondary batteries," *Electrochemical and Solid-State Letters,* vol. 7, pp. A306-A309, 2004.

[21]   H. Wu, G. Chan, J. W. Choi, Y. Yao, M. T. McDowell, S. W. Lee*, et al.*, "Stable cycling of double-walled silicon nanotube battery anodes through solid-electrolyte interphase control," *Nature nanotechnology,* vol. 7, pp. 310-315, 2012.

[22]   M. Kummer, J. Badillo, A. Schmitz, H.-G. Bremes, M. Winter, C. Schulz*, et al.*, "Silicon/polyaniline nanocomposites as anode material for lithium ion batteries," *Journal of The Electrochemical Society,* vol. 161, pp. A40-A45, 2014.

[23]   H. Wu, G. Yu, L. Pan, N. Liu, M. T. McDowell, Z. Bao*, et al.*, "Stable Li-ion battery anodes by in-situ polymerization of conducting hydrogel to conformally coat silicon nanoparticles," *Nature communications,* vol. 4, 2013.

[24]   L. Mangolini, E. Thimsen, and U. Kortshagen, "High-yield plasma synthesis of luminescent silicon nanocrystals," *Nano Letters,* vol. 5, pp. 655-659, Apr 2005.

[25]   E. Kang, K. Neoh, and K. Tan, "Polyaniline: a polymer with many interesting intrinsic redox states," *Progress in Polymer Science,* vol. 23, pp. 277-324, 1998.

[26]   D. C. Marra, E. A. Edelberg, R. L. Naone, and E. S. Aydil, "Silicon hydride composition of plasma-deposited hydrogenated amorphous and nanocrystalline silicon films and surfaces," *Journal of Vacuum Science & Technology A: Vacuum, Surfaces, and Films,* vol. 16, pp. 3199-3210, 1998.

[27]   N. M. Park, S. H. Kim, G. Y. Sung, and S. J. Park, "Growth and size control of amorphous silicon quantum dots using SiH4/N2 plasma," *Chemical Vapor Deposition,* vol. 8, pp. 254-256, 2002.

[28]   C.-H. Cho, B.-H. Kim, T.-W. Kim, S.-J. Park, N.-M. Park, and G.-Y. Sung, "Effect of hydrogen passivation on charge storage in silicon quantum dots embedded in silicon nitride film," *Applied Physics Letters,* vol. 86, pp. 143107-143107-3, 2005.

[29]   J. B. Lambert, *Introduction to organic spectroscopy*. New York: Macmillan, 1987.

[30]   S.-B. Yoon, E.-H. Yoon, and K.-B. Kim, "Electrochemical properties of leucoemeraldine, emeraldine, and pernigraniline forms of polyaniline/multi-wall carbon nanotube nanocomposites for supercapacitor applications," *Journal of Power Sources,* vol. 196, pp. 10791-10797, 2011.

[31]   Z. Li, M. Swihart, and E. Ruckenstein, "Luminescent silicon nanoparticles capped by conductive polyaniline through the self-assembly method," *Langmuir,* vol. 20, pp. 1963-1971, 2004.

[32]   E. Kang, K. Neoh, T. Tan, S. Khor, and K. Tan, "Structural studies of poly (p-phenyleneamine) and its oxidation," *Macromolecules,* vol. 23, pp. 2918-2926, 1990.

[33]   O. Yasar-Inceoglu, T. Lopez, E. Farshihagro, and L. Mangolini, "Silicon nanocrystal production through non-thermal plasma synthesis: a comparative study between silicon tetrachloride and silane precursors," *Nanotechnology,* vol. 23, Jun 29 2012.

[34]   Y. Chen, E. Kang, K. Neoh, S. Lim, Z. Ma, and K. Tan, "Intrinsic redox states of polyaniline studied by high-resolution X-ray photoelectron spectroscopy," *Colloid and polymer Science,* vol. 279, pp. 73-76, 2001.

[35]   B. C. Beard and P. Spellane, "XPS evidence of redox chemistry between cold rolled steel and polyaniline," *Chemistry of materials,* vol. 9, pp. 1949-1953, 1997.

[36]   S. Golczak, A. Kanciurzewska, M. Fahlman, K. Langer, and J. J. Langer, "Comparative XPS surface study of polyaniline thin films," *Solid State Ionics,* vol. 179, pp. 2234-2239, 2008.

[37]   T. Lopez and L. Mangolini, "On the nucleation and crystallization of nanoparticles in continuous-flow nonthermal plasma reactors," *Journal of Vacuum Science & Technology B,* vol. 32, p. 061802, 2014.

[38]   R. P. Chaukulkar, K. d. Peuter, P. Stradins, S. Pylypenko, J. P. Bell, Y. Yang*, et al.*, "Single-Step Plasma Synthesis of Carbon-Coated Silicon Nanoparticles," *ACS applied materials & interfaces,* vol. 6, pp. 19026-19034, 2014.

[39]   U. Kasavajjula, C. S. Wang, and A. J. Appleby, "Nano- and bulk-silicon-based insertion anodes for lithium-ion secondary cells," *Journal of Power Sources,* vol. 163, pp. 1003-1039, Jan 1 2007.

Chapter 6 Conclusion and Future Work

Non-thermal plasma system has many unique characteristics such as the unipolar charging of the particles, cost effectiveness, and room temperature processing which make it   more efficient and the most advantageous plasma processing method. Silicon nanoparticles, silicon-germanium alloy nanoparticles, and silicon/polymer core/shell nanoparticles are successfully synthesized using non-thermal plasma system. We confirm that silicon nanocrystals can be produced at a high production rate using silicon tetrachloride as a precursor. We present a direct comparison between the use of a chlorinated precursor and the use of silane, and discuss the consequences of precursor choice on both the process parameters and the material properties. In particular, we show that the presence of chlorine at the particle surface, and possibly also within the particle core, has important consequences on the crystallization rate, which implies that a higher power is required to produce high-quality material when silicon tetrachloride is the precursor of choice. Particles produced from silicon tetrachloride are very prone to oxidation in air, indicating that even more special care will have to be taken during the processing of this material for any of its potential applications compared to the case of the hydrogen terminated particles.

Silicon-germanium alloy nanocrystals is produced using non-thermal plasma reactor in combination with chlorinated precursors silicon tetrachloride and germanium

tetrachloride. The use of such precursors provides advantages with respect of hydrogenated precursors in terms of safety of handling and in terms of cost. As a future work, silicon-germanium alloy nanoparticles based thermoelectric devices can be fabricated.

A non-thermal plasma-based process for the synthesis of silicon nanoparticles and their in-flight coating with a plasma polymerized shell has been developed. This process takes advantage of the many unique properties of non-thermal plasmas, such as the unipolar charging of the particles and the presence of highly reactive species, to produce core/shell silicon/polyaniline-like nanoparticles. We have demonstrated that it is possible to tune the chemistry of the shell by modifying the gas-phase composition during the polymerization step. We have performed a preliminary investigation of the use of these nanoparticles in electrochemical energy storage applications. The coating of the silicon particle with a polymer shell offers a way to uniformly disperse the particles into a carbon matrix after high-temperature treatment. While further improvements are needed before being directly applicable in such applications, we report a promising improvement in the stability of an anode for lithium-ion batteries based on such material, compared to the case of uncoated silicon particles.

Further work is needed to increase the electrical conductivity of the core/shell nanoparticles by forming the conductive form of polyaniline shell on silicon core nanoparticles without annealing process which sacrifices the theoretical advantages

offered by having a potentially conductive polymer shell. Additionally further studies can be based on the finding the optimal binder that can guarantee mechanical stability of the active layer upon cycling for rechargeable batteries. This is particularly crucial for the case of silicon since its large volume change during cycling generates significant stress in the film.

.